Dissertation

submitted to the
Combined Faculties for the Natural Sciences
and for Mathematics
of the Ruperto-Carola University of Heidelberg, Germany
for the degree of
Doctor of Natural Sciences

Presented by

M. Sc. Christopher Martin Rank

Born in: Stuttgart, Germany

Oral examination: December 13, 2016

Motion-Compensated Image Reconstruction for Magnetic Resonance (MR) Imaging and for Simultaneous Positron Emission Tomography/MR Imaging

Referees: Prof. Dr. Peter Bachert

Prof. Dr. Marc Kachelrieß

"Science is a way of life. Science is a perspective. Science is the process that takes us from confusion to understanding in a manner that's precise, predictive and reliable – a transformation, for those lucky enough to experience it, that is empowering and emotional."

Brian Greene, 2008

Motion-Compensated Image Reconstruction for Magnetic Resonance (MR) Imaging and for Simultaneous Positron Emission Tomography/MR Imaging

In this work, novel algorithms for 4D (3D + respiratory) and 5D (3D + respiratory + cardiac) motion-compensated (MoCo) magnetic resonance (MR) and positron emission tomography (PET) image reconstruction were developed. The focus of all methods was set on short MR acquisition times. Therefore, respiratory and cardiac patient motion were estimated on the basis of strongly undersampled radial MR data employing joint motion estimation and MR image reconstruction. In case of simultaneous PET/MR acquisitions, motion information derived from MR was incorporated into the MoCo PET reconstruction. 4D respiratory MoCo MR image reconstructions with acquisition times of 40 s achieved an image quality comparable to standard motion handling approaches, which require one order of magnitude longer MR acquisition times. Respiratory MoCo PET images using 1 min of the MR acquisition time for motion estimation revealed improved PET image quality and quantification accuracy when compared to standard reconstruction methods. Additional compensation of cardiac motion resulted in increased image sharpness of MR and PET images in the heart region and enabled time-resolved 5D imaging allowing for reconstruction of any arbitrary combination of respiratory and cardiac motion phases. The proposed methods for MoCo image reconstruction may be integrated into clinical routine, reducing MR acquisition times for improved patient comfort and increasing the diagnostic value of MR and simultaneous PET/MR examinations of the thorax and abdomen.

Bewegungskompensierte Bildrekonstruktion für Magnetresonanz (MR)-Bildgebung und für simultane Positronen-Emissions-Tomographie/MR-Bildgebung

In der vorliegenden Arbeit wurden neuartige Algorithmen für die 4D (3D + Atmung) und 5D (3D + Atmung + Herz) bewegungskompensierte Magnetresonanz (MR)- und Positronen-Emissions-Tomographie (PET)-Bildrekonstruktion entwickelt. Schwerpunkt aller Methoden waren kurze MR-Aufnahmezeiten. Aus diesem Grund wurde die Atem- und Herzbewegung der Patienten auf Basis von stark unterabgetasteten radialen MR-Daten mit einem Verfahren geschätzt, welches die Bewegungsschätzung mit der MR-Bildrekonstruktion verknüpft. Bei simultaner PET/MR Datenaufnahme wurde die von MR-Daten abgeleitete Bewegungsinformation in die bewegungskompensierte PET-Rekonstruktion integriert. 4D atemkompensierte MR-Bildrekonstruktionen mit einer Aufnahmezeit von 40 s erzielten eine vergleichbare Bildqualität wie Standardverfahren zur Bewegungsreduktion, die jedoch eine Größenordnung längere Aufnahmezeiten benötigen. Atemkompensierte PET-Bilder, für die 1 min MR-Aufnahmezeit zur Bewegungsschätzung verwendet wurde, zeigten eine verbesserte visuelle Bildqualität und Quantifizierung im Vergleich zu Standardrekonstruktionsverfahren. Die zusätzliche Kompensation der Herzbewegung ergab eine erhöhte Bildschärfe der MR- und PET-Bilder im Bereich des Herzens und ermöglichte zeitaufgelöste 5D Bildgebung, womit beliebige Kombinationen aus Atem- und Herzphasen rekonstruiert werden konnten. Die vorgeschlagenen Methoden zur bewegungskompensierten Bildrekonstruktion können an die klinische Routine angepasst werden und damit durch kürzere MR-Aufnahmezeiten den Patientenkomfort verbessern sowie den diagnostischen Nutzen von MR- und simultanen PET/MR-Untersuchungen des Thorax und Abdomens erhöhen.

Contents

List of Acronyms

CT	computed tomography
ECG	electrocardiography
FBP	filtered backprojection
^{18}F-FDG	fluorodeoxyglucose
FOV	field of view
FFT	fast Fourier transform
FWHM	full width at half maximum
HDTV	high-dimensional total variation
jMoCo PET	motion-compensated PET based on joint MoCo-HDTV
joint MoCo-HDTV	joint motion-compensated high-dimensional total variation
LOR	line of response
MASTeR	motion-adaptive spatio-temporal regularization
MoCo	motion-compensated
MR	magnetic resonance
MRI	magnetic resonance imaging
MSE	mean squared error
MVF	motion vector field
NCC	normalized cross-correlation
NMI	normalized mutual information
OSEM	ordered subset expectation maximization
PET	positron emission tomography
RF	radio frequency
sMoCo PET	motion-compensated PET based on standard motion estimation
SNR	signal-to-noise ratio
SSIM	structural similarity
SUV	standardized uptake value
$\mathbf{SUV_{max}}$	maximum standardized uptake value
$\mathbf{SUV_{mean}}$	mean standardized uptake value
TV	total variation
VOI	volume of interest

1 | Introduction

Magnetic resonance imaging (MRI) and positron emission tomography (PET) represent two common imaging modalities employed in modern radiology and nuclear medicine to diagnose and assess a wide range of diseases covering all parts of the human body. While sequential imaging of a patient with these devices has been available for many years, a novel hybrid device combining both modalities was introduced in the year 2011 (Delso et al., 2011). This device allows for simultaneous acquisition of PET and magnetic resonance (MR) data delivering an intrinsic spatial and temporal correlation of the resulting PET and MR images. While PET offers molecular imaging with high sensitivity but limited resolution, MRI provides high-resolution morphological imaging. This complementary information is very promising for applications in the fields of oncology, neurology, cardiology and pediatric imaging (Quick, 2014) and there is ongoing research to define and establish key applications of simultaneous PET/MR imaging (Nensa et al., 2014; Bailey et al., 2015a,b). Advantages over combined PET/computed tomography (CT) are an enhanced soft tissue contrast and reduced radiation dose when using MRI instead of CT (Jadvar and Colletti, 2014). A disadvantage of MRI and PET are the relatively long acquisition times in the range of several minutes, e. g. required for examination of the complete thorax. Due to this property, a major challenge in PET and MR image reconstruction is to deal with patient motion during measurements, especially when imaging the thorax and abdomen, which are affected by respiratory and cardiac motion. As a consequence, reconstructed images reveal motion blurring if no motion handling strategy is applied (Schultz et al., 1984; Visvikis et al., 2006) as demonstrated in Fig. 1.1. Besides reducing motion blur in static MRI, dynamic time-resolved imaging is of high interest as it can provide valuable information for radiotherapy (Blackall et al., 2006; Dinkel et al., 2009; Sawant et al., 2014) or for studying physiology (von Siebenthal et al., 2007; Biederer et al., 2009, 2010; La Gerche et al., 2013). In case of PET, motion blurring further leads to a degradation of quantification accuracy. As reported by Kinahan and Fletcher (2010), respiratory motion may lead to an underestimation of standardized uptake values (SUVs) in the range of 25%. This effect may impede detection of small lesions or it may impair therapy monitoring and a precise definition of tumor volumes for applications in radiation therapy and surgery (Catana, 2015).

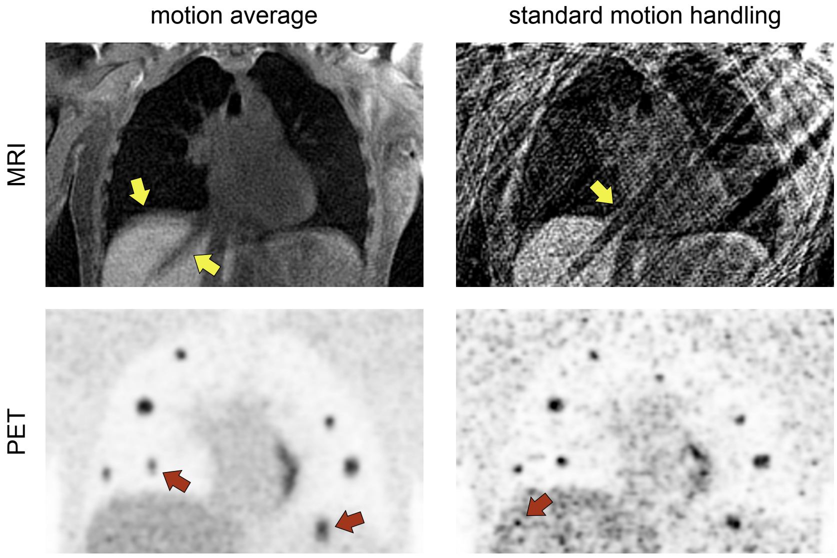

Figure 1.1: Comparison of standard MR and PET reconstruction methods for the thorax region. While motion average images reveal blurring due to respiratory and cardiac motion, standard motion handling strategies usually suffer from increased artifact levels.

For both MRI and PET, standard motion handling strategies, such as gating, are limited in many cases as they suffer from increased artifact levels (Fig. 1.1) or demand inappropriately long acquisition times. In the field of MRI, more advanced methods use compressed sensing–based reconstruction to reduce the artifact level of the images (Lustig et al., 2007, 2008; Hollingsworth, 2015). In addition, motion-compensated (MoCo) image reconstruction has been proposed (Batchelor et al., 2005; Odille et al., 2008; Wang and Amini, 2012; McClelland et al., 2013). This approach requires an estimation of patient motion, then allowing for reconstruction of each individual motion phase from 100% of the measured raw data. In addition, simultaneous PET/MR enables MoCo PET reconstruction using MR-based motion estimation (Catana, 2015; Munoz et al., 2016). However, when applying short MR acquisition times and thus high undersampling, artifacts may impair the quality of motion estimation and the subsequent MoCo image reconstruction.

This work aims at developing novel algorithms for time-resolved 4D (3D + respiratory) and 5D (3D + respiratory + cardiac) MoCo MR and PET image reconstruction. For all methods, respiratory and cardiac patient motion shall be estimated on basis of MR data acquired during free breathing. The focus of developments is set on reducing the MR acquisition time necessary for motion estimation, which may help to improve patient comfort in the scanner and to increase patient throughput in clinical practice. The resulting strong undersampling of MR data requires to design the motion estimation to be robust against artifacts arising from the undersampling. Enabling MoCo MR image reconstruction, the novel methods shall allow for a reduction of MR acquisition time by one order of magnitude in comparison to standard motion handling approaches while achieving comparable image quality. In case of simultaneous PET/MR acquisitions, motion information derived from MR shall be incorporated into a MoCo PET reconstruction. To allow for clinical MR examinations during the simultaneous PET/MR measurement, only a fraction of the MR acquisition time shall be used for motion estimation, e. g. 1 min of a 5 min scan.

The following algorithmic developments are covered by this work:

- *4D respiratory time-resolved MRI*: A novel algorithm combining a specifically-tailored iterative MR image reconstruction with artifact-robust motion estimation is developed. The method is embedded in a framework of joint motion estimation and image reconstruction. This joint approach is supposed to provide high-quality respiratory time-resolved 4D MR images and motion information of the patient when using MR data with high undersampling and thus short acquisition times.

- *4D respiratory MoCo PET*: To compensate for respiratory motion in PET, a MoCo image reconstruction framework for simultaneous PET/MR data is implemented. Motion estimation is based on MR data and resulting motion information is incorporated into the MoCo PET reconstruction algorithm. Compensating for respiratory motion, MoCo PET images are supposed to exhibit improved quantification accuracy when compared to the motion average.

- *5D respiratory and cardiac MoCo MRI*: The algorithms developed for estimation and compensation of respiratory patient motion are extended to enable additional compensation of cardiac motion. For robust estimation of both motion types from strongly undersampled MR data, respiratory and cardiac motion are estimated sequentially. Compensation of full organ motion shall allow for the reconstruction of any arbitrary combination of respiratory and cardiac motion phase with high image sharpness using 100% of the measured MR raw data.

- *5D respiratory and cardiac MoCo PET*: Likewise, the MoCo PET reconstruction framework is extended to incorporate additional MR-based cardiac motion information into the reconstruction process.

2 | Fundamentals

This chapter gives an overview of fundamentals underlying this work. In sections 2.1 and 2.2, basics of MR and PET imaging are presented. Image registration as a method for motion estimation is explained in section 2.3. Section 2.4 provides an introduction to respiratory and cardiac motion management in MRI and PET.

2.1 Magnetic Resonance Imaging

MRI is a tomographic imaging technique, which has a large spectrum of applications in modern medicine ranging from orthopedics and cardiology to neurology and oncology. This noninvasive technique generally provides anatomical or morphological images of inner body structures, which can be acquired *in vivo* with a resolution in the range of 1 mm. Advantages of MRI are an excellent soft tissue contrast and the fact that in contrast to other imaging techniques such as CT or PET, no exposure of the patient to ionizing radiation is necessary. Comprehensive descriptions of fundamentals and applications of MRI are presented in Haacke et al. (1999), Liang and Lauterbur (1999), Bernstein et al. (2004) and Reiser et al. (2008).

2.1.1 Nuclear Magnetic Resonance

Measuring MR signals is based on the effect of nuclear magnetic resonance, which was discovered by Bloch (1946) and Purcell et al. (1946). Atomic nuclei with an odd number of protons and/or neutrons possess a nonzero nuclear spin $\boldsymbol{I}$ that is related to a nuclear magnetic moment $\boldsymbol{\mu}_I$:

$$\boldsymbol{\mu}_I = \gamma \, \boldsymbol{I}, \tag{2.1}$$

with γ as the gyromagnetic ratio of nuclei. In a constant magnetic field $\boldsymbol{B}_0$, these magnetic moments align, which lifts the degeneracy of energy levels (Fig. 2.1 a). This phenomenon is known as the nuclear Zeeman effect. As $I = 1/2$ for hydrogen, only two discrete states exist (Fig. 2.1 b). The energy difference ΔE between both states is proportional to the magnetic field strength:

$$\Delta E = \gamma \, \hbar \, B_0, \tag{2.2}$$

with $\hbar$ as the reduced Planck constant. In the case of hydrogen, the probability of occupancy is slightly higher for the parallel lower-energy state in comparison to the antiparallel higher-energy state.

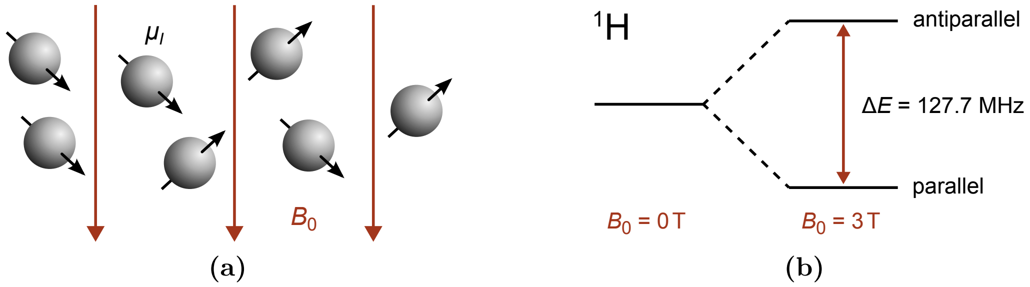

Figure 2.1: (a) Alignment of nuclear magnetic moments in the environment of a constant magnetic field $\boldsymbol{B}_0$. (b) Zeeman splitting for hydrogen that results in two discrete states lifting the degeneracy of energy levels.

The excess of parallel states can be described by Boltzmann statistics and is very small in the order of 10^{-6} at $B_0 \approx 1\,\mathrm{T}$, but generates a macroscopic magnetization $\boldsymbol{M}$ that is defined as the vector sum of expectation values of nuclear magnetic moments per unit volume V:

$$\boldsymbol{M} = \frac{1}{V} \sum_i \langle \boldsymbol{\mu}_I \rangle_i . \tag{2.3}$$

Applying a radio frequency (RF) pulse with perpendicular orientation to the direction of the magnetic field $\boldsymbol{B}_0$ and frequency $\omega_{\mathrm{rf}} = \frac{\Delta E}{\hbar}$, the macroscopic magnetization $\boldsymbol{M}$ can be tipped away from its parallel alignment to the $\boldsymbol{B}_0$-field by exciting spins into the higher-energy state. In this excited state the magnetization precesses about the direction of the magnetic field $\boldsymbol{B}_0$ with the Larmor frequency ω_0:

$$\omega_0 = \gamma \, B_0 . \tag{2.4}$$

The precession of the transversal component of the magnetization M_{xy} about the axis of the magnetic field $\boldsymbol{B}_0$ leads to an induction of a current in a receiver coil, which is proportional to the magnitude of the transversal component and can be measured as the MR signal.

Spin–spin interactions and interactions of spins with their environment cause a relaxation of the magnetization back to equilibrium. These relaxation processes can be described by the Bloch equations (Bloch, 1946):

$$\frac{\mathrm{d}M_x}{\mathrm{d}t} = (\boldsymbol{M} \times \gamma \boldsymbol{B})_x - \frac{M_x}{\mathrm{T}_2}, \tag{2.5}$$

$$\frac{\mathrm{d}M_y}{\mathrm{d}t} = (\boldsymbol{M} \times \gamma \boldsymbol{B})_y - \frac{M_y}{\mathrm{T}_2}, \tag{2.6}$$

$$\frac{\mathrm{d}M_z}{\mathrm{d}t} = (\boldsymbol{M} \times \gamma \boldsymbol{B})_z + \frac{M_0 - M_z}{\mathrm{T}_1}, \tag{2.7}$$

where M_0 represents the magnitude of the magnetization vector in equilibrium. The spin–lattice relaxation time T_1 describes the recovery of the longitudinal component of magnetization M_z, which is caused by an energy transfer from the spin system to the surrounding lattice restoring thermal equilibrium (Eq. (2.7) and Fig. 2.2 a). In addition to that process, the transversal component of magnetization M_{xy} decays with the spin–spin relaxation time T_2. Due to dipole–dipole interactions, local magnetic fields are disturbed resulting in different precession frequencies and finally in an irreversible decay of phase coherence of preceding spins (Eq. (2.5), Eq. (2.6) and Fig. 2.2 b). Local inhomogeneities of the static magnetic field $\boldsymbol{B}_0$ and a heterogeneous magnetic susceptibility of the probe cause further dephasing of spins accelerating the decay of the transversal component of magnetization M_{xy}. This faster decay is described by the characteristic time T_2^*. As the disturbing magnetic fields are constant in time, this process can however be reversed, e. g. by applying a RF pulse that flips the magnetization vector by 180°.

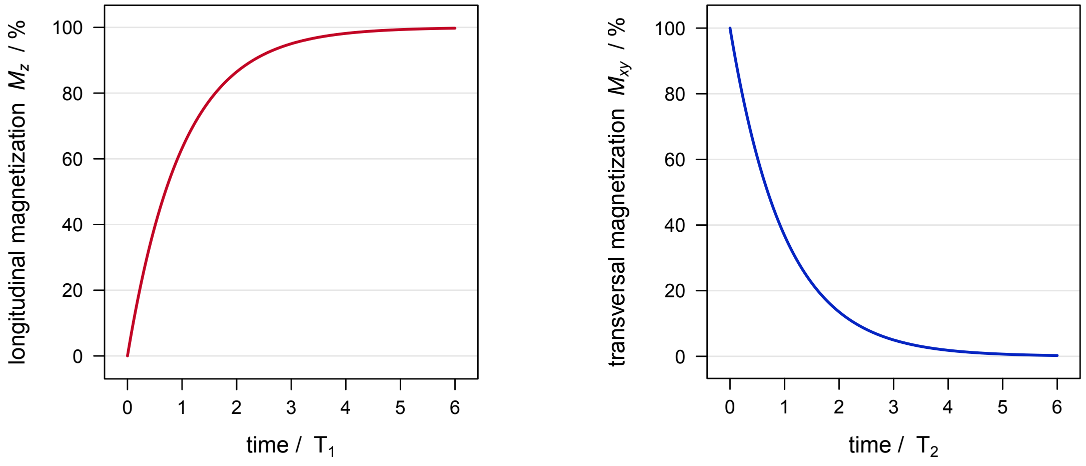

(a) longitudinal relaxation **(b)** transversal relaxation

Figure 2.2: Temporal evolution of the magnitude of (a) the longitudinal and (b) the transversal component of magnetization after excitation with a 90° RF pulse (in units of T_1 and T_2). For hydrogen and in biological tissue, T_1 is approximately in the range of 300 – 2000 ms while T_2 is about 30 – 150 ms (de Bazelaire et al., 2004; Stanisz et al., 2005). The two curves represent solutions of the Bloch equations defined in Eq. (2.7) and Eq. (2.5), (2.6), respectively.

2.1.2 Signal Localization and k-Space Formalism

In order to obtain a spatial resolution of the MR signal, the constant magnetic field $\boldsymbol{B}_0$ is superimposed with a time- and location-dependent gradient field:

$$\boldsymbol{B}_{\boldsymbol{G}}(\boldsymbol{r}, t') = (\boldsymbol{G}(t') \cdot \boldsymbol{r})\, \boldsymbol{e}_z = (G_x(t')\, x + G_y(t')\, y + G_z(t')\, z)\, \boldsymbol{e}_z, \tag{2.8}$$

with the gradient $\boldsymbol{G}(t')$ and the unit vector $\boldsymbol{e}_z$. As a result, the magnetic field and the Larmor frequency become dependent on the location $\boldsymbol{r}$:

$$\omega(\boldsymbol{r}, t') = \omega_0 + \gamma\, \boldsymbol{G}(t')\, \boldsymbol{r}. \tag{2.9}$$

Applying the additional gradient $\boldsymbol{G}(t')$ allows for either exciting only a selected slice by tuning the RF to the Larmor frequency of that particular slice or encoding the MR signal with a location-dependent phase or frequency $\phi(\boldsymbol{r}, t)$:

$$\phi(\boldsymbol{r}, t) = \int_0^t \gamma\, \boldsymbol{G}(t')\, \boldsymbol{r}\, \mathrm{d}t' = 2\pi\, \boldsymbol{k}(t)\, \boldsymbol{r}, \tag{2.10}$$

with:

$$\boldsymbol{k}(t) = \frac{\gamma}{2\pi} \int_0^t \boldsymbol{G}(t')\, \mathrm{d}t'. \tag{2.11}$$

The variable $\boldsymbol{k}(t)$ corresponds to a spatial frequency and can be interpreted as a position in the so-called k-space. Varying the strength and direction of the gradient $\boldsymbol{G}(t')$, arbitrary locations in k-space can be probed. Whereas low frequencies at the k-space center are correlated with image contrast, high frequencies at outer areas yield image details and fine structure. There exist different schemes for probing the k-space, e. g. Cartesian or radial sampling (Fig. 2.3). In the Cartesian case, a rectilinear grid is sampled along lines defining a particular readout direction. In contrast, for radial sampling each measured k-space line has a different readout direction.

The measured MR signal for each point in k-space is composed of the integrated transversal magnetization of the whole imaging volume. In a rotating frame about the z-direction with frequency ω_0, the measured MR signal $p(\boldsymbol{k})$ is then given as follows:

$$p(\boldsymbol{k}) = \int M_{xy}(\boldsymbol{r})\, \mathrm{e}^{-2\pi\, \mathrm{i}\, \boldsymbol{k}\, \boldsymbol{r}} \mathrm{d}\boldsymbol{r}. \tag{2.12}$$

This equation demonstrates that the MR signal $p(\boldsymbol{k})$ corresponds to the Fourier transform of the spatial distribution of the transversal magnetization $M_{xy}(\boldsymbol{r})$. Accordingly, the image represented by the location-dependent transversal magnetization $M_{xy}(\boldsymbol{r})$ can be obtained by the inverse Fourier transform of the measured signal $p(\boldsymbol{k})$.

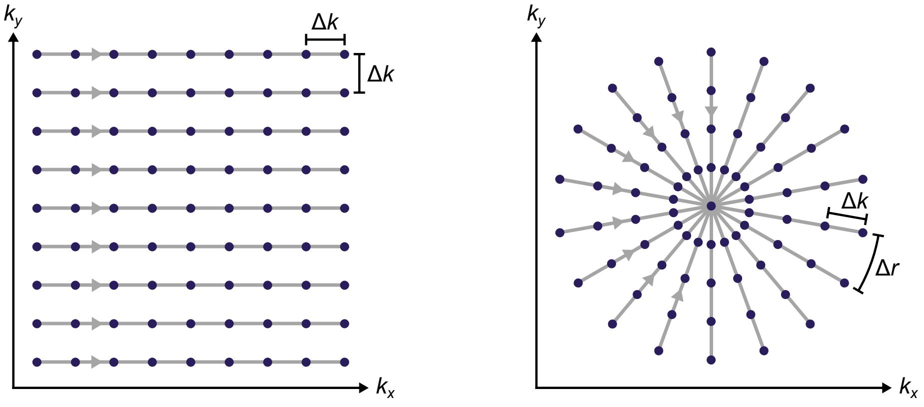

(a) Cartesian sampling **(b)** radial sampling

Figure 2.3: Different schemes for probing the k-space: gray lines represent trajectories through k-space. The MR signal is then measured at discrete points along these trajectories indicated in dark blue.

2.1.3 Sampling Requirements

During MR data acquisition, the continuous Fourier transform of the object is sampled on a discrete grid with sampling distance Δk. While application of the sampling function in k-space corresponds to a multiplication of the continuous signal with a comb function, the object is convolved with a comb function with reciprocal period $\frac{1}{\Delta k}$ in image space. This convolution results in a periodic repetition of the object at a distance $\frac{1}{\Delta k}$. This distance is commonly referred to as the field of view (FOV). To avoid aliasing, i. e. an overlap of neighboring repetitions of the object as shown in Fig. 2.4, the sampling distance Δk has to be chosen in such a way, that the FOV fully covers an object of size L to be imaged. This requirement is known as the Nyquist sampling criterion (Nyquist, 1928):

$$L \leq \text{FOV} \quad \text{or} \quad \Delta k \leq \frac{1}{L}. \tag{2.13}$$

If $\Delta k < \frac{1}{L}$ is chosen, a so-called readout oversampling is applied during the measurement. In case of radial sampling, distances between measurement points along spokes and between points of neighboring spokes (represented by Δr in Fig. 2.3 b), have to satisfy the Nyquist criterion. Thus the number of spokes N_{spokes} can be chosen as follows:

$$N_{\text{spokes}} = \frac{\pi}{2} N, \tag{2.14}$$

with N being the number of voxels along one spatial dimension in the reconstructed image. Compared to Cartesian sampling, the number of required k-space lines is increased by about 57%. However, while aliasing in Cartesian sampling manifests in repetitions of the object, radial undersampling is more benign resulting in streak artifacts in the reconstructed images (Fig. 2.4).

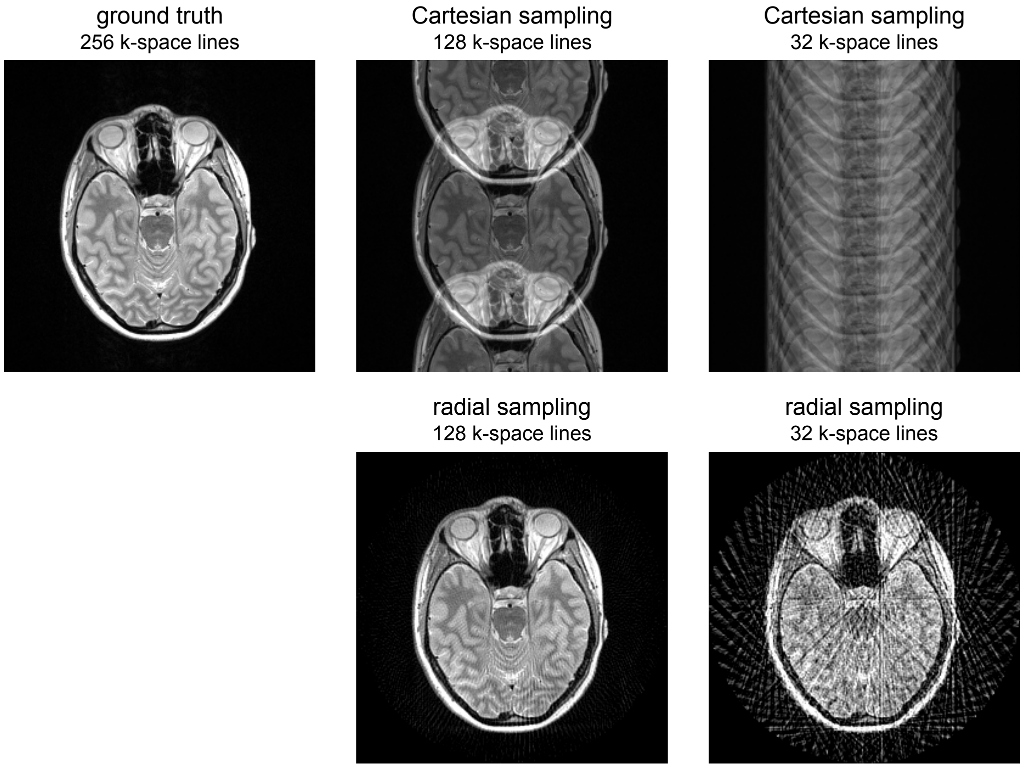

ground truth
256 k-space lines

Cartesian sampling
128 k-space lines

Cartesian sampling
32 k-space lines

radial sampling
128 k-space lines

radial sampling
32 k-space lines

Figure 2.4: Comparison of undersampling artifacts of Cartesian and radial sampling. In the Cartesian case, twofold (center) and eightfold undersampling (right) in the row direction are shown. In the radial case, the same number of k-space lines as used for Cartesian sampling was employed to simulate comparable acquisition times. This corresponds to radial undersampling factors of 3.14 (center) and 12.57 (right), respectively.

2.1.4 Advantages and Disadvantages of Radial Sampling

One advantage of a radial acquisition scheme is its lower sensitivity to object motion. As the center of k-space is sampled during each readout, ghosting is strongly reduced compared to Cartesian patterns (Glover and Pauly, 1992; Block et al., 2014). As the radial plane is sampled at different angles, readout oversampling can be employed in two dimensions, which eliminates aliasing artifacts for large objects. In addition, radial acquisition reveals a more benign undersampling behavior than Cartesian sampling. As shown in Fig. 2.4, radial undersampling preserves a large amount of object information and spatial resolution in contrast to Cartesian sampling, which yields either blurring or aliasing when reducing the number of k-space lines. A further property of the radial geometry is that each spoke covers the same amount of low and high frequencies. Thus the measured data can be subdivided into arbitrary subsets of spokes without introducing ghosting or intensity variations, which is attractive for dynamic applications (Rasche et al., 1995; Larson et al., 2004; Winkelmann et al., 2007; Uecker et al., 2010; Zhang et al., 2010a; Feng et al., 2014).

One disadvantage of radial sampling is the larger number of k-space lines required to satisfy the Nyquist sampling criterion as discussed in section 2.1.3. This increase of about 57% directly translates to longer acquisition times compared to Cartesian sampling. In addition, radial schemes show increased sensitivity to off-resonance, which appears when the exciting RF pulse does not exactly match the Larmor frequency of the spins, e. g. due to small local variations of the magnetic field $\boldsymbol{B}_0$. As each spoke is sampled at a different angle, phase-modulations caused by off-resonance slightly shift each spoke in a different direction resulting in blurring of the reconstructed image. Furthermore, radial data require a more complex image reconstruction in comparison to Cartesian data as shown in section 2.1.6.

2.1.5 MRI Contrasts

The process of measuring an MR image is described by the MR sequence that controls the RF excitation pulse, the gradients for spatial encoding and the signal acquisition. In MRI, the intensity of a voxel depends on several parameters, mainly on its density of water and fat protons and on its tissue-specific relaxation parameters T_1, T_2 and T_2^*. While many other techniques exist (Bernstein et al., 2004), adjusting the echo time TE and repetition time TR in the sequence protocol typically determines which of the above-mentioned parameters has the strongest influence on the signal intensity of the voxel and thus the image contrast. Examples of different contrast weightings are shown in Fig. 2.5. A very short echo time ($TE \ll \mathrm{T}_2^*$) and a long repetition time ($TR \gg \mathrm{T}_1$) yields a proton density–weighted contrast. A T_2- or T_2^*-weighting is achieved by an appropriate echo time and a long repetition time ($TR \gg \mathrm{T}_1$). A very short echo time ($TE \ll \mathrm{T}_2^*$) and an appropriate repetition time result in a T_1-weighted image.

2.1.6 Analytic Image Reconstruction

The aim of MR image reconstruction is to resolve the spatial distribution of the transversal magnetization $M_{xy}(\boldsymbol{r})$, which mainly depends on proton density and tissue relaxation characteristics. In case of Cartesian sampling, analytic image reconstruction corresponds to a discrete inverse Fourier transform along the lines of encoding. In accordance to Eq. (2.12), replacing $M_{xy}(\boldsymbol{r})$ by the reconstructed image $f(x)$ yields the following equation for the one-dimensional case:

$$f(x) = \sum_n p_n \, \mathrm{e}^{2\pi \, \mathrm{i} \, x \, k_n}. \tag{2.15}$$

As the measured raw data $\boldsymbol{p}$ are equally distributed on a regular grid, the fast Fourier transform (FFT) algorithm can be employed to reduce computational complexity from N^2 to $N \log N$. Due to its geometry, direct application of the FFT to radial data is not possible. Two reconstruction techniques for radial data are available: The filtered backprojection (FBP) (Kak and Slaney, 1988) and regridding or gridding (O'Sullivan, 1985;

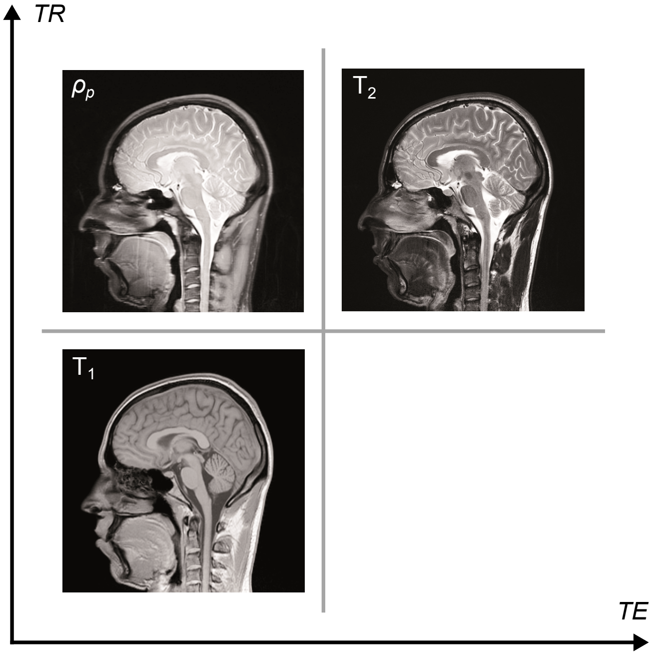

Figure 2.5: Dependence of the MRI contrast on the sequence parameters echo time *TE* and repetition time *TR*. The parameter ρ_p represents the proton density.

Jackson et al., 1991). Both approaches are closely related and linked by the projection-slice theorem, or central slice theorem. For FBP reconstruction, a one-dimensional Fourier transform along the spoke dimension is performed and the resulting projections are filtered and backprojected. Interpolation from radial geometry onto the regular grid of the image is calculated in image space. In contrast, the gridding approach interpolates radial data points in k-space onto the Cartesian grid. This allows for application of a two-dimensional FFT for conversion to image space. To account for the property that low frequencies at the k-space center are sampled more densely than high frequencies, a density compensation of sampling points has to be performed, which equals the filtering for the FBP. As small-scale variations in the frequency domain lead to large-scale changes in the image domain, interpolation in k-space has to be constructed in such a way, that effects in image space can be removed. Hence, gridding can be interpreted as a source-driven interpolation. As illustrated in Fig. 2.6, each measured data point is convolved with an interpolation kernel W and its contribution is added to neighboring grid points k. The inverse Fourier transform for image reconstruction can then be formulated as follows:

$$f(x)\,w(x) = \int \mathrm{d}k\,(p * W)(k)\,\mathrm{e}^{2\pi\,\mathrm{i}\,x\,k}. \tag{2.16}$$

Dividing by the inverse Fourier transform of the gridding kernel $w(x)$, any modulation of the image $f(x)$ can be removed, which is called roll-off correction. However, discrete sampling in k-space during interpolation, which corresponds to a multiplication with a comb function, introduces periodic repetitions of the object in image space. Thus an interpolation

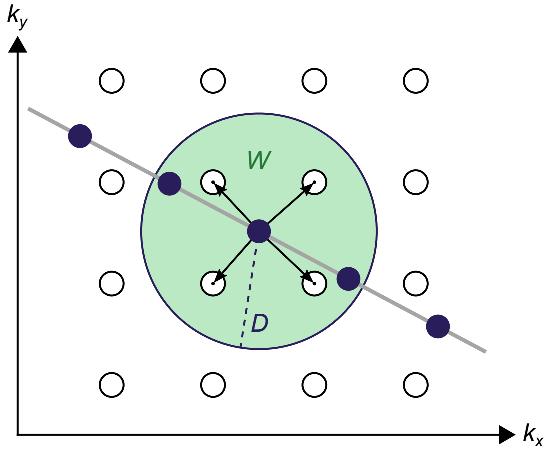

Figure 2.6: Schematic illustration of source-driven gridding interpolation in k-space. The measured data points of radial spokes (dark blue points) are typically not distributed on a regular Cartesian grid (white points). To make use of a two-dimensional FFT for reconstruction, each measured data point is convolved with an interpolation kernel and its contribution is added to neighboring grid points that are located within a specified kernel width D.

kernel with small-valued side-lobes in image domain has to be chosen. In addition, finite support in the frequency domain is required to achieve reasonable computation times. To further reduce aliasing effects, an oversampling in readout direction can be applied in practice. This approach increases the distance between repetitions of the object. An appropriate function for interpolation is the Kaiser-Bessel window (Kaiser, 1974):

$$W_{\mathrm{KB}}(d) = \begin{cases} \frac{1}{D}\, I_0(\delta\sqrt{1-(2d/D)^2}) & \text{for } |d| \leq \frac{D}{2} \\ 0 & \text{for } |d| > \frac{D}{2} \end{cases}. \tag{2.17}$$

The parameter D denotes the desired kernel width and $I_0(\cdot)$ represents the zero-order modified Bessel function of first kind. Depending on the chosen oversampling in readout direction, the artifact energy in the reconstructed image can be minimized by tuning the shape parameter δ (Beatty et al., 2005). The inverse Fourier transform of W for roll-off correction is given by:

$$w_{\mathrm{KB}}(x) = \mathsf{F}^{-1}\{W_{\mathrm{KB}}\}(x) = \operatorname{sinc}\left(\sqrt{(\pi D x)^2 - \delta^2}\right). \tag{2.18}$$

2.1.7 Iterative Image Reconstruction

Analytic image reconstruction of undersampled radial data leads to streak artifacts in the image as illustrated in Fig. 2.4 and is thus limited at high undersampling factors. The streak artifacts arise from missing data in k-space in regions between the measured spokes. Therefore, more sophisticated reconstruction techniques are required to reduce streak artifacts on the one hand and to recover object information on the other hand.

Inverse Problem and Incorporation of Prior Knowledge

Based on a vector of measured raw data $\boldsymbol{p}$, image reconstruction seeks to find the corresponding image vector $\boldsymbol{f}$. For undersampled data, the size of $\boldsymbol{p}$ is usually smaller than the size of $\boldsymbol{f}$, i. e. the problem is underdetermined. However, the measurement process can be described as a forward problem:

$$\boldsymbol{p} = \mathsf{X}\boldsymbol{f}. \tag{2.19}$$

For a given image $\boldsymbol{f}$, the measured raw data can be obtained by linear operation applying the system matrix X. This matrix represents a mathematical description of the image acquisition process. In MRI, it includes a Fourier transform and in case of radial data an interpolation onto radial spoke positions. Image reconstruction then corresponds to solving the inverse problem to Eq. (2.19) by finding the image $\boldsymbol{f}^*$ that optimizes raw data fidelity and minimizes the following cost function:

$$C(\boldsymbol{f}) = \frac{1}{2}\,\|\mathsf{X}\boldsymbol{f} - \boldsymbol{p}\|_2^2. \tag{2.20}$$

This equation can be solved by conjugate gradient methods (Hestenes and Stiefel, 1952; Boyd and Vandenberghe, 2004). For iterative optimization, the following steps are repeated in an alternating manner: In a first step, the search direction is estimated by calculating the gradient of the cost function. In the second step, a line search into that direction is carried out until the minimum of the cost function along this direction is reached. The gradient of the cost function of Eq. (2.20) can be calculated as follows:

$$\boldsymbol{\nabla} C(\boldsymbol{f}) = \mathsf{X}^{\mathrm{T}}\mathsf{X}\boldsymbol{f} - \mathsf{X}^{\mathrm{T}}\boldsymbol{p} = \mathsf{X}^{\mathrm{T}}(\mathsf{X}\boldsymbol{f} - \boldsymbol{p}), \tag{2.21}$$

with X^{T} representing the complex conjugated transposed matrix of X. While for radial data, the operator X applies a forward Fourier transform and an interpolation to radial spokes, X^{T} describes gridding to a Cartesian grid without density compensation followed by an inverse Fourier transform. The iterative process of image reconstruction is then explained by the right part of Eq. (2.21). During each iteration, the current image estimate $\boldsymbol{f}$ is forward transformed to k-space and compared to the measured raw data. To update the image estimate, the residuum is then backward transformed to image space and added to the estimate of the previous iteration.

Optimizing the cost function in Eq. 2.20 evaluates data only at the measured spoke positions. While the reconstructed image might have a perfect match with the measured raw data, missing information in k-space is not recovered and the reconstructed image still reveals streak artifacts. However, Eq. 2.20 can be extended incorporating prior knowledge about the image estimate into the reconstruction process:

$$C(\boldsymbol{f}) = \underbrace{\frac{1}{2}\|\mathsf{X}\boldsymbol{f} - \boldsymbol{p}\|_2^2}_{\text{raw data fidelity}} + \underbrace{\sum_i \eta_i \, R_i(\boldsymbol{f})}_{\text{regularization}} . \tag{2.22}$$

In addition to the raw data fidelity term, penalties $R_i(\boldsymbol{f})$ on certain properties of the reconstructed object $\boldsymbol{f}$ are added, which is called regularization. To allow for optimization of the cost function, these regularization terms have to be defined by convex functions. Using the parameters η_i, each regularization term can be weighted relative to the raw data fidelity term. Hence, the optimization is driven towards solutions that agree with the measured raw data and with prior knowledge about the reconstructed object. Thus it becomes possible to recover missing information in k-space and to remove streak artifacts from the reconstructed images. A schematic illustration of the complete iterative reconstruction process is shown in Fig. 2.7.

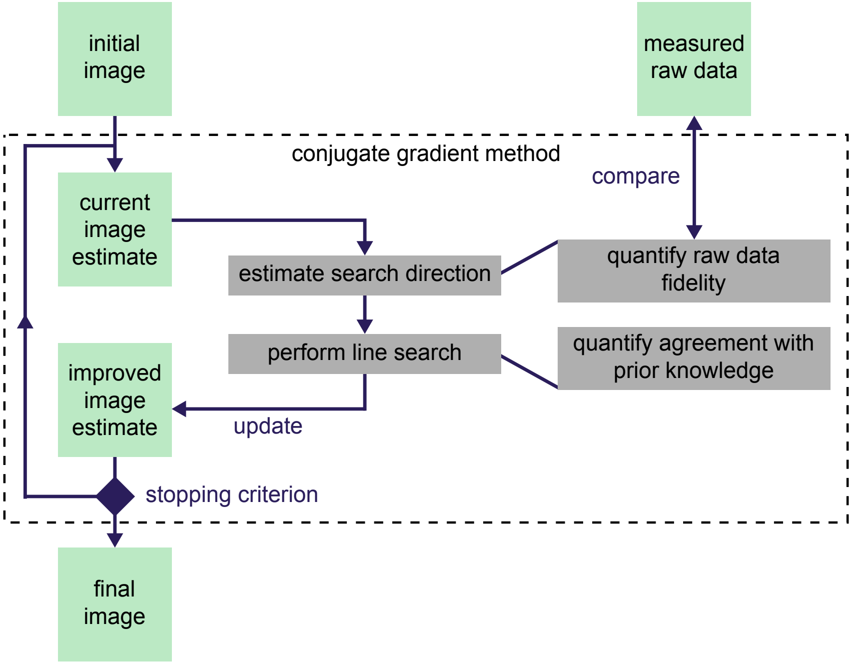

Figure 2.7: Schematic illustration of iterative MR image reconstruction. A standard conjugate gradient method can be used to find an image estimate that agrees with the measured raw data and with prior knowledge about the reconstructed object. Adopted from Block (2008).

One example of prior knowledge that can be incorporated into reconstruction is that intensity outside an object has to be zero. In addition, assuming that the measured physical quantity in MRI is a positive value, negative values in the image can be penalized. A further type of regularization, which is well-known for image denoising, is minimization of the total variation (TV) of the image (Rudin et al., 1992). Application of TV assumes piecewise constant intensities in the image, which matches the properties of a wide range of medical images quite well. The TV of an image $\boldsymbol{f}$ is defined as the sum of its first order derivatives. In two dimensions, it can be calculated as follows:

$$R_{\mathrm{TV}}(\boldsymbol{f}) = \sum_i \sqrt{(\boldsymbol{\nabla}_x f_i)^2 + (\boldsymbol{\nabla}_y f_i)^2}. \tag{2.23}$$

The operators $\boldsymbol{\nabla}_x$ and $\boldsymbol{\nabla}_y$ denote the finite differences along the respective spatial directions x and y, respectively. For dynamic image series, the TV can also be calculated for the temporal dimension. The representation of an image in the TV domain reveals entries only at edges of the original image while homogeneous regions are zero-filled. As a result, the TV image typically contains less nonzero entries than the original image. The TV operator thus serves as a sparsity transform of the image, which is in compliance with the theory of compressed sensing.

Relation to the Theory of Compressed Sensing

In clinical routine and especially in MRI, it is highly desirable to keep acquisition times as low as possible. Employing parallel imaging, complementary information of different coil channels allows for suppression of aliasing artifacts (Larkman and Nunes, 2007; Deshmane et al., 2012). In addition, partial Fourier methods exploit the symmetry of k-space (McGibney et al., 1993). For radial data acquisitions, filtering high frequencies reduces streak artifacts, but also decreases image resolution. A further opportunity for the reduction of acquisition times is provided by the theory of compressed sensing. This mathematical theory was developed for the recovery of signals from highly incomplete data (Candès et al., 2006; Donoho, 2006) and represents the theoretical foundation of regularized iterative image reconstruction. The first application to MRI was reported in Block et al. (2007), Lustig et al. (2007) and Lustig et al. (2008). Three conditions have to be fulfilled for the successful implementation of compressed sensing:

1. The true image has to be compressible, i. e. a sparse representation of the image in a known transform domain $\Psi(\boldsymbol{f})$ is required.
2. Artifacts arising from undersampling of k-space should be incoherent in this transform domain, i. e. they should have a noise-like appearance.
3. For image reconstruction, nonlinear methods should be applied, which enforce both raw data fidelity and sparsity of the image in the transform domain.

For highly undersampled raw data, Eq. (2.19) is underdetermined, i. e. there exists a whole set of images $\boldsymbol{f}^*$, which are in compliance with the measured raw data $\boldsymbol{p}$. To find an appropriate solution from this set of images, the image with the highest sparsity in the transform domain $\Psi(\boldsymbol{f})$ can be selected, which is in correspondence to the image property demanded by condition 1. Typical sparsity transforms may be the TV or wavelet transform (Lustig et al., 2007, 2008), for instance. To prevent the selection of unreasonable solutions, condition 2 assures that undersampling artifacts do not have a sparse representation in the transform domain unlike the true signal. Image reconstruction can then be formulated as a constrained optimization problem with convex behavior:

$$\boldsymbol{f}^* = \underset{\boldsymbol{f}}{\operatorname{argmin}} \|\Psi(\boldsymbol{f})\|_1 \quad \text{subject to} \quad \|\mathsf{X}\boldsymbol{f} - \boldsymbol{p}\|_2^2 < \epsilon. \tag{2.24}$$

The parameter $\epsilon > 0$ is chosen to relax the raw data fidelity constraint accounting for noise and the incomplete description of the measurement process by the system matrix X. For optimization of Eq. (2.24), an unconstrained formulation can be used (Song et al., 2007). This allows for optimizing both parts of the equation in an alternating manner employing a standard conjugate gradient algorithm (Boyd and Vandenberghe, 2004).

2.2 Positron Emission Tomography

PET is an imaging modality in the field of nuclear medicine, which allows for noninvasive measurement of the spatial distribution of a radioactive substance *in vivo*. This substance called tracer is injected into the patient prior to the examination. It is composed of a biomolecule labeled with a radioisotope. The tracer is intended to participate in physiological or functional processes mimicking the specific behavior of the original biomolecule. Thus it becomes possible to gain information about biochemical reactions at a molecular level or about physiology, such as metabolism and blood flow. In clinical practice, this physiological or functional information is a valuable complement to the anatomical or morphological information primarily provided by MRI or CT. The glucose analog fluorodeoxyglucose (^{18}F-FDG) labeled with the radioisotope ^{18}F is the most commonly applied tracer in PET imaging providing information about the local glucose metabolism. A detailed overview of PET is given in Bailey et al. (2005), Saha (2010) and Kim et al. (2013).

2.2.1 Positron Decay and Positron–Electron Annihilation

PET imaging is based on the emission of radiation from unstable isotopes, which decay by emission of a positron. This β^+-decay occurs for proton-rich radionuclides when a proton is converted to a neutron emitting a positron and an electron neutrino. For a nucleus X with mass number A and Z protons, the β^+-decay to a daughter nucleus Y can be formulated as follows:

$${}^{A}_{Z}X \longrightarrow {}^{A}_{Z-1}Y + e^+ + \nu_e + Q. \tag{2.25}$$

The decay products e^+ and ν_e denote the positron and the electron neutrino, respectively, while Q represents the released energy. This energy is distributed continuously between positron and neutrino as kinetic energy and depends on the decaying isotope. Traversing matter, the positron interacts with atomic electrons and loses its kinetic energy. Almost at rest, it combines with an electron representing its antiparticle. This process is called positron–electron annihilation:

$$e^+ + e^- \longrightarrow \gamma + \gamma. \tag{2.26}$$

According to the law of conservation of momentum, the annihilation most likely produces two photons γ, which carry the same amount of energy and are emitted in opposite direction under an angle of about 180°. Due to conservation of energy, the photon energy equals 511 keV each, which in total is equivalent to the rest mass of the positron–electron pair. The physical processes important for PET imaging are illustrated in Fig. 2.8.

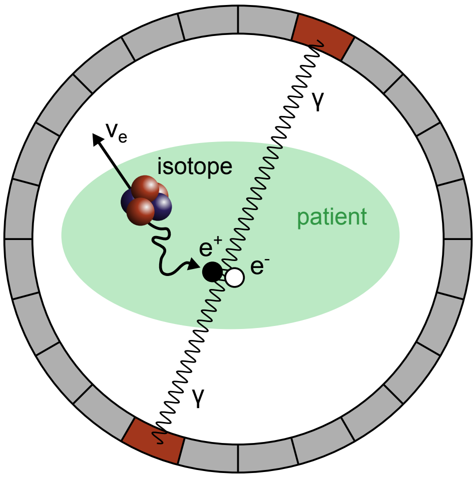

Figure 2.8: Principle of PET: A radioactive isotope is injected to the patient (green) and disperses in the body. The substance decays via β^+-decay generating a positron and an electron neutrino. When the positron is almost at rest, it annihilates with an electron emitting two photons in opposite directions. These photons can be detected and assigned to the annihilation event by the coincidence measurement (red).

As the positron originating from the β^+-decay carries kinetic energy, it travels a certain range through matter before annihilation. This range depends on the kinetic energy and thus the emitting isotope on the one hand and on the electron density of the traversed material on the other hand. Mean ranges in water of typical isotopes used in PET are approximately 1 to 3 mm. This effect causes a disagreement between isotope distribution and the distribution of annihilation events. Besides, positrons may still carry a small momentum at annihilation. To conserve momentum, the created photons are thus emitted at angles slightly varying around the 180° with a standard deviation of 0.25° (DeBenedetti et al., 1950), which is called non-collinearity. Both effects, the positron range and the non-collinearity, induce a physical limit of the intrinsic spatial resolution obtained by PET. However, for common tracers, these errors are typically below the resolution of PET detectors used in clinical practice.

Radioactive decay is a statistical process, i. e. prediction of individual events is limited to probability. Common probability distributions to model decay processes are the binomial distribution and for a large concentration of isotope the Poisson distribution. The activity A is proportional to the number of isotopes in the sample and defines the number of disintegrations per time interval. The unit is $1\,\mathrm{s}^{-1} = 1\,\mathrm{Bq}$ (Becquerel). For a given activity A_0 at time $t = 0$, the activity at time t can be expressed as:

$$A(t) = A_0\, \mathrm{e}^{-\lambda\, t}. \tag{2.27}$$

The decay constant λ is directly related to the half-life of an isotope, which specifies the time interval reducing the initial activity to one-half:

$$T_{1/2} = \frac{\ln 2}{\lambda}. \tag{2.28}$$

2.2.2 Photon Interaction with Matter

Photons originating from positron–electron annihilation are monoenergetic with an energy of 511 keV. At this energy, interactions when traversing matter can be described by contributions of two major interaction processes, namely (i) the photoelectric effect and (ii) inelastic Compton scattering. When the incident photon interacts with an atom by the photoelectric effect, it is absorbed and transfers its entire energy to an inner shell electron, which is then ejected. In case of inelastic Compton scattering, the photon interacts with a weakly bound outer shell electron and transfers only part of its energy to the electron. While the electron is ejected, a photon of lower energy is emitted escaping at a different angle than the original photon as the momentum of the system has to be conserved. Other interaction processes, such as Rayleigh scattering and the nuclear photoelectric effect, can be neglected at 511 keV. Furthermore, pair production is not possible due to the insufficient photon energy. The interaction processes result in an attenuation of photons and, at a fixed energy, they are solely influenced by the material composition of the traversed object. The attenuation is characterized by the linear attenuation coefficient:

$$\mu = \rho_e\, \sigma, \tag{2.29}$$

with the electron density ρ_e and the total cross-section of interaction processes σ. A plot of linear attenuation coefficients of water for different energies is shown in Fig. 2.9. It demonstrates that attenuation of 511 keV photons is dominated by Compton scattering.

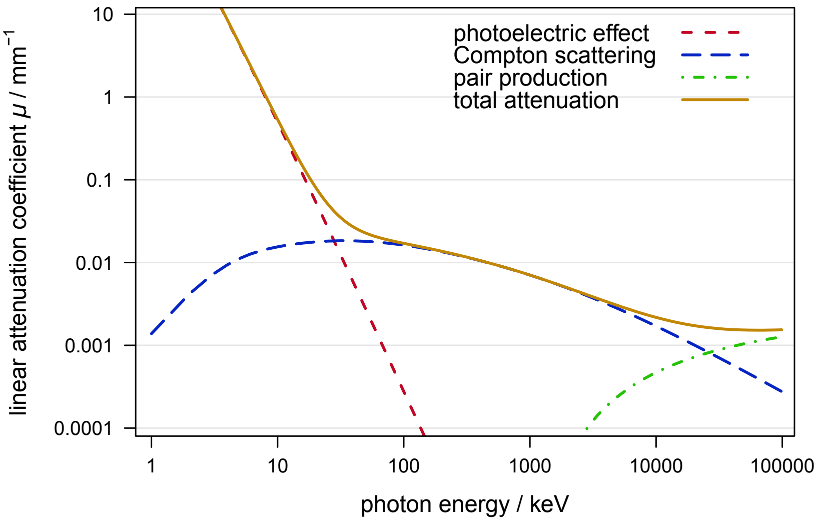

Figure 2.9: Linear attenuation coefficient of water for different photon energies.

The reduction of photon intensity after traversing an object of length L can be described by the Beer-Lambert law that has the following form for an inhomogeneous object:

$$I(L) = I_0 \, \mathrm{e}^{-\int_0^L \mu(l)\,\mathrm{d}l}, \tag{2.30}$$

with I_0 as the initial photon intensity.

2.2.3 Detection of Annihilation Photons

In PET, the distribution of positron annihilations is measured as it is closely related to the desired tracer distribution within the imaged object. If not attenuated within the object, two photons originating from an annihilation event can be detected nearly simultaneously. This property forms the basis of PET and the measurement is called coincidence detection. Photons detected within a certain timing window are assigned to the same annihilation event. This allows for distinguishing annihilation events occurring at slightly different times. Furthermore, it yields the information that the annihilation event took place along a line connecting both detectors. This line is called line of response (LOR). For measuring annihilation photons, modern PET scanners typically use a detector ring. The detectors employ scintillators to convert the incident 511 keV photons into visible light. Besides a high stopping power for the incident photons, scintillators are required to provide a high energy resolution and a short signal decay time. The visible light is then transformed into an electronic signal by a photodetector. The most common device for conversion is the photomultiplier tube (Kim et al., 2013). Here, the scintillator photons create electrons that are amplified towards an electrode with positive charge. In strong magnetic fields, e. g. in simultaneous PET/MR, robust operation of photomultiplier tubes is not possible.

Hence, semiconductor-based photodiodes, such as avalanche photodiodes (Pichler et al., 2006; Catana et al., 2006) or silicon photomultipliers (Roncali and Cherry, 2011), can be employed. Here, incident scintillator photons create electron–hole pairs in the diodes that can be amplified to generate an electronic signal.

2.2.4 Image Reconstruction

The aim of PET image reconstruction is the calculation of the activity distribution within the measured object. The measured counts per LOR represent estimates of the line integrals through this distribution. Thus for analytic reconstruction, a FBP (Kak and Slaney, 1988) can be employed. Due to the statistical nature of PET, measured data typically contain considerable noise levels in practice. Therefore, algebraic reconstruction techniques, which model these statistical fluctuations, usually provide better image quality than FBP. They seek to find an activity distribution that reproduces the measured data with highest probability. Similar to the iterative MR image reconstruction, this inverse problem is solved by optimizing some kind of cost function. For a given initial activity distribution $\boldsymbol{\lambda}_0$, a forward transform to raw data space and comparison to the measured raw data $\boldsymbol{p}$ is performed. As a result, an update of the activity distribution can be calculated. These steps are repeated until improvement of the cost function reaches a specific stopping criterion. For a discrete representation of the desired activity distribution $\boldsymbol{\lambda} = (\lambda_1, \ldots, \lambda_I)$, the expected raw data $\hat{\boldsymbol{p}} = (\hat{p}_1, \ldots, \hat{p}_J)$ are given in the forward model as follows:

$$\hat{\boldsymbol{p}} = M\boldsymbol{\lambda}. \tag{2.31}$$

The system matrix M models the measurement process and gives the probability that an annihilation event in voxel i is detected at LOR j of the expected raw data $\hat{\boldsymbol{p}}$. Assuming a Poisson distribution as statistical model, the probability $P(p_j)$ of observing p_j when $\hat{p}_j$ represents the expectation value is defined by:

$$P(p_j) = \frac{\mathrm{e}^{-\hat{p}_j}\,\hat{p}_j^{p_j}}{p_j!}. \tag{2.32}$$

Combining all measured LORs, which possess independent probabilities $P(p_j)$, yields the likelihood function $P(\boldsymbol{p}|\boldsymbol{\lambda})$:

$$P(\boldsymbol{p}|\boldsymbol{\lambda}) = \prod_j P(p_j) = \prod_j \frac{\mathrm{e}^{-\hat{p}_j}\,\hat{p}_j^{p_j}}{p_j!}. \tag{2.33}$$

Instead of the function in Eq. (2.33), its logarithm $l(\boldsymbol{p}|\boldsymbol{\lambda})$ is often used for image reconstruction:

$$l(\boldsymbol{p}|\boldsymbol{\lambda}) = \ln P(\boldsymbol{p}|\boldsymbol{\lambda}) = \sum_j (p_j \ln \hat{p}_j - \hat{p}_j - \ln(p_j!)). \tag{2.34}$$

The desired solution is then represented by the activity distribution $\boldsymbol{\lambda}^*$, which maximizes the likelihood function $l(\boldsymbol{p}|\boldsymbol{\lambda})$ (Rockmore and Macovski, 1976). This solution can be found by iterative approaches, e. g. using the expectation maximization algorithm (Dempster et al., 1977; Shepp and Vardi, 1982; Lange and Carson, 1984), which yields in its most basic form the following update equation:

$$\boldsymbol{\lambda}^{(n+1)} = \boldsymbol{\lambda}^{(n)} \frac{1}{M^{\mathrm{T}}1} M^{\mathrm{T}} \frac{\boldsymbol{p}}{M\boldsymbol{\lambda}^{(n)}}. \tag{2.35}$$

The matrix M^{T} denotes the transpose of the system matrix M and n represents the iteration index. To account for nonlinear physical effects biasing the measurement, such as scatter and randoms as described in section 2.2.5, data correction terms can be added to the denominator of the last term of Eq. (2.35). Furthermore, to decrease computational effort, the ordered subset expectation maximization (OSEM) algorithm was introduced (Hudson and Larkin, 1994). This modification of the expectation maximization algorithm employs only a subset of the measured LORs for each image update reducing the total number of required forward and backprojections. The modified update equation with additional data correction terms is explained in section 3.2.1.

2.2.5 Data Corrections

Attenuation

Starting at the annihilation location, the emitted photons traverse the body of the patient before reaching the detector ring. Due to interaction processes, the number of photons is decreased by up to two orders of magnitude. Thus correction of this attenuation is required for reconstruction of quantitatively correct activity distributions. Employing Eq. (2.30), the probability P of detecting two photons emitted at location r at a given LOR is the product of the individual probabilities P_1 and P_2:

$$P = P_1\, P_2 = \mathrm{e}^{-\int_0^r \mu(l)\,\mathrm{d}l}\, \mathrm{e}^{-\int_r^L \mu(l)\,\mathrm{d}l} = \mathrm{e}^{-\int_0^L \mu(l)\,\mathrm{d}l}. \tag{2.36}$$

This demonstrates that for coincidence detection, attenuation along a LOR is independent of the annihilation location. Hence, attenuation correction factors can be determined from an external radioactive source, which is rotated around the patient. For hybrid devices, attenuation correction factors are usually obtained by forward projection of a so-called attenuation map, which describes the distribution of linear attenuation coefficients in the FOV. In PET/CT, this attenuation map can be calculated directly by conversion of the measured CT values into attenuation coefficients. In PET/MR, the derivation of the attenuation map is more difficult as there is no direct correlation between the MR signal and photon attenuation coefficients. Several approaches exist, which are based on

PET emission data, segmentation-based and atlas-based methods as discussed in detail by Bezrukov et al. (2013), Keereman et al. (2013) and Mehranian et al. (2016).

Normalization

To account for differences in the characteristics of individual detectors, such as geometrical efficiency or detector sensitivity, the measured raw data have to be corrected by LOR–specific normalization coefficients. These coefficients can be derived from a calibration measurement with a homogeneous activity distribution.

Scatter and Randoms

Besides the detection of desired true coincidence events, measured PET data may contain several other events as illustrated in Fig. 2.10, which impair reconstruction of the true activity distribution. If one of the photons is deflected by Compton scattering before detection, the assigned LOR will not pass through the origin of the annihilation event. As photons loose energy during the scattering process, detection of these scatter events can be reduced considerably by analyzing only photons with energies close to 511 keV. Furthermore, the remaining scatter distribution can be estimated incorporating a single scatter model into image reconstruction (Watson, 2000). If two annihilation events occur nearly at the same time and in each case one photon is absorbed in the object, the two remaining photons may generate a random event and the assigned LOR is generally not related to the two annihilation origins. To reduce random events, the timing window of the coincidence detection can be narrowed. Using a second coincidence circuit with delayed timing window enables direct measurement of the statistical distribution of random events allowing for correction of PET data (Brasse et al., 2005).

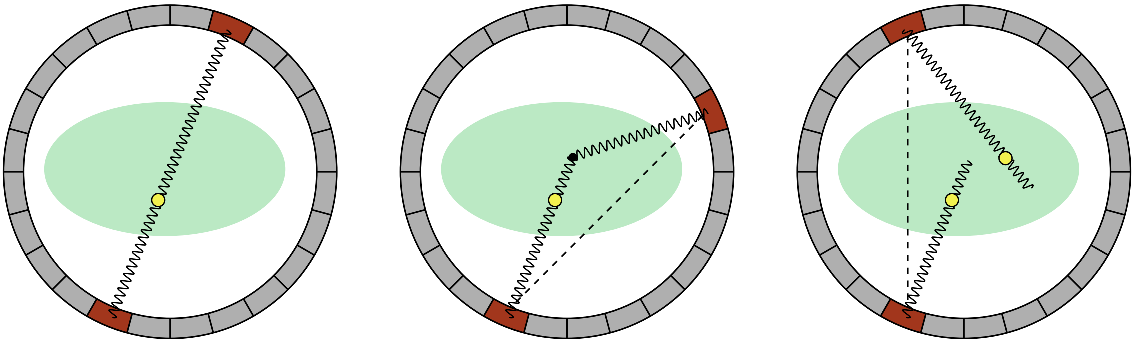
(a) true event **(b)** scatter event **(c)** random event

Figure 2.10: Overview of different types of events measured in PET.

2.3 Image Registration

Image registration describes the process of aligning two or more images. It aims at finding a geometric transformation that matches selected structures of these images. The image to be deformed by this transformation is defined as the source image $\boldsymbol{f}_{\mathrm{S}}$ while the static image is called destination image $\boldsymbol{f}_{\mathrm{D}}$. Comprehensive surveys of image registration are given in Gottesfeld Brown (1992), Hill et al. (2001), Zitová and Flusser (2003), Wyawahare et al. (2009) and Oliveira and Tavares (2014). In the field of medical imaging, typical applications of image registration comprise:

- Alignment of images of the same patient acquired with different FOVs or image orientations.
- Detection of changes between images of the same patient examined at different times.
- Fusion of information from different imaging modalities, such as CT, MRI and PET.
- Description of transformations between different motion states, e. g. in case of images affected by respiratory or cardiac motion.
- Transfer of information between two different patients, e. g. to add bone information to attenuation maps in simultaneous PET/MR imaging (Burgos et al., 2014; Paulus et al., 2015).

As medical image registration is employed for a wide range of applications, methods are typically adapted to specific requirements and body regions (Wyawahare et al., 2009; Oliveira and Tavares, 2014). However, most methods can be subdivided into a set of similar steps. In a first step, certain features are extracted from the source and destination images. These features may be defined in the image domain and may e. g. describe voxel intensities, edges, contours, landmark points or regions with closed boundaries. In general, feature space can also be defined in the projection or frequency domain. In a second step, a similarity metric is chosen that correlates information from the source and the destination image. This metric may quantify the physical distance of features in the two images or it may compare voxel intensities of the images. For the latter, typical approaches seek to minimize the sum of squared differences or to maximize the cross-correlation or mutual information, respectively. The third step estimates the transformation of the source image to match the destination image. Several types of transformations exist. Figure 2.11 illustrates two examples. While rigid transformations are restricted to translation and rotation in all spatial dimensions, affine transformations allow for additional shearing and scaling of the source image. Moreover, deformable transformations assign each voxel with an individual displacement and thus enable more complex deformation models. The type of transformation has to be chosen specifically for a given problem. This selection usually represents a trade-off between a high degree of freedom of the transformation and the robustness of the registration process. In many algorithms, the transformation parameters are estimated iteratively optimizing a cost function, which contains the similarity metric chosen in step two. In the fourth step, the source image may be transformed to the geometry of the destination image. As medical images are typically of discrete nature, interpolation has to be applied to compute values at defined grid positions. Common methods comprise linear or cubic spline interpolation.

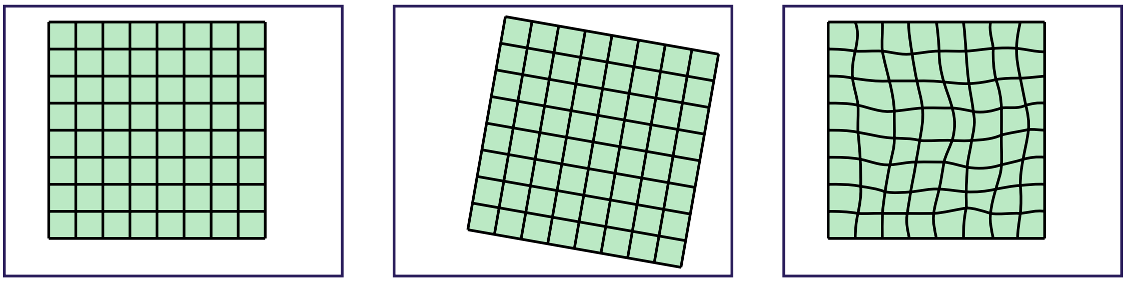

(a) original image **(b)** rigid transformation **(c)** deformable transformation

Figure 2.11: Examples of two different types of image transformations. While rigid transformations (b) are restricted to translation and rotation in all spatial dimensions, deformable transformations (c) assign each voxel with an individual displacement enabling more complex deformations.

In this work, image registration is employed to estimate transformations that describe motion between different respiratory or cardiac phases. Due to their complexity, these types of motion are modeled with deformable transformations. The resulting voxel-specific motion vector fields (MVFs) are defined by a transformation operator T that is composed of the identity mapping and a displacement vector field $\boldsymbol{d}$:

$$T : (x, y, z) \to (x, y, z) + \boldsymbol{d}(x, y, z). \tag{2.37}$$

Applying the transformation operator T to a source image $\boldsymbol{f}_\mathrm{S}$ results in the destination image $\boldsymbol{f}_\mathrm{D}$. This procedure can be described by a destination-driven deformation:

$$\boldsymbol{f}_\mathrm{D}(x, y, z) = T\boldsymbol{f}_\mathrm{S}(x, y, z) = \boldsymbol{f}_\mathrm{S}((x, y, z) + \boldsymbol{d}(x, y, z)). \tag{2.38}$$

To find a suitable transformation operator T, a cost function similar to the following is optimized:

$$C_\mathrm{Reg}(T) = \|\boldsymbol{f}_\mathrm{D} - T\boldsymbol{f}_\mathrm{S}\|_2^2 + R(T). \tag{2.39}$$

The first term of the cost function optimizes the similarity between the destination image and the deformed source image. While Eq. (2.39) employs the sum of squared distances as similarity metric, other measures such as mutual information can be implemented as well. Similar to the iterative image reconstruction in Eq. (2.22), the second term imposes penalties on the properties of the transformation operator T. This regularization ensures smoothness of the resulting deformation vector field, for instance.

2.4 Respiratory and Cardiac Motion Management

Patient motion during measurements is one major challenge for data acquisition and image reconstruction. Depending on the body region, different motion types and corresponding correction techniques exist. This work has a focus on thoracic and abdominal imaging, for which respiratory and cardiac motion is most important. In contrast to random motion, such as coughing, these motion types describe cyclic patterns. Although different motion cycles slightly vary, preservation of this property can be assumed in most cases when averaging over several motion cycles. For respiratory motion, common peak to peak amplitudes in the two main directions of motion were reported to be in the range of 6 to 20 mm in superior-to-inferior direction and 1 to 11 mm in anterior-to-posterior direction, respectively (Ionascu et al., 2007). Typical breathing periods are approximately 2.6 to 4.8 s (Quirk et al., 2013), which translates into frequencies of 0.4 to 0.2 Hz. An additional property of respiratory physiology is called hysteresis inducing that internal structures follow different motion paths during inhalation and during exhalation (McClelland et al., 2013). For cardiac motion, typical heart rates at rest are in the range of 60 to 100 Hz. A mean displacement of about 3 to 8 mm between end-diastole and end-systole was reported for cardiac structures and coronary arteries in Tan et al. (2013). However, these values as well as left and right ventricular volumes depend on the respiratory motion phase due to coupling of respiratory and cardiac motion (Claessen et al., 2014).

A general overview of motion correction methods for MRI is given in Wang and Amini (2012) and McClelland et al. (2013) while techniques for simultaneous PET/MR imaging are discussed in Catana (2015) and Munoz et al. (2016).

2.4.1 Prospective Approaches

Prospective motion management aims at controlling data acquisition to reduce motion artifacts and blurring in the reconstructed images. In case of MRI, several different approaches are available. Regarding k-space sampling, non-Cartesian trajectories, e. g. radial patterns, can be employed. As described in section 2.1.4, ghosting can be strongly reduced compared to Cartesian patterns. One option to minimize respiratory motion blurring is MR data acquisition in breath-hold (Paling and Brookeman, 1986). This, however, limits acquisition times to about 10 to 15 s making the acquisition of 3D volumes with a large number of slices difficult. Moreover, respiratory time-resolved MRI cannot be realized using breath-hold acquisitions. Triggered MR acquisition represents a technique, which can be applied to reduce either respiratory or cardiac motion blur. With this technique, data are acquired only when the subject is in a predefined motion state. To estimate this motion state, a motion surrogate signal has to be acquired during the measurement. For that purpose, external devices such as compressible cushions or pneumatic belts for respiratory signals (Arnold et al., 2007) and electrocardiography (ECG) for cardiac signals (Rokey et al., 1988; Fischer et al., 1999) can be employed. In addition, MRI allows for intrinsic estimation of motion amplitudes using navigators (McClelland et al., 2013) or from the k-space center signal when using radial acquisitions (Larson et al., 2004, 2005). A disadvantage of triggered acquisition is the reduced efficiency of the measurement prolonging acquisition times. In clinical practice, cardiac examinations are generally performed during breath-hold or with triggered respiratory gating. Data acquisition is then synchronized with the heartbeat of the patient (Earls et al., 2002). Thus several k-space lines can be acquired for predefined phases of the cardiac cycle during each heartbeat. The position of k-space lines is chosen in such a way, that after several heartbeats the full specified k-space is filled with data.

In addition to these segmented k-space acquisition strategies, real-time MRI represents another state-of-the-art technique providing high temporal resolution (Zhang et al., 2010b; Uecker et al., 2012; Feng et al., 2013; Zhang et al., 2014). However, image acquisition is typically limited to a single slice with reduced spatial resolution due to the ultrafast acquisition. When repeating the acquisition at varying slice locations, temporal consistency of the imaged motion cycles is not preserved. In contrast to the variety of methods for MR data acquisition, the nature of PET data acquisition does not allow for prospective motion management, but retrospective approaches can be applied.

2.4.2 Retrospective Approaches

Retrospective approaches for motion handling are quite similar between the different imaging modalities MRI, PET and CT, as they are less dependent on the data acquisition process. The most widely used strategy is gating. As shown in Fig. 2.12, the motion cycle is divided into several motion phases and the acquired data are sorted into these different motion bins. This sorting requires that the acquired data can be subdivided into small subsets. Furthermore, a motion surrogate signal has to be acquired during the measurement or it has to be estimated intrinsically from the measured data as described in the previous section 2.4.1. After sorting, images are reconstructed from the data of each individual phase separately. Hence, gating typically represents a trade-off between acquisition time and an appropriate signal-to-noise ratio (SNR), contrast and artifact level of the reconstructed images. To reduce artifact levels of gated images in MRI, iterative compressed sensing–based approaches as explained in section 2.1.7 are typically applied (Lustig et al., 2007, 2008; Hollingsworth, 2015). Furthermore, MoCo image reconstruction has been proposed to overcome limitations of gating (Batchelor et al., 2005; Odille et al.,

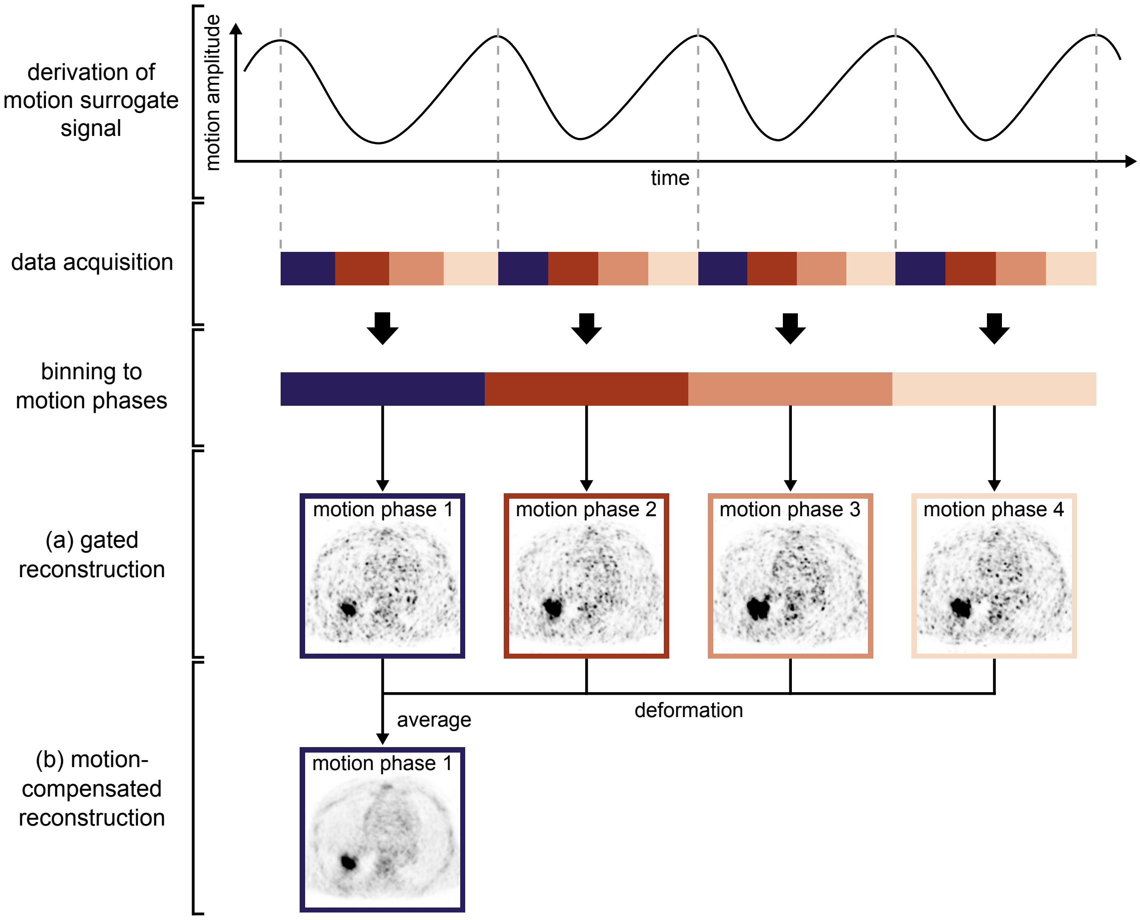

Figure 2.12: Schematic illustration of two approaches for retrospective motion handling: (a) For gated reconstructions, the acquired data are sorted into different motion phase bins and images are reconstructed from the data of each individual phase separately. (b) For MoCo reconstructions, the gated images corresponding to different motion phases are deformed to a desired motion phase and averaged. Thus 100% of the measured data can be employed for reconstruction of each individual phase. For convenience, MoCo reconstruction is only shown for a single motion phase.

2008; Wang and Amini, 2012; McClelland et al., 2013). In contrast to gated reconstructions, this approach uses 100% of the measured data for the reconstruction of each individual phase. For that purpose, gated images of the different motion phase are deformed to the desired motion phase and averaged as illustrated in Fig. 2.12. For this procedure, estimation of MVFs, which specify the displacement in the three spatial dimensions between motion phases for each voxel, is required. To obtain the MVFs, image registrations between reconstructions of the different motion phases are typically performed. The quality of resulting MoCo images directly depends on the accuracy of MVFs and therefore robust motion estimation methods are required, especially when using undersampled data and thus artifact-contaminated images for registration.

3 | Materials and Methods

In this chapter, important methods used for image reconstruction and data generation and processing are introduced. Sections 3.1 and 3.2 describe algorithms for MR and PET image reconstruction developed in this work. Section 3.3 presents methods for simulation of MR and PET data. Furthermore, it specifies the protocols used for acquisition of volunteer and patient data. In section 3.4, preprocessing of MR and PET data is illustrated. An overview of the studies conducted in this work is given in section 3.5.

3.1 MR Image Reconstruction Algorithms

3.1.1 Gridding Reconstruction

For analytic reconstruction of radial MR data, gridding of these data onto a rectilinear grid as described in section 2.1.6 is performed. Using all acquired data, reconstruction of the image $\boldsymbol{f}$ corresponds to the 3D motion average and is described as follows:

$$\boldsymbol{f} = S^{\dagger}\mathsf{X}^{\dagger}\boldsymbol{p}. \tag{3.1}$$

The vector $\boldsymbol{p} = (\boldsymbol{p}_1, \boldsymbol{p}_2, \ldots, \boldsymbol{p}_J)^T$ describes the measured raw data of all coil channels J. The pseudo-inverse operator $\mathsf{X}^{\dagger}$ corresponds to the gridding operation. A Kaiser-Bessel window (Kaiser, 1974) was used as gridding kernel. For density compensation, a Ram-Lak kernel (Ramachandran and Lakshminarayanan, 1971) was employed. The transformation to image space was obtained by an inverse Cartesian FFT. The operator $S^{\dagger}$ describes the combination of the different coil channels and is defined in Eq. (3.24) (Bydder et al., 2002).

Taking temporal dimensions into account, the 5D double-gated reconstruction $\boldsymbol{f}_{r,c}$ of respiratory motion phase r and cardiac motion phase c is obtained as follows:

$$\boldsymbol{f} = S^{\dagger}\mathsf{X}^{\dagger}G_r G_c \boldsymbol{p}. \tag{3.2}$$

The operators G_r and G_c act as respiratory and cardiac gating operators on the raw data. Thus radial spokes not belonging to the current respiratory phase r or cardiac phase c

are excluded from the reconstruction. In case only respiratory gating is desired, e. g. for 4D respiratory gated reconstructions, the cardiac gating operator G_c becomes the identity matrix. Setting both operators to identity leads to results identical to Eq. (3.1).

3.1.2 Joint Motion Estimation and Image Reconstruction: 4D joint MoCo-HDTV

The 4D joint motion-compensated high-dimensional total variation (joint MoCo-HDTV) algorithm represents the basis of all studies conducted in this work. It is derived from the high-dimensional total variation (HDTV) algorithm originally developed for time-resolved reconstruction of undersampled CT data (Ritschl et al., 2012). The original HDTV algorithm shares similarities with many compressed sensing–based MR reconstruction algorithms exploiting sparsity of the image in spatial and/or temporal TV domain, such as proposed by Block et al. (2007), Lustig et al. (2007), Feng et al. (2014), Montesinos et al. (2014), Cruz et al. (2016) and Feng et al. (2016a).

The novelty of this work is the extension of this algorithm using MoCo MR image reconstruction in conjunction with artifact-robust motion estimation. These methods are embedded in a framework of joint motion estimation and image reconstruction. An illustration of the algorithm is given in Fig. 3.1. The algorithm alternates between estimation of the desired image and the MVFs using a multiresolution strategy. The motivation behind the alternating estimation is that the updated image of a given resolution level improves the quality of motion estimation, resulting in more accurate MVFs, which in turn improve the image reconstruction of the next resolution level. The algorithm has been developed to resolve a single temporal dimension, which can be either the respiratory dimension r or the cardiac dimension c. Thus for generalization, the variable t represents the temporal dimension in the following.

Cost Function and Update Equation

As described in section 2.1.7, image reconstruction is considered as an inverse problem and the following cost function is optimized in an alternating manner for each resolution level:

$$C_{\mathrm{HDTV}}(\boldsymbol{f}) = \|\mathsf{X}_{\mathrm{PC}} S \boldsymbol{f} - \boldsymbol{p}\|_2^2 + \eta \, \mathrm{HDTV} \, \boldsymbol{f}. \tag{3.3}$$

The operator X_{PC} represents a sparse matrix. Its diagonal elements $\mathsf{X}_{\mathrm{PC},t}$ describe the motion phase–correlated forward transform of each component of the 4D image volume $\boldsymbol{f} = (\boldsymbol{f}_1, \boldsymbol{f}_2, \ldots, \boldsymbol{f}_{N_t})^{\mathrm{T}}$ to its corresponding radial spoke positions in k-space. Applying a Cartesian FFT to each component of the 4D image volume, raw data values at radial spoke positions are calculated by resampling with bilinear interpolation in k-space. The operator

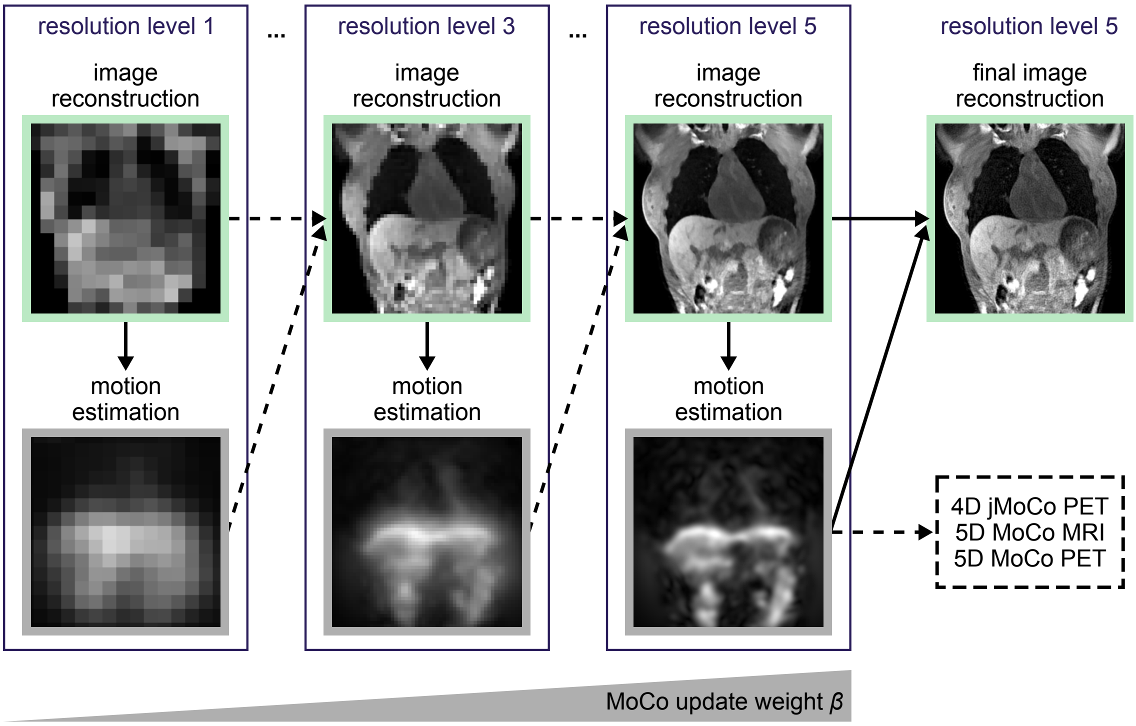

Figure 3.1: Overview of the 4D joint MoCo-HDTV algorithm alternating between image reconstruction and motion estimation at different resolution levels. The MVFs of the highest resolution level can be employed for MR or PET MoCo image reconstructions.

S performs a multiplication of the complex-valued sensitivity profiles defined by Eq. (3.23) for each coil channel with the image volume $\boldsymbol{f}$ creating complex-valued volumes for each combination of motion phase t and coil channel j. While the vector $\boldsymbol{p} = (\boldsymbol{p}_1, \boldsymbol{p}_2, \ldots, \boldsymbol{p}_J)^{\mathrm{T}}$ denotes the measured raw data of the different coil channels, the parameter η weights the regularization term, which is defined as the spatio-temporal total variation HDTV $\boldsymbol{f}$. The first term of Eq. (3.3) corresponds to the raw data comparison and leads to the following update $\boldsymbol{u}_t^{(n+1)}$ of motion phase t for iteration $n+1$:

$$\boldsymbol{u}_t^{(n+1)} = S^{\dagger} \mathsf{X}^{\dagger}_{\mathrm{PC},t} (\mathsf{X}_{\mathrm{PC},t} S \boldsymbol{f}_t^{(n)} - G_t \, \boldsymbol{p}). \tag{3.4}$$

Instead of using the complex conjugated transposed transform $\mathsf{X}^{\mathrm{T}}_{\mathrm{PC},t}$, the pseudoinverse $\mathsf{X}^{\dagger}_{\mathrm{PC},t}$ is used instead, which is called preconditioning. In correspondence to Eq. (3.2), application of $\mathsf{X}^{\dagger}_{\mathrm{PC},t}$ performs a motion phase–correlated gridding reconstruction with density compensation. Employing Eq. (3.4), the updated image volume $\boldsymbol{f}_t^{(n+1)}$ of motion phase t is then obtained as follows:

$$\boldsymbol{f}_t^{(n+1)} = \boldsymbol{f}_t^{(n)} + \alpha \left((1-\beta) \boldsymbol{u}_t^{(n+1)} + \beta \frac{1}{N_t} \sum_{t'} D^t_{t'} \boldsymbol{u}_{t'}^{(n+1)} \right). \tag{3.5}$$

The parameter α defines the update step size and it was set to 0.5 in this work, which ensures a smooth convergence over several iterations. The weighting of both update terms is specified by the parameter β. The first update term represents a direct update from the raw data comparison and it is independent of the quality of the estimated MVFs. However, it might introduce streak artifacts caused by undersampling, as only raw data of motion phase t are employed for the update. In contrast, the second update term performs a MoCo update using 100% of raw data for the update and therefore produces less streak artifacts. The operator $D_{t'}^{t}$ is defined in Eq. (3.9) and describes a deformation of the volume from motion phase t' to motion phase t. For this deformation, tricubic interpolation is employed applying the dedicated MVFs. Thus the second update term describes a superimposition of the updates of all N_t motion phases warped to phase t.

As demonstrated in Fig. 3.2, the MoCo update improves sparsity in the HDTV domain as streak artifacts and noise are reduced resulting in a more compact representation in this domain. However, for inaccurate MVFs, the update volume of the second term might introduce blurring and spurious motion. This requires a careful choice of the parameter β. As described below, a multiresolution strategy can be pursued to overcome this problem.

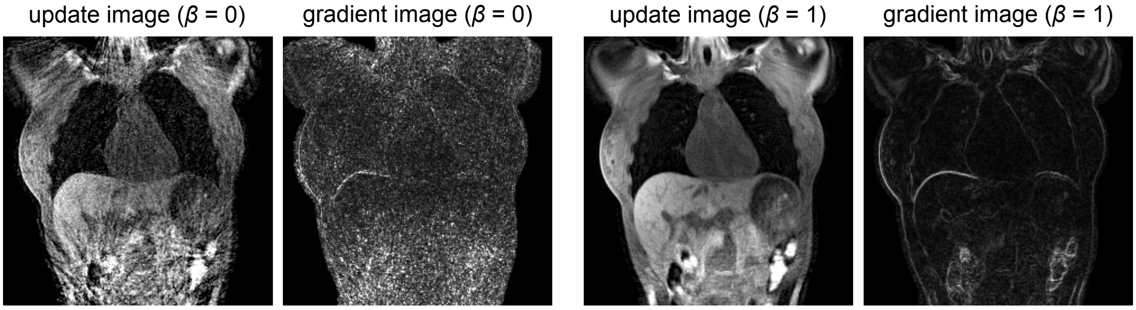

Figure 3.2: Example of image updates employing Eq. (3.5) for $\beta = 0$ (left) and $\beta = 1$ (right) and corresponding spatio-temporal gradient images in the HDTV domain applying Eq. (3.6) to the update images. The image updates were computed for a zero-filled initial image using the constant value $\bar{v}_{x,y,z}\Delta r = 1.0\,\mathrm{mm}$ in Eq. (3.6) for calculation of both gradient images. The lower intensities in the gradient image for $\beta = 1$ demonstrate that employing the MoCo update in the update equation (Eq. (3.5)) improves sparsity of the update image in the HDTV domain. Note that both gradient images are displayed at equal intensity windows. Adopted from Rank et al. (2016a).

Multiresolution Strategy

Starting at an initial low-resolution level, at which streak artifacts are less pronounced, an image estimate is reconstructed as illustrated in Fig. 3.1 employing the weight $\beta = 0$ in Eq. (3.5). After convergence of this first image reconstruction step, an initial estimation of MVFs is performed. The next higher resolution level is treated separately and image reconstruction is initialized with a smoothed version of the image estimate of the previous resolution level. The MVFs are upsampled to the new resolution and to ensure convergence of the cost function, they are kept constant during the image reconstruction. For each step in resolution, the weighting parameter β is increased gradually. This is motivated by an improvement of the accuracy of MVFs on the one hand and increased streak artifact levels on the other hand for high-resolution levels. In this work, five resolution levels with base resolutions of 16, 32, 64, 128 and 256 px were used for the alternating approach shown in Fig. 3.1. The parameter β was varied linearly between 0 and 0.65. For the reconstructions conducted in this work, the upper limit of 0.65 represented an appropriate trade-off between the appearance of streak artifacts caused by low values and error propagation through resolution levels caused by large values.

Adaptive Spatio-Temporal Regularization

After calculating the image update from the raw data comparison described in Eq. (3.5), the spatio-temporal sparsity of the image is optimized, which corresponds to the second term of Eq. (3.3). For that purpose, a conjugate gradient descent algorithm with 15 to 20 gradient steps was employed, which is described in more detail in Ritschl et al. (2011) and Ritschl et al. (2012). The HDTV operator specifies the weighted spatio-temporal gradient of the image volume $\boldsymbol{f}(x,y,z,t)$ at position (x,y,z,t):

$$\begin{aligned}\mathrm{HDTV}\,\boldsymbol{f} &= \|\nabla_{x,y,z,t}\,\boldsymbol{f}\|_{1,2}\\ &= \sum_{xyzt}\Bigg(\frac{1}{\Delta x^2}(f_{x,y,z,t}-f_{x-1,y,z,t})^2+\frac{1}{\Delta y^2}(f_{x,y,z,t}-f_{x,y-1,z,t})^2\\ &\quad+\frac{1}{\Delta z^2}(f_{x,y,z,t}-f_{x,y,z-1,t})^2+\frac{\gamma_t^2}{\bar{v}_{x,y,z}^2\,\Delta t^2}(f_{x,y,z,t}-f_{x,y,z,t-1})^2\Bigg)^{1/2}.\end{aligned} \tag{3.6}$$

The parameters $\Delta x, \Delta y, \Delta z$ are defined as the spatial distances between neighboring voxels and Δt denotes the interval between motion phases in temporal dimension. The factor γ_t scales the contribution of the temporal TV. To increase the influence of the temporal regularization, it was set to 1.2 for all reconstructions. The parameter $\bar{v}_{x,y,z}$ can be interpreted as the average motion velocity and it is derived as follows:

$$\bar{v}_{x,y,z} = \frac{1}{N_t\,\Delta t}\sum_t \sqrt{(\Delta x^2\,\mathrm{MVF}_x(x,y,z,t)^2+\Delta y^2\,\mathrm{MVF}_y(x,y,z,t)^2)+\Delta z^2\,\mathrm{MVF}_z(x,y,z,t)^2}. \tag{3.7}$$

The variable N_t specifies the total number of motion phases and the vector $\mathrm{MVF}_{xyz}(x,y,z,t)$ contains the voxel displacement in the three spatial dimensions between adjacent motion phases. Hence, the larger the average motion velocity at a voxel position, the smaller the weighting of the temporal TV and vice versa. Examples of spatio-temporal gradient images in the HDTV domain are given in Fig. 3.2. Applying the HDTV regularization results in denoising and in a reduction of streak artifacts by spatio-temporal smoothing of the image.

Furthermore, the regularization may correct for local errors induced by inaccurate MVFs. At the end of each iteration, the combination weight between the update of the raw data comparison and the spatio-temporal image regularization is calculated adaptively (Ritschl et al., 2011). This prevents overregularization of the image and ensures a convex behavior of the image reconstruction. The iterative optimization of Eq. (3.3) at a given resolution level will stop if the improvement of raw data fidelity ϵ between adjacent iterations is smaller than a threshold:

$$|\epsilon^{(n)} - \epsilon^{(n+1)}| < 0.005\,\epsilon^{(n)} \quad \text{with } \epsilon^{(n)} = \|\mathsf{X}_{\mathrm{PC}} \boldsymbol{S} \boldsymbol{f} - \boldsymbol{p}\|_2^2. \tag{3.8}$$

Cyclic Motion Estimation

After performing the image reconstruction step of one resolution level, an update of the MVFs is calculated employing the recent image estimate for motion estimation (Fig. 3.1). The registration process is initialized using the MVFs from the previous resolution level. Instead of using a standard motion estimation approach, which estimates MVFs between any combination of motion phases (Fig. 3.3 a), a cyclic motion pattern is assumed and therefore MVFs are only estimated between adjacent motion phases (Brehm et al., 2012) (Fig. 3.3 b). The image registration is based on the demons algorithm (Thirion, 1998; Vercauteren et al., 2009) optimizing a cost function similar to Eq. (2.39). This algorithm allows for deformable transformations and employs the sum of squared differences as similarity metric. During each iteration of the registration process, a fluid-like and diffusion-like regularization, implemented as a binomial filtering, is applied to the MVFs. To improve robustness of the image registration, the demons algorithm pursues a hierarchical approach using different resolution levels, not to be confused with the multiresolution strategy used for joint motion estimation and image reconstruction.

After the cyclic registration process, the MVFs are further regularized by cyclic constraints demanding that each voxel returns to its initial position after passing one full motion cycle. This cyclic self-consistency criterion increases the robustness of the registration against streak artifacts in the image considerably as demonstrated in Brehm et al. (2012). Having ensured cyclic consistency of MVFs, a deformation operator $D_1^{N_t}$ between any nonadjacent motion phases $t = 1$ and $t' = N_t$ can be generated by noncommutative concatenation of adjacent transformation operators T_t^{t+1}:

$$D_1^{N_t} = \prod_{t=1}^{N_t - 1} T_t^{t+1} = T_1^2 \circ T_2^3 \circ \ldots \circ T_{N_t - 1}^{N_t}. \tag{3.9}$$

When using the estimated MVFs for MoCo PET reconstructions, the resulting images are referred to as 4D motion-compensated PET based on joint MoCo-HDTV (jMoCo PET).

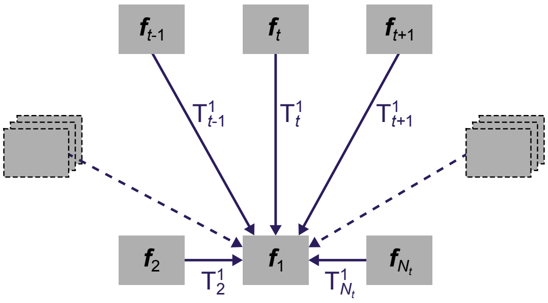

(a) standard motion estimation

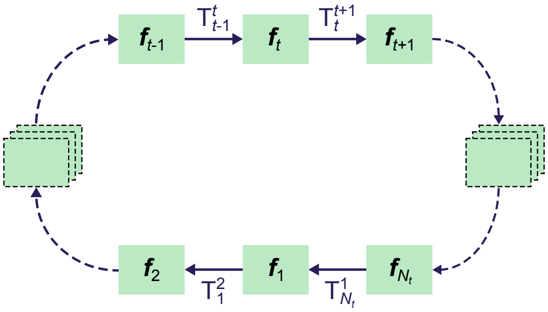

(b) cyclic motion estimation

Figure 3.3: Comparison of two motion estimation strategies: For the standard approach (a), MVFs are estimated between all possible combinations of motion phases t and t'. For the cyclic approach (b), MVFs are calculated only between adjacent motion phases t and $t+1$ assuming a cyclic motion pattern.

Final Reconstruction

After estimation of MVFs at the highest resolution level (Fig. 3.1), a further image reconstruction step is performed using the weight $\beta = 1$ and thus only the MoCo update term in Eq. (3.5). Furthermore, the HDTV regularization term is disabled employing $\eta = 0$ in Eq. (3.3) to increase image sharpness. The resulting final image volume is then referred to as 4D joint MoCo-HDTV.

3.1.3 4D Respiratory Time-Resolved MRI from Literature

For comparison purposes, additional image reconstructions using the original HDTV algorithm were performed. For that purpose, only the first update term of Eq. (3.5) with $\beta = 0$ was considered and the motion estimation step was omitted, thus employing a constant velocity map $\bar{v}_{x,y,z}\,\Delta t = 1.0\,\text{mm}$ in Eq. (3.6). All other parameters were identical to the 4D joint MoCo-HDTV reconstructions.

Furthermore, the motion-adaptive spatio-temporal regularization (MASTeR) algorithm (Asif et al., 2013) was implemented. This algorithm combines iterative image reconstruction and motion compensation and it was specifically developed for time-resolved MRI with strong undersampling. In the initialization step, a first image estimate has to be computed. For this purpose, the 4D HDTV reconstruction was used. In the motion adaptation step, estimation of interframe motion and image reconstruction are performed in an alternating manner. Interframe motion was estimated with the same registration methods as used for 4D joint MoCo-HDTV employing the cyclic motion estimation described in section 3.1.2. For reconstruction of the image $\boldsymbol{f}$, the following cost function is optimized:

$$C_{\text{MASTeR}}(\boldsymbol{f}) = \sum_t \|\mathsf{X}_{\text{PC},t} S \boldsymbol{f}_t - G_t \boldsymbol{p}\|_2^2 + \eta(\|F_{t-1}\boldsymbol{f}_{t-1} - \boldsymbol{f}_t\|_1 + \|B_{t+1}\boldsymbol{f}_{t+1} - \boldsymbol{f}_t\|_1). \quad (3.10)$$

The operators and variables are defined in accordance to Eq. (3.3). The operator $\mathsf{X}_{\text{PC},t}$ denotes the motion phase–correlated forward transform of the image $\boldsymbol{f}_t$ for motion phase t while the operator S performs a multiplication of the complex-valued sensitivity profiles as defined in Eq. (3.23) with the image volume $\boldsymbol{f}_t$ creating complex-valued volumes for each coil channel j. The regularization terms are weighted by η while the operators F_t and B_t describe forward and backward motion operators, respectively. These operators warp an image $\boldsymbol{f}_t$ from motion phase t to $t+1$ and vice versa. In this work, the cost function in Eq. (3.10) was optimized with identical optimization methods as employed for HDTV and joint MoCo-HDTV. As proposed in the original publication, three motion-adaptation iterations of MASTeR were performed. Resulting images are referred to as 4D MASTeR.

3.1.4 5D Respiratory and Cardiac Motion Compensation

Estimation of Respiratory Motion

Respiratory and cardiac motion are estimated sequentially as proposed in Brehm et al. (2015) and Sauppe et al. (2016). For estimation of respiratory motion, the MR raw data are divided into N_r respiratory motion phases while cardiac motion is neglected as illustrated in Fig. 3.4 a. With this gating scheme, each respiratory motion phase consists of raw data from all cardiac phases assuming an approximately uniform distribution among the different respiratory phases. The respiratory MVFs are obtained from reconstructions with the 4D joint MoCo-HDTV algorithm as described in section 3.1.2.

Estimation of Cardiac Motion

To allow for robust estimation of MVFs in the cardiac dimension, MR data originating from all respiratory phases have to be employed due to the high artifact and noise level of double-gated images. The studies in Brehm et al. (2015) and in Sauppe et al. (2016) have utilized the respiratory MVFs to create respiratory MoCo and cardiac gated images and have used these images for registration.

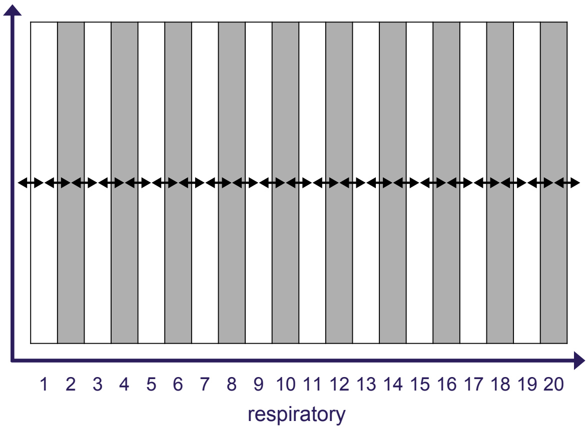

(a) respiratory motion estimation

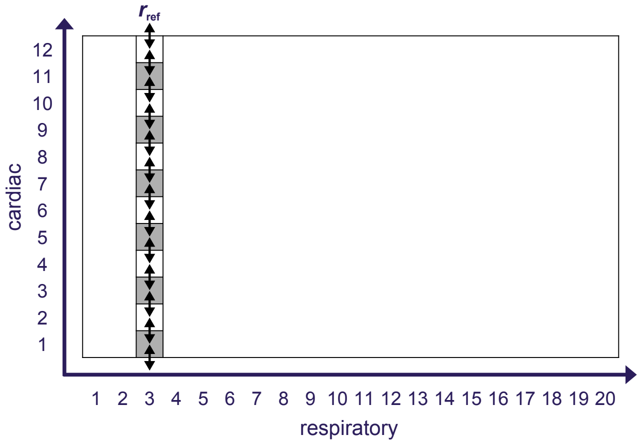

(b) cardiac motion estimation

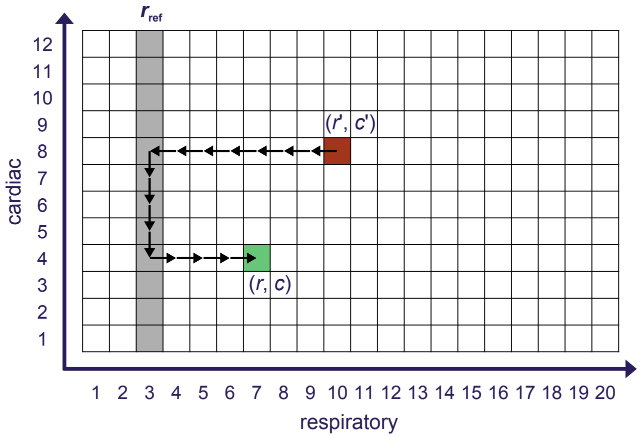

(c) MoCo reconstruction

Figure 3.4: Sequential estimation of respiratory and cardiac patient motion: (a) Gating scheme used for estimation of respiratory motion. The black arrows illustrate motion estimation between adjacent motion phases. (b) Respiratory MoCo raw data are generated for a respiratory reference phase and cardiac MVFs are estimated between adjacent cardiac phases. (c) For 5D respiratory and cardiac MoCo reconstruction, any source phase (red) is transformed along the deformation path indicated by the black arrows to the destination phase (green) in passing the respiratory reference phase (gray). Adopted from Rank et al. (2016b).

To make use of 100% of the available information for cardiac motion estimation, the generation of respiratory MoCo raw data is proposed as an alternative approach in this work (Fig. 3.4 b). For this purpose, double-gated gridding reconstructions are carried out for all coil channels j. Corresponding to the estimation of respiratory motion, MR raw data are sorted into N_r respiratory motion bins and into N_c cardiac motion bins. For a given cardiac phase c, all related combinations (r, c) are deformed to a respiratory reference motion phase (r_{ref}, c) and averaged. In this work, an end-exhale motion phase was chosen as respiratory reference in order to provide the lowest respiratory intraphase blurring. The resulting respiratory MoCo and cardiac gated complex-valued coil images are then forward transformed to k-space in the following manner:

$$\boldsymbol{p}_{j,r_{\text{ref}},c}^{\text{resp MoCo}} = \mathsf{X}_{\text{Nyq}} \sum_{r} D_r^{r_{\text{ref}}} \mathsf{X}^{\dagger} G_r G_c \, \boldsymbol{p}_j . \tag{3.11}$$

The raw data of coil channel j are represented by $\boldsymbol{p}_j$. The operator X_{Nyq} performs a forward transform of the respiratory MoCo and cardiac gated complex-valued coil images to generate radial k-space data. The number of spokes used for the forward transform was chosen to satisfy the Nyquist criterion for radial MR acquisitions using a uniform angular distribution of radial spokes. This approach prevents the introduction of sampling-related artifacts in contrast to a forward transform using the measured spoke angles, which generally do not satisfy the Nyquist criterion nor have a uniform angular distribution. Based on the generated respiratory MoCo raw data of the different cardiac motion phases, cardiac MVFs are estimated employing the 4D joint MoCo-HDTV algorithm in the cardiac dimension. The deformation operator $D_r^{r_{\text{ref}}}$ is defined in Eq. (3.9).

Evaluation of Generation of Respiratory MoCo Raw Data

To demonstrate the advantage of generating respiratory MoCo raw data and applying the 4D joint MoCo-HDTV algorithm for cardiac motion estimation, cardiac MVFs were also estimated on basis of respiratory MoCo and cardiac gated images in the respiratory reference motion phase without employing 4D joint MoCo-HDTV. Both approaches employed the cyclic image registration described in section 3.1.2 with identical parameter settings.

Representative results of cardiac MVFs estimated with both approaches are shown in Fig. 3.5. The cardiac MVFs of the image-based approach reveal severe spurious motion in regions outside the heart caused by residual streak artifacts in the respiratory MoCo and cardiac gated images. As these artifacts change their position in each cardiac phase, artificial motion is introduced during the registration process. Interfering with the true cardiac motion, this also yields an underestimation of the latter. In contrast, results of the approach with generated respiratory MoCo raw data are not affected by spurious motion and cardiac MVFs show large entries only inside the heart.

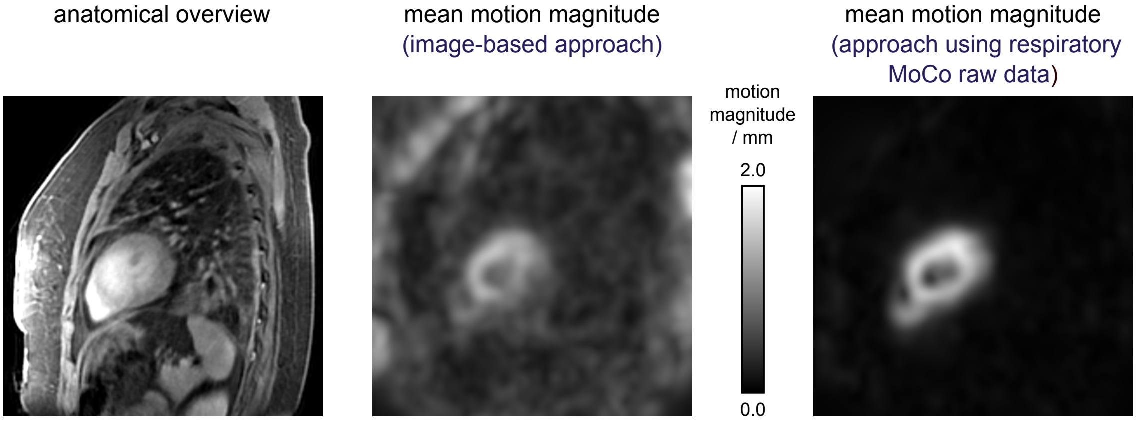

Figure 3.5: Comparison of cardiac MVFs estimated with the image-based approach and with the approach using respiratory MoCo raw data. The mean motion magnitude represents the motion magnitude averaged over all cardiac motion phases. The image-based approach reveals spurious motion in regions outside the heart caused by residual streak artifacts in the image while the approach using respiratory MoCo raw data for motion estimation is not affected by these distortions.

5D MoCo Image Reconstruction

Having estimated respiratory and cardiac MVFs, MoCo image reconstruction can be performed. Applying the estimated MVFs to gated or double-gated gridding reconstructions, images of all motion phases are warped onto a desired reconstruction phase and averaged, i. e. 100% of the measured raw data are employed for reconstruction. To perform a 4D respiratory MoCo reconstruction, the image volume $\boldsymbol{f}_r$ of respiratory phase r is calculated as follows:

$$\boldsymbol{f}_r = \sum_{r'} D^{r}_{r'} S^{\dagger} \mathsf{X}^{\dagger} G_{r'} \boldsymbol{p}. \tag{3.12}$$

A 5D respiratory MoCo and cardiac gated image $\tilde{\boldsymbol{f}}_{r,c}$ of respiratory and cardiac phase (r, c) is reconstructed as follows:

$$\tilde{\boldsymbol{f}}_{r,c} = \sum_{r'} D^{r}_{r'} S^{\dagger} \mathsf{X}^{\dagger} G_{r'} G_c \boldsymbol{p}. \tag{3.13}$$

Accordingly, 5D respiratory and cardiac MoCo images $\hat{\boldsymbol{f}}_{r,c}$ are obtained as follows:

$$\hat{\boldsymbol{f}}_{r,c} = \sum_{r',c'} D^{r,c}_{r',c'} S^{\dagger} \mathsf{X}^{\dagger} G_{r'} G_{c'} \boldsymbol{p}. \tag{3.14}$$

The deformation operator $D^{r,c}_{r',c'}$ is generated in accordance to the following decomposition proposed in Brehm et al. (2015) and Sauppe et al. (2016):

$$D^{r,c}_{r',c'} = D^{r_{\mathrm{ref}}}_{r'} \circ D^{r_{\mathrm{ref}},c}_{r_{\mathrm{ref}},c'} \circ D^{r}_{r_{\mathrm{ref}}}. \tag{3.15}$$

Figure 3.4 c illustrates the virtual deformation path between the combination (r', c') and the combination (r, c) as an example. In a first step, the source volume is warped along the respiratory direction from (r', c') to the respiratory reference phase (r_{ref}, c'). While remaining in this respiratory reference phase, the volume is deformed along the cardiac direction in the second step to match the cardiac destination phase (r_{ref}, c). In step three, it is then warped to the respiratory destination phase (r, c). This deformation scheme requires cardiac motion estimation to be performed only at the respiratory reference phase while enabling MoCo image reconstruction of any arbitrary combination of respiratory and cardiac motion phase employing 100% of the measured raw data.

3.1.5 Implementation

All algorithms were implemented in the programming language C++ and reconstructions were performed on a two-socket Intel Xeon E5–2697v3 with a total of 28 cores at 2.60 GHz and 256 GB of memory. For the nonoptimized code, joint motion estimation and image reconstruction of 20 respiratory phases required computation times of about 4.0 h applying the 4D joint MoCo-HDTV algorithm. Accordingly, computational effort for generation of respiratory MoCo raw data and for reconstruction of 12 cardiac phases was about 3.0 h. Reconstruction time of 5D respiratory and cardiac MoCo reconstructions of 240 combinations of respiratory and cardiac phases was about 2.0 h for nonoptimized code.

3.2 PET Image Reconstruction Algorithms

3.2.1 Standard OSEM

Reconstructions of 3D motion average, 4D respiratory gated and 5D respiratory and cardiac gated PET images were performed with a 3D OSEM algorithm (Hudson and Larkin, 1994). This algorithm represents a modification of the expectation maximization algorithm derived in section 2.2.4. The OSEM update equation of the image estimate $\boldsymbol{\lambda}^{(n+1)}$ at subiteration $n+1$ is given as follows:

$$\boldsymbol{\lambda}^{(n+1)} = \boldsymbol{\lambda}^{(n)} \frac{1}{M_\kappa^{\mathrm{T}}(\frac{1}{\boldsymbol{a}\boldsymbol{n}})} M_\kappa^{\mathrm{T}} \frac{\boldsymbol{p}}{(M_\kappa \boldsymbol{\lambda}^{(n)}) + \boldsymbol{a}(\boldsymbol{d}\boldsymbol{n} + \boldsymbol{s})}. \tag{3.16}$$

The parameter κ denotes the subset index and for a total number of subsets K, it is defined as $\kappa = n \mod K$, i. e. execution of K subiterations yields a full iteration. The operators M_κ and M_κ^{T} represent the system matrix and its transpose, respectively, including forward and backprojections along the LORs of subset κ. The vector $\boldsymbol{p}$ contains the measured PET raw data. Further variables are the randoms $\boldsymbol{d}$, attenuation correction factors $\boldsymbol{a}$ and scatter $\boldsymbol{s}$. Note that all vector operations in Eq. (3.16) represent element-wise operations. For gated reconstruction schemes, raw data from each motion phase were reconstructed separately. All PET images were reconstructed with 3 iterations, 21 subsets and the specified FOV covered a volume of $534 \times 534 \times 258\,\mathrm{mm}^3$ with a voxel size of $2.1 \times 2.1 \times 2.0\,\mathrm{mm}^3$. At the end of each iteration, a 3D Gaussian smoothing filter with a full width at half maximum (FWHM) of 3.2 mm was applied to the image volume to reduce statistical noise in the image.

3.2.2 Motion-Compensated OSEM

For 4D respiratory MoCo PET and 5D respiratory and cardiac MoCo PET reconstructions, the OSEM algorithm from Eq. (3.16) was extended incorporating MVFs into the system matrix (Li et al., 2006; Qiao et al., 2006) as shown in Fig. 3.6. In mathematical notation, the MoCo OSEM update equation of the image estimate $\boldsymbol{\lambda}_{r,c}^{(n+1)}$ at subiteration $n+1$ for the combination of respiratory and cardiac motion phase (r, c) is defined as:

$$\boldsymbol{\lambda}_{r,c}^{(n+1)} = \boldsymbol{\lambda}_{r,c}^{(n)} \frac{1}{N_c \sum_{r'} D_{r',c'}^{r,c} M_\kappa^{\mathrm{T}} (\frac{1}{\boldsymbol{a}_{r'} \boldsymbol{n}})} \sum_{r',c'} D_{r',c'}^{r,c} M_\kappa^{\mathrm{T}} \frac{G_{r'} G_{c'}\, \boldsymbol{p}}{(M_\kappa D_{r,c}^{r',c'} \boldsymbol{\lambda}_{r,c}^{(n)} + \boldsymbol{a}_{r'}(\boldsymbol{d}\,\boldsymbol{n} + \boldsymbol{s})}. \tag{3.17}$$

The definition of variables and operators corresponds to Eq. (3.16). However, the attenuation correction factors $\boldsymbol{a}_r$ are respiratory motion phase–dependent. The gating operators $G_{r'}$ and $G_{c'}$ are applied in accordance to Eq. (3.2) nulling the contribution of raw data not belonging to the current combination of respiratory and cardiac phase (r', c'). While N_c denotes the number of cardiac motion phases, the operator $D_{r',c'}^{r,c}$ describes a warping operation mapping the volume of motion phase (r', c') to (r, c) applying the dedicated MVFs. It can be constructed using Eq. (3.9) for respiratory motion only or Eq. (3.15) for both the respiratory and cardiac dimension. The same image reconstruction parameters as used for the standard OSEM reconstruction were employed.

3.2.3 4D Respiratory Motion-Compensated PET from Literature

For comparison purposes, the motion estimation approach proposed in Würslin et al. (2013), Fayad et al. (2015b), Fürst et al. (2015) and Grimm et al. (2015) was implemented. In these studies, respiratory time-resolved 4D gated MR images were used for registration. In contrast to the cyclic registration described above, these studies estimated MVFs between each combination of motion phases t and t' as shown in Fig. 3.3 a. In this work, the same image registration algorithm with identical parameter settings as used for 4D joint MoCo-HDTV was employed. To obtain 4D gated MR images, a gridding reconstruction of the radially acquired MR raw data was performed (Eq. (3.2)). For MoCo PET reconstruction, the approach described in section 3.2.2 was used. Implying that a standard motion estimation method was employed, resulting MoCo PET images are referred to as 4D motion-compensated PET based on standard motion estimation (sMoCo PET).

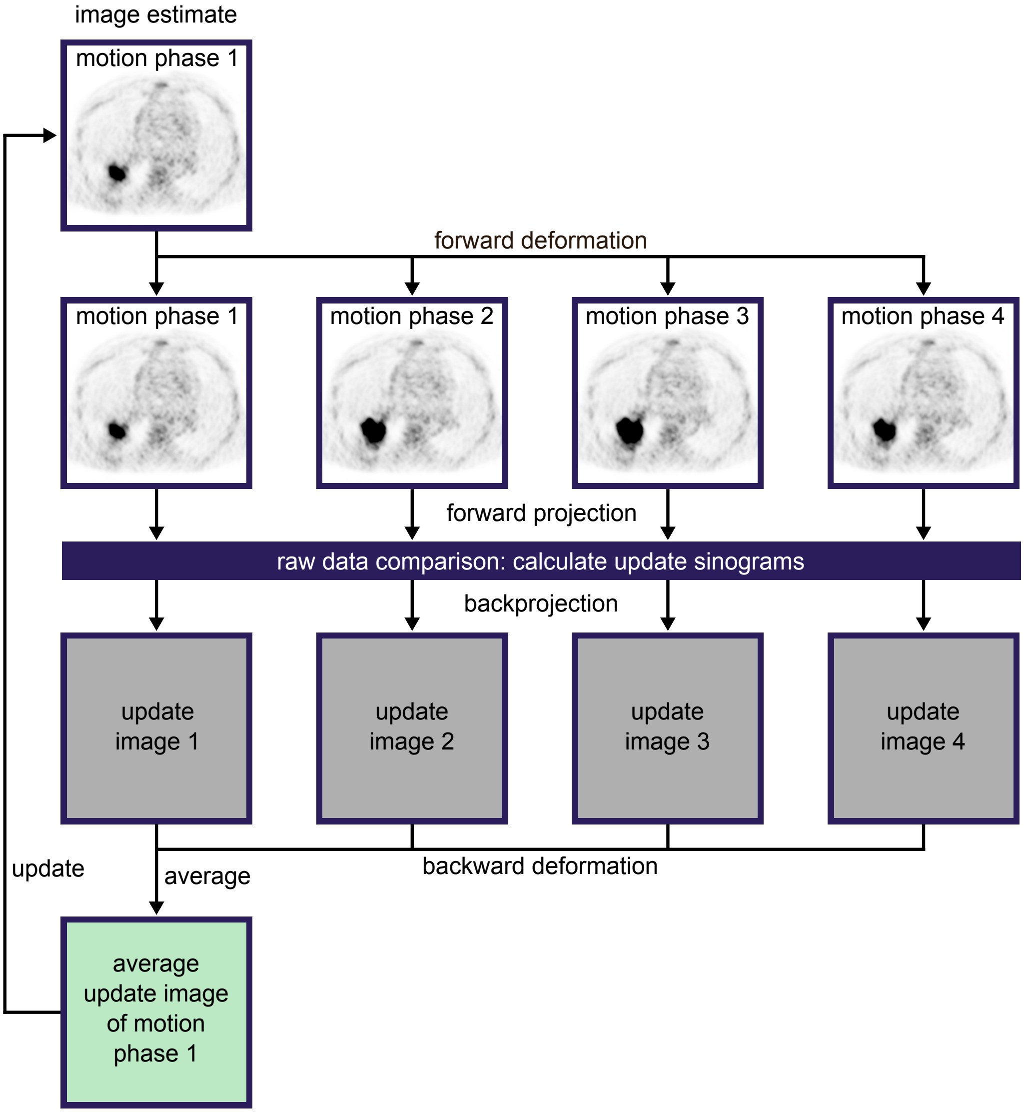

Figure 3.6: Schematic overview of MoCo PET reconstruction (Li et al., 2006; Qiao et al., 2006). The image estimate of a desired motion phase (r, c) is deformed to all other motion phases, forward projected and compared to the raw data of these phases. This comparison yields update sinograms, which are backprojected. The resulting update images are deformed back to the desired motion phase and the average is used for updating the image estimate. This process is repeated for several iterations.

3.2.4 Implementation

Similar to the MR reconstruction, all algorithms were implemented in C++. Using the same workstation as described in section 3.1.5, the nonoptimized code required about 15 min per respiratory motion phase in case of 4D respiratory MoCo PET reconstruction with 20 motion phases. For 5D respiratory and cardiac MoCo PET with 240 combinations of respiratory and cardiac phases (r, c) in total, the reconstruction time of a volume from a single combination was about 40 min for nonoptimized code.

3.3 Generation of MR and PET Data

3.3.1 Radial Stack-of-Stars Sampling Scheme

In this work, a radial stack-of-stars sampling of k-space (Vigen et al., 2000; Larson et al., 2002) was employed for all simulations and measurements. The sampling scheme is illustrated in Fig. 3.7. It combines radial sampling in the readout plane with Cartesian sampling in slice direction. The angular increment between adjacent radial spokes corresponded to the golden angle of approximately 111.25° as was proposed by Winkelmann et al. (2007) for radial MRI. First all slices corresponding to one radial angle were sampled sequentially before moving to the next angle. This sampling scheme leads to approximately uniform coverage of the radial plane in retrospectively gated reconstructions (Lin et al., 2008; Buerger and Clough, 2012). In addition, radial sampling improves the robustness against motion during data acquisition as the k-space center is sampled during each readout (Glover and Pauly, 1992; Block et al., 2014). As a further advantage, the k-space center signal can be employed for intrinsic MR gating as explained in section 3.4.1 (Larson et al., 2005; Grimm et al., 2015).

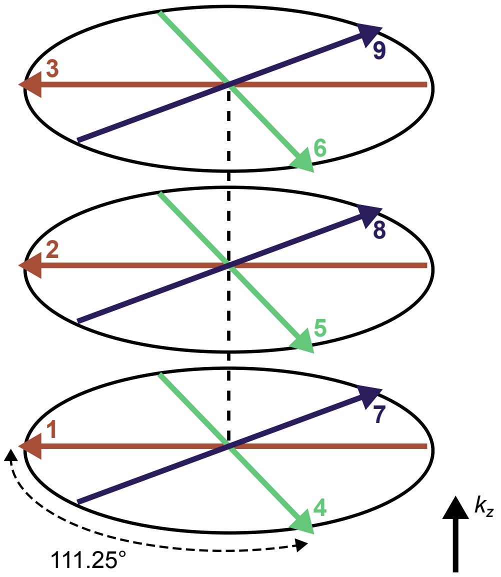

Figure 3.7: Radial stack-of-stars sampling scheme: The readout plane is sampled in a radial manner while Cartesian slice encoding is employed. The angular spacing between adjacent spokes is defined by the golden angle of approximately 111.25°. First all slices of one radial angle are sampled sequentially before moving to the next angle as indicated by the numbers in the illustration.

3.3.2 Simulation of MR Data

A PET/MR acquisition of the free-breathing thorax was simulated to have a ground truth available for comparison purposes (Fig. 3.8). To create a 4D MR motion phantom, artificially generated deformation vector fields were applied to a static 3D MR thorax volume of a patient. Motion in head–feet and anterior–posterior direction was considered for the simulation setting the maximal motion magnitude of structures at the diaphragm to approximately 20 mm. For this motion phantom, 100 different respiratory motion states were generated.

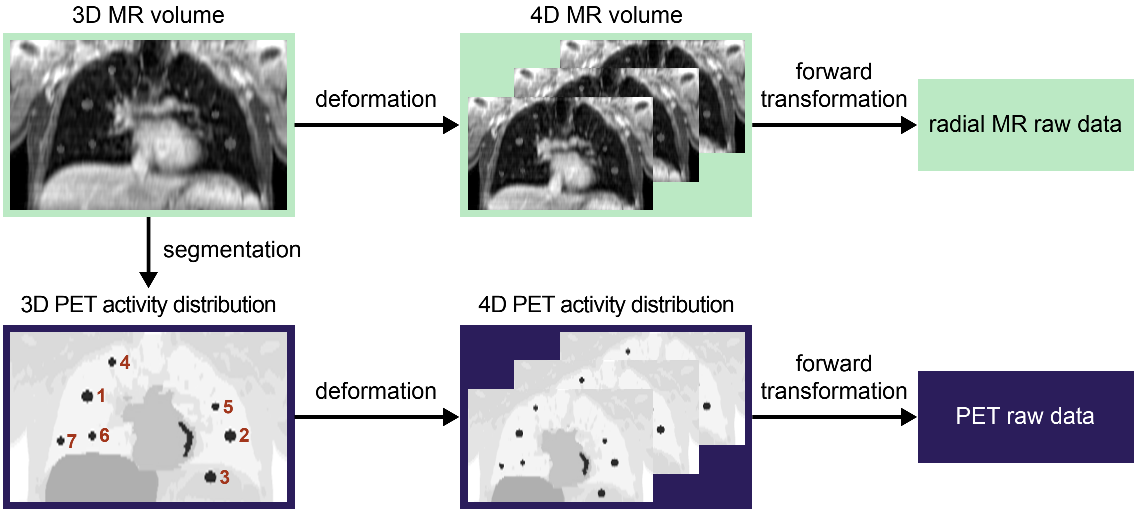

Figure 3.8: Overview of PET/MR simulation: For MR simulation, artificially-generated deformation vector fields are applied to a static 3D MR volume of a patient to create a 4D MR motion phantom. Radial MR raw data are obtained by forward transformation of this motion phantom. For PET simulation, a 3D activity distribution is constructed by segmenting the static MR volume and deformation identical to the MR simulation is applied. The resulting 4D activity distribution is forward projected to gain the PET raw data.

To simulate a realistic MR measurement during free breathing, the temporal evolution of a sinusoidal respiratory motion curve with varying breathing periods (3.50 s ± 0.50 s) and varying breathing amplitude (100% ± 3%) was incorporated into the simulation. Depending on the chosen number of spokes and the specified temporal sampling distance, any arbitrary acquisition time could be simulated. Moving along the motion curve with this specified sampling distance, one of the 100 generated volumes was assigned to each simulated k-space line according to the breathing amplitude at that time point.

To create MR raw data, the selected volume was forward transformed to k-space applying a Cartesian FFT and the simulated k-space line was sampled at its desired location. In this work, a 3D-encoded radial stack-of-stars sampling scheme with golden angle radial spacing as described in section 3.3.1 was employed. Thus MR raw data values at radial spoke positions were computed by bilinear interpolation in k-space. Gaussian noise individually calculated for real and imaginary parts was added to the simulated MR data. For gated reconstructions, the respiratory motion curve used for simulation was employed as input and data were sorted into $N_r = 20$ overlapping respiratory motion phase bins with a width of 10.0% in accordance to section 3.4.1.

3.3.3 Simulation of PET Data

As proposed by Tsoumpas et al. (2011), a 3D PET activity distribution was created by segmentation of the 3D MR volume employed for the MR simulation (Fig. 3.8). Seven spherical lesions with a radius of 8 and 12 mm were inserted in the lungs and upper abdomen. Table 3.1 summarizes the activity values assigned to the different tissue classes. To create a 4D activity distribution, respiratory motion was modeled in accordance to the 4D MR motion phantom.

tissue class	activity / (kBq/mL)
lungs	1.0
soft tissue	3.0
liver	7.5
heart	5.5
myocardium	20.0
lesions	20.0

Table 3.1: Activity values assigned to the 3D PET activity distribution used for simulation.

PET raw data were generated in correspondence to Heußer et al. (2016) by forward projecting the volume of each motion phase. For scatter simulation, the noiseless emission sinograms were smoothed in all spatial dimensions applying a Gaussian filter. Emission data and simulated scatter were combined assuming a scatter fraction of 50% and Poisson noise was added. For simplification, effects of tissue attenuation were excluded from the PET simulation. To account for the noisy data, ten independent noise realizations each having 60×10^6 counts in total were simulated. The PET detector geometry used for simulation corresponded to the geometry of the Biograph mMR system (Delso et al., 2011) (Siemens Healthineers, Erlangen, Germany). For generation of a 4D ground truth PET, reference raw data were simulated in such a way that each reference motion phase was composed of approximately 60×10^6 counts yielding noise levels comparable to 3D motion average PET reconstructions.

3.3.4 Acquisition of MR Data

To demonstrate the application of the different MR reconstruction algorithms, MR data of three healthy volunteers (2 female, 1 male, aged 26 to 29 years) and thirteen patients

(7 female, 6 male, aged 42 to 79 years) with fibrosing lung disease were acquired during free breathing. Data acquisition and evaluation was in accordance with the declaration of Helsinki (World Medical Association, 2013) including study approval by the local ethics committee and informed consent was obtained from each patient. Table 3.2 lists the individual subjects and their assignment to the different studies conducted in this work. MR data were acquired at a 1.5 T MR scanner (Magnetom Aera, Siemens Healthineers, Erlangen, Germany, Fig. 3.9 a). A vendor-provided 3D-encoded T_1-weighted prototype gradient echo sequence was employed. This sequence type generates a gradient echo by applying a pair of bipolar gradients in contrast to spin echo sequences, which use a 180° RF pulse for refocusing the signal. For sampling k-space, a radial stack-of-stars scheme with golden angle radial spacing as described in section 3.3.1 was used. The base resolution in the radial plane was set to 256 px, which yields the Nyquist sampling criterion for radial MR acquisitions of $256 \times \pi/2 \approx 402$. To reduce aliasing artifacts, the readout plane was oversampled by a factor of two, i. e. 512 sampling points were measured along each spoke. Volunteer data were acquired in coronal orientation to fully cover the thorax requiring as few slice encoding steps as possible. Note that acquisition of patient data was not for the purpose of this work, but for clinical analysis of respiratory motion patterns. Thus, data acquisition was oriented in sagittal view with the intention of capturing the primary motion directions in the readout plane. Table 3.3 gives an overview of further acquisition parameters.

(a) 1.5 T MR scanner (Magnetom Aera) **(b)** 3.0 T PET/MR scanner (Biograph mMR)

Figure 3.9: MR and fully-integrated PET/MR scanners employed for patient measurements in this work (Siemens Healthineers, Erlangen, Germany)[1].

---

[1] The images were adopted from `https://www.healthcare.siemens.de/magnetic-resonance-imaging/0-35-to-1-5t-mri-scanner/magnetom-aera`, `https://www.healthcare.siemens.de/magnetic-resonance-imaging/mr-pet-scanner/biograph-mmr` on August 10, 2016.

3.3.5 Acquisition of PET/MR Data

To assess the performance of MoCo PET reconstruction algorithms, simultaneous PET/MR data of six patients (2 female and 4 male, aged 32 to 81 years) with diagnosed bronchial carcinoma were acquired during free breathing at a 3 T PET/MR system (Delso et al., 2011) (Biograph mMR, Siemens Healthineers, Erlangen, Germany, Fig. 3.9 b). Data acquisition and evaluation was in accordance with the local ethics committee and informed consent was obtained from each patient. The individual subjects are listed in Table 3.2. For MR imaging, a similar prototype MR sequence with radial stack-of-stars sampling in the sagittal plane and a base resolution of 256 px as explained in section 3.3.4 was applied. The acquisition parameters are shown in Table 3.3. For PET imaging, the radionuclide agent ^{18}F-FDG was employed. Injected activities were (209 ± 19) MBq and the tracer was administered (141 ± 14) min prior to data acquisition.

subject ID	gender	age / years	scanner model	4D MRI study	4D PET study	5D MRI study	5D PET study
volunteer data (MR)							
v01	female	27	Magnetom Aera	×	–	–	–
v02	male	26	Magnetom Aera	×	–	–	–
v03	female	29	Magnetom Aera	×	–	–	–
patient data (MR)							
p01	female	60	Magnetom Aera	×	–	–[b]	–
p02	male	43	Magnetom Aera	×	–	–[b]	–
p03	female	45	Magnetom Aera	×	–	×	–
p04	male	76	Magnetom Aera	×	–	×	–
p05	female	78	Magnetom Aera	×	–	×	–
p06	female	58	Magnetom Aera	×	–	×	–
p07	female	78	Magnetom Aera	×	–	×	–
p08	female	73	Magnetom Aera	×	–	×	–
p09	male	72	Magnetom Aera	×	–	×	–
p10	male	73	Magnetom Aera	–[a]	–	×	–
p11	male	64	Magnetom Aera	–[a]	–	×	–
p12	female	79	Magnetom Aera	–[a]	–	×	–
p13	male	71	Magnetom Aera	–[a]	–	×	–
patient data (PET/MR)							
s01	male	57	Biograph mMR	–	×	–	–[b]
s02	female	56	Biograph mMR	–	×	–	×
s03	male	32	Biograph mMR	–	×	–	×
s04	female	48	Biograph mMR	–	×	–	×
s05	male	75	Biograph mMR	–	×	–	–[b]
s06	male	81	Biograph mMR	–	×	–	×

[a] Data set was not available at the time the 4D MRI study was conducted
[b] Derivation of cardiac self-gating signal failed

Table 3.2: List of acquired volunteer and patient data sets and assignment to the different studies that were conducted in this work and that are described in section 3.5.

parameter	simulation	volunteer data (MR)	patient data (MR)	patient data (PET/MR)
scanner model	–	Magnetom Aera	Magnetom Aera	Biograph mMR
number of subjects	1	3 (v01 to v03)	13 (p01 to p13)	6 (s01 to s06)
body region	thorax	thorax and upper abdomen	thorax and upper abdomen	thorax
contrast-enhanced	–	no	yes	no
orientation of radial plane	transversal	coronal	sagittal	sagittal
sampling points per readout	512	512 (2×oversampling)	512 (2×oversampling)	512 (2×oversampling)
number of partitions	80	48 to 52	80 (interpolated)	88 (interpolated)
partial Fourier encoding (slices)	7/8	no	6/8	6/8
slice resolution	100%	100%	60%	55%
slice oversampling	0%	0%	33%	0%
active receiving coil channels	1	32 to 34	30 to 34	7 to 20
total acquisition time	20 to 60 s	4 min 4 s to 6 min 51 s	5 min	5 min 50 s
field of view	$400 \times 400 \times 188\,\text{mm}^3$	$400 \times 400 \times 192$ to $208\,\text{mm}^3$	$385 \times 385 \times 300\,\text{mm}^3$	$400 \times 400 \times 396\,\text{mm}^3$
voxel size	$0.8 \times 0.8 \times 2.4\,\text{mm}^3$	$1.6 \times 1.6 \times 4.0\,\text{mm}^3$	$1.5 \times 1.5 \times 5.0\,\text{mm}^3$	$1.6 \times 1.6 \times 4.5\,\text{mm}^3$
echo time TE	–	1.23 ms	1.69 ms	1.70 ms
repetition time TR	–	2.48 ms	3.77 ms	3.75 ms
effective temporal resolution	–	153 to 162 ms	172 ms	162 ms
flip angle	–	12°	12°	10°
fat suppression	–	yes	yes	yes

Table 3.3: Parameters of MR simulation and MR data acquisitions.

3.4 Preprocessing of Acquired MR and PET Data

This section describes methods applied to the acquired MR and PET data as preprocessing steps before image reconstruction is performed. An overview of the complete PET/MR MoCo reconstruction framework developed in this work, which illustrates the connections between the individual components, is shown in Fig. 3.10.

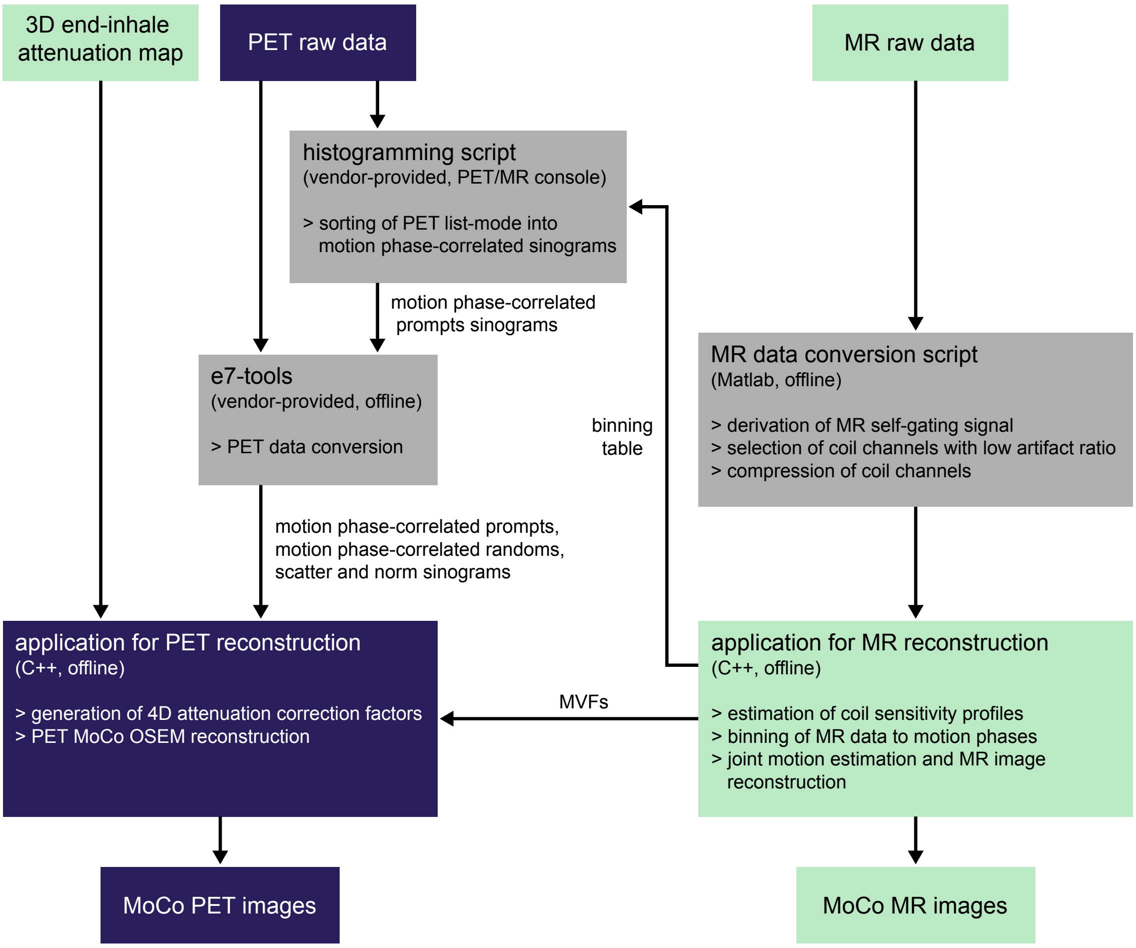

Figure 3.10: Overview of the PET/MR MoCo reconstruction framework developed in this work. For MR image reconstruction, proprietary MR raw data are converted and preprocessed employing a Matlab (The Mathworks, Inc., Natick, USA) script. Subsequently, joint motion estimation and MR image reconstruction of processed data can be performed. For PET reconstruction, a binning table generated during the MR reconstruction is employed for histogramming of proprietary PET list-mode data. Motion phase–correlated sinograms and data correction sinograms are extracted using the e7-tools for offline reconstruction. Applying the MVFs derived from MR, MoCo PET images can be reconstructed.

3.4.1 MR Self-Gating

The signal used for intrinsic MR gating was obtained from the magnitude of the k-space data averaged over the nine central points for each acquired spoke. The data were corrected for an angle-dependence of the signal baseline in accordance to Grimm et al. (2011). The corrected data were sorted into a matrix Ω such that the rows of Ω corresponded to the different acquisition angles and the columns of Ω represented data from different partitions and coil channels. As the different coil channels and partitions contain varying amounts of information on the motion signal, a principal component analysis of Ω was performed to obtain the self-gating signal as the principal eigenvector of the covariance matrix of Ω. To correct for baseline drifts of the self-gating signal, e. g. due to contrast agent dynamics, a cubic spline interpolation between the points of maximal exhalation was calculated to estimate the correction signal. To distinguish between respiratory and cardiac self-gating signals, a bandpass filter was applied before the principal component analysis was carried out. Filter ranges of 0.1 to 0.5 Hz and 0.5 to 2.0 Hz were used for respiratory and cardiac motion, respectively. Examples of the resulting signals are shown in Fig. 3.11.

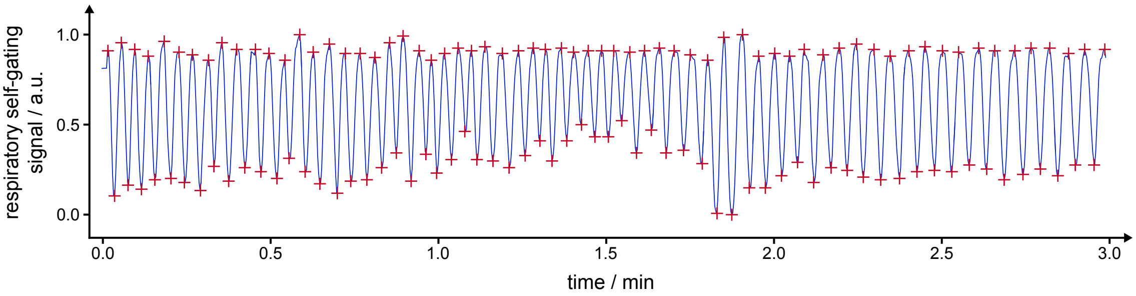

(a) respiratory self-gating signal

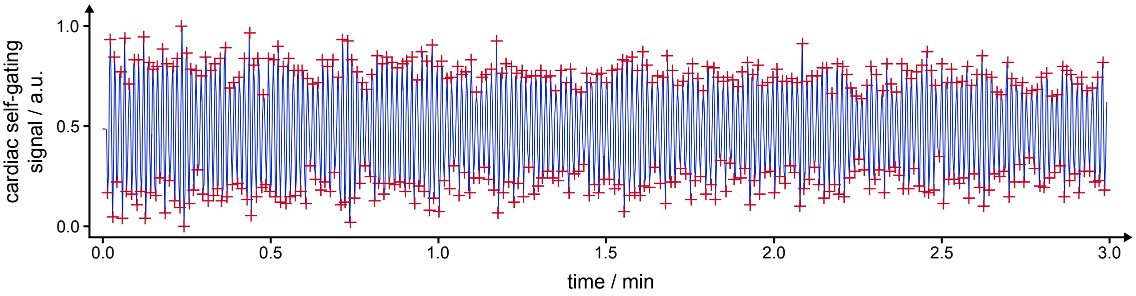

(b) cardiac self-gating signal

Figure 3.11: Examples of MR self-gating signals obtained from the magnitude of k-space center values for a patient with fibrosing lung disease. For the respiratory signal, the upper and lower peaks can be interpreted as the relative breathing amplitudes at end-exhale and end-inhale, respectively. For the cardiac signal, the distance between upper or lower peaks is used to obtain the cardiac motion phase.

Employing the self-gating signals, the respiratory and cardiac gating operators G_r and G_c were constructed. These operators act as raw data masks and remove entries not belonging to the current respiratory phase r or cardiac phase c from the raw data. For all studies conducted in this work, G_r and G_c were defined in such a way that MR and PET raw data were assigned to $N_r = 20$ overlapping respiratory motion phase bins with a width of 10.0% and $N_c = 12$ overlapping cardiac bins with a width of 16.7%. Each bin represented a specific motion state averaged over several motion cycles. For respiratory gating, inhalation and exhalation was distinguished accounting for hysteresis effects, i. e. intracycle breathing variations were considered (McClelland et al., 2013). The sorting of data was based on the respiratory amplitude. The amplitude range was chosen individually for each respiratory bin to ensure that each bin contained 10.0% of the data. For cardiac gating, the cardiac phase defined by the lower and upper peaks of the cardiac self-gating signal was used for sorting of data. Assuming normal heart rates of about 60 beats per minute, the number of $N_c = 12$ cardiac phases with a width of 16.7% was chosen to match the effective temporal resolution of the MR data acquisition of about 160 to 170 ms.

3.4.2 MR Raw Data Preprocessing

Selection of Coil Channels With Low Artifact Ratio

To reduce streak artifacts in the reconstructed images, data from coil channels with high artifact ratios were discarded and thus excluded from the reconstruction as proposed in Grimm et al. (2013). For each coil channel j, a streak artifact ratio R_j^S was calculated:

$$R_j^S = \frac{\|\boldsymbol{h}_j\|_2}{\|\boldsymbol{l}_j\|_2}. \tag{3.18}$$

The vectors $\boldsymbol{l}_j$ and $\boldsymbol{h}_j$ correspond to low and high frequency components of the measured raw data $\boldsymbol{p}$ of coil channel j. To obtain the low and high frequency components, the N data points of each spoke were weighted with a Hann window W^{H} and with $(1 - W^{\mathrm{H}})$, respectively:

$$W^{\mathrm{H}}(n) = 0.5\left(1 - \cos\left(\frac{2\,\pi\,n}{N-1}\right)\right). \tag{3.19}$$

A k-means clustering with two classes was applied to the calculated values R_j^S to assign the J coil channels to classes with either low or high streak artifact level. The J_l channels with low streak artifact levels, i. e. low values R_j^S, were employed for image reconstruction while the channels with high artifact levels were discarded.

Compression of Coil Channels

To reduce computational effort, coil channels were compressed by creating new virtual coil channels in a lower-dimensional subspace of the original data. Coil data were sorted into a matrix B, such that the rows of B contained the data of each coil channel j and the columns of B represented the J_l different coil channels. This matrix B can be represented by a singular value decomposition:

$$B = U\,\Sigma\,V^{\mathrm{T}}. \tag{3.20}$$

The columns of the unitary matrices U and V are called the left and right singular vectors, respectively. The diagonal matrix Σ contains the singular values $\tilde{\sigma}_j$ in nonincreasing order with $j = 1, \ldots, J_l$. As the right singular vectors represent an orthonormal basis for the rows of B, each row of B can be written as a linear combination of these vectors. Utilizing this property, virtual coil channels B_L in a lower-dimensional space can be generated by projecting B onto a subspace spanned by the first $L \leq J_l$ singular vectors:

$$B_L = B\,V_L. \tag{3.21}$$

As the total energy of the matrix B is defined as the sum of squares of its singular values, an energy ratio $R^E(L)$ between the truncated virtual coil data B_L and the full-rank original coil data B can be calculated as follows:

$$R^E(L) = \frac{\sum_{l=1}^{L} \tilde{\sigma}_l}{\sum_{j=1}^{J_l} \tilde{\sigma}_j}. \tag{3.22}$$

This energy ratio can be interpreted as a measure of the information content of the new virtual coil channels relative to the original coils. In this work, L was chosen in such a way that $R^E(L) \geq 0.96$, i. e. at least 96% of the information of the original coil channels was kept. In this way, the number of coil channels was reduced approximately by a factor of two depending on the data set.

Estimation and Combination of Coil Channels

The complex-valued coil sensitivity profiles $\boldsymbol{b}_j$ of coil channels j were estimated on basis of low-resolution 3D reconstructions of the measured raw data as proposed in Bydder et al. (2002):

$$\boldsymbol{b}_j = \frac{\mathsf{X}^{\dagger} W^{\mathrm{H}}\,\boldsymbol{p}_j}{\sqrt{\sum_k (\mathsf{X}^{\dagger} W^{\mathrm{H}}\,\boldsymbol{p}_k)^2}}. \tag{3.23}$$

The operator W^{H} represents a Hann window as defined in Eq. (3.19) selecting the low frequency components of the measured raw data $\boldsymbol{p}_{j,k}$ of coil channels j, k.

For combination of different coil channels during the reconstruction, a method similar to the real-SUPER approach proposed in Bydder et al. (2002) was used. The combination is described by the operator $S^{\dagger}$ in the equations of this work. The real-valued composite image $\boldsymbol{f}$ is then obtained using the coil sensitivity profiles $\boldsymbol{b}_j$ from Eq. (3.23) as follows:

$$\boldsymbol{f} = S^{\dagger}\mathsf{X}^{\dagger}\boldsymbol{p} = \mathrm{Re}\left(\frac{\sum_j (\mathsf{X}^{\dagger}\boldsymbol{p}_j)\,\boldsymbol{b}_j^*}{\sum_k \boldsymbol{b}_k^2}\right). \tag{3.24}$$

Generation of Highly-Undersampled Raw Data

To create MR raw data sets with high undersampling, only a subset of the acquired raw data sets was used for reconstruction. For this purpose, the first N_{spokes} consecutively measured spoke angles were kept and all further spoke angles were discarded. This procedure allowed for retrospective generation of highly undersampled raw data sets with arbitrary acquisition times being equal to measurements, which stop after the acquisition of N_{spokes} radial spokes. In this work, the number of spoke angles N_{spokes} varied between the different studies and is described in more detail in section 3.5 below.

3.4.3 PET Raw Data Preprocessing

Histogramming of PET List-Mode Data

Prior to the PET image reconstruction, PET list-mode data acquired at the scanner were sorted into sinograms of different motion phases applying a vendor-provided histogramming script. This script was carried out at the console of the PET/MR scanner synchronizing the clocks of PET and MR computers. For sorting, a motion phase binning table defined by the intrinsic MR gating was used.

Extraction of Normalization and Attenuation Factors, Scatter, and Randoms

For estimation of scatter and the extraction of normalization and randoms sinograms, the vendor-provided e7-tools for offline reconstruction were employed. For attenuation correction, the standard attenuation map available at the scanner was used. It was based on a two-point Dixon method (Martinez-Möller et al., 2009), which segments an acquired MR image into four tissue classes, in particular into soft tissue, fat, lung tissue and air. As the standard attenuation map was acquired in breath-hold end-exhale, MVFs derived from MR were applied to deform this map to all other respiratory motion phases to create a 4D attenuation map. This respiratory time-resolved attenuation map was employed for all MoCo PET reconstructions while the static attenuation map was used for 3D and 4D gated PET reconstructions, for which no MVFs are available in practice. To generate attenuation correction factors, the selected attenuation map was forward projected along all LORs.

3.5 Overview of Studies

3.5.1 4D Respiratory Time-Resolved MRI

The 4D MRI study aimed at investigating the performance of the 4D joint MoCo-HDTV algorithm developed in this work for 4D respiratory time-resolved MR image reconstruction of highly undersampled data in comparison to other methods from the literature. This evaluation of reconstruction algorithms comprised simulated data and acquired data of three volunteers (v1 to v3) and nine patients (p1 to p9) of the thorax and upper abdomen. A list of the individual subjects is given in Table 3.2. Employing the MR simulation described in section 3.3.2, highly undersampled MR data for acquisition times of 20, 40 and 60 s were simulated corresponding to 12, 24 and 36 spokes per slice and motion phase. For the acquired volunteer and patient data, highly undersampled data sets consisting of 24 spokes per slice and motion phase were generated for all twelve subjects as described in section 3.4.2. These data sets corresponded to acquisition times of 37 to 41 s and radial undersampling factors of 16.8. As shown in Fig. 3.12, the following reconstructions were performed for the highly undersampled data sets of simulated and acquired data: 3D motion average and 4D gated reconstructions serving as standard methods (section 3.1.1), 4D MASTeR and 4D HDTV representing state-of-the-art methods from literature (section 3.1.3) and 4D joint MoCo-HDTV reconstructions as proposed in this work (section 3.1.2). In addition, 4D gated images of the reference raw data sets were reconstructed for the acquired data employing all available data from acquisition times of 4 to 7 min. Equal parameter settings were used for all reconstructions.

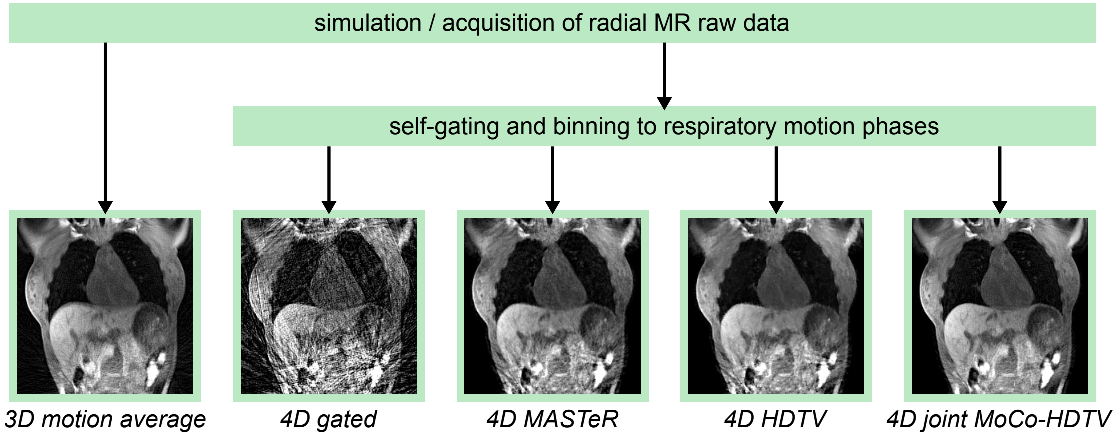

Figure 3.12: Overview of 4D MRI study: Radial MR data of the free-breathing thorax are either simulated or acquired. After self-gating, MR data are sorted into different respiratory motion phases and several MR image reconstructions are performed.

Assessment of Image Quality

To quantify the performance of the different algorithms described above, reconstruction results for the highly undersampled raw data sets were compared. For this comparison, the 4D ground truth was used in case of simulated data while for acquired data, 4D gated reconstructions of the reference raw data sets were employed. The 4D gated reconstructions were selected as reference, since they represent the clinical standard today and provide high temporal fidelity employing no temporal regularization during reconstruction. Different image similarity metrics between the reconstructed images $\boldsymbol{f}$ and reference or ground truth images $\boldsymbol{g}$ were calculated. A well-known and simple metric is the mean squared error (MSE), which represents a voxel-wise comparison of image intensities:

$$\mathrm{MSE}(\boldsymbol{f},\boldsymbol{g}) = \frac{1}{N}\sum_{i=0}^{N-1}(f_i - g_i)^2, \tag{3.25}$$

with the voxel index i and the total number of voxels N. For the acquired data, the reference images contained slight streak artifacts and the voxel-specific metric MSE was therefore excluded from evaluation as it may be biased by these artifacts.

To account for the human visual perception, which is adapted for the extraction of structural information from an image, Wang et al. (2004) introduced the structural similarity (SSIM) metric. This measure compares luminance, contrast and structure of two images and can be calculated as follows:

$$\mathrm{SSIM}(\boldsymbol{f},\boldsymbol{g}) = \frac{1}{N}\sum_{i=0}^{N-1}\frac{(2\,\bar{\mu}_{f_i}\bar{\mu}_{g_i} + c_1)\,(2\,\bar{\sigma}_{f_i g_i} + c_2)}{(\bar{\mu}_{f_i}^2 + \bar{\mu}_{g_i}^2 + c_1)\,(\bar{\sigma}_{f_i}^2 + \bar{\sigma}_{g_i}^2 + c_2)}. \tag{3.26}$$

The contribution of each voxel i is evaluated within a two-dimensional patch of $9 \times 9\,\mathrm{px}^2$. While $\bar{\mu}_{f_i}$ and $\bar{\mu}_{g_i}$ describe mean values of these patches for the voxels f_i and g_i, respectively, $\bar{\sigma}_{f_i}^2$ and $\bar{\sigma}_{g_i}^2$ represent corresponding variances. The covariance between the patches of f_i and g_i is given by $\bar{\sigma}_{f_i g_i}$. The two variables $c_1 = (k_1 L_\mathrm{D}^2)$ and $c_2 = (k_2 L_\mathrm{D}^2)$ stabilize the division. They are calculated from the dynamic range L_D defined by the difference of maximum and minimum intensity of the images and from the parameters $k_1 = 0.01$ and $k_2 = 0.03$ chosen in accordance to Wang et al. (2004).

Furthermore, the normalized cross-correlation (NCC) of $\boldsymbol{f}$ and $\boldsymbol{g}$, which is commonly used in image registration, was computed:

$$\mathrm{NCC}(\boldsymbol{f},\boldsymbol{g}) = \frac{1}{N}\sum_{i=0}^{N-1}\frac{(f_i - \bar{\mu}_f)\,(g_i - \bar{\mu}_g)}{\bar{\sigma}_f\,\bar{\sigma}_g}. \tag{3.27}$$

The parameters $\bar{\mu}_f$ and $\bar{\mu}_g$ correspond to mean values of the images and $\bar{\sigma}_f$ and $\bar{\sigma}_g$ denote standard deviations, respectively.

Besides the intensity-based metrics MSE, SSIM and NCC, the normalized mutual information (NMI) was evaluated as a statistical metric for image similarity (Collignon et al., 1995; Viola and Wells, W. M., 1995; Wells et al., 1996). The NMI can be interpreted as a measure of the information content both images $\boldsymbol{f}$ and $\boldsymbol{g}$ contain mutually. It is closely connected to the Shannon entropy (Shannon, 1948):

$$H(\boldsymbol{f}) = H_b = -\sum_b P_b \log(P_b). \tag{3.28}$$

The variable P_b defines the probability that the intensity of a voxel matches the intensity range of bin b. In this work, 32 bins with equal width were employed for evaluation. Using P_{b_1,b_2} as the joint probability that voxels of the images $\boldsymbol{f}$ and $\boldsymbol{g}$ correspond to bin b_1 and bin b_2, respectively, joint entropy of two images is defined accordingly:

$$H(\boldsymbol{f},\boldsymbol{g}) = H_{b_1,b_2} = -\sum_{b_1}\sum_{b_2} P_{b_1,b_2} \log(P_{b_1,b_2}). \tag{3.29}$$

Employing the definitions of Eq. (3.28) and Eq. (3.29), the NMI can be expressed by:

$$\mathrm{NMI}(\boldsymbol{f},\boldsymbol{g}) = \frac{H(\boldsymbol{f}) + H(\boldsymbol{g}) - H(\boldsymbol{f},\boldsymbol{g})}{H(\boldsymbol{f},\boldsymbol{g})}. \tag{3.30}$$

In addition to the calculation of quantitative image similarity metrics, reconstructed images of the acquired data were evaluated independently by two radiologists. Both had at least five years of experience in thoracic and abdominal MR imaging. 4D gated images of the highly undersampled raw data sets were excluded from this evaluation due to their severe streak artifact levels. To assess different motion phases, the end-exhale phase and a mid-ventilation phase were selected. The evaluation was blinded, i. e. type and order of reconstruction algorithms were unknown to the radiologists. Using the five-point Likert scale, each image was rated using the following overall score levels: 1 (nondiagnostic), 2 (poor), 3 (adequate), 4 (good), and 5 (excellent). The first criterion for image quality was overall image sharpness, e. g. sharpness of the edge of the diaphragm, the lung and liver parenchyma and the spine, and identification and sharpness of lung and liver vessels. The second criterion was overall artifact level, i. e. streak artifact and noise level of the images. For each reconstruction algorithm, mean and standard deviation of the ratings were calculated.

To analyze statistics, the paired Wilcoxon signed-rank test (Wilcoxon, 1945) was employed. It represents a non-parametric statistical hypothesis test to decide whether two data population distributions are identical. A statistical significant difference was assumed for P values smaller than 0.05. In addition to the absolute ranking, both radiologists chose the best reconstruction algorithm for each subject relative to the others using the same assessment criteria as above.

3.5.2 4D Respiratory Motion-Compensated PET

The purpose of the 4D PET study was to evaluate the potential of reducing the MR acquisition time used for motion estimation in simultaneous PET/MR respiratory motion compensation. Employing only a fraction of the MR acquisition time would allow for additional clinical MR examinations during the PET measurement as shown in Fig. 3.13 a. Simultaneous PET/MR data were simulated as illustrated in sections 3.3.2 and 3.3.3. The simulated MR data corresponded to a 1 min MR acquisition with 36 spokes per slice and motion phase. For the acquired data of six patients (s01 to s06, listed in Table 3.2), MR data with acquisition times of 1 min and 5 min were used (Fig. 3.13 a). An overview of the 4D PET study is given in Fig. 3.13 b. Respiratory MVFs were estimated from the

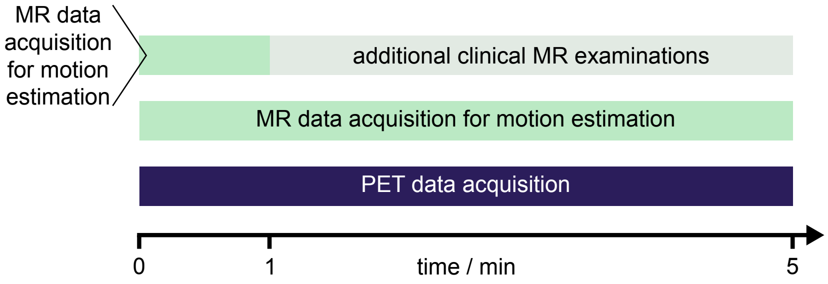

(a)

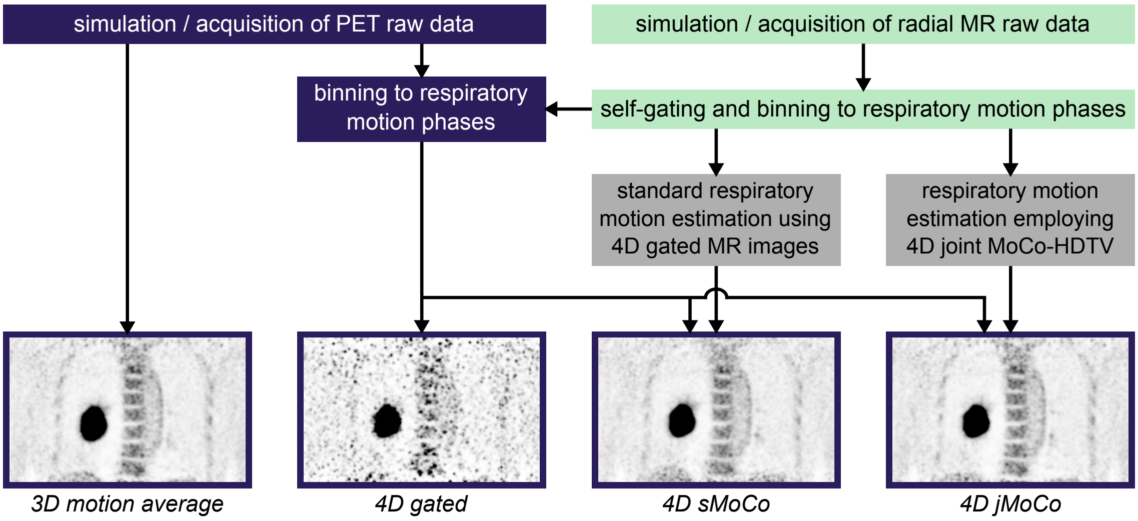

(b)

Figure 3.13: Overview of 4D PET study: (a) Simultaneous PET/MR data are either simulated or acquired and a variable amount of the MR acquisition time is used for respiratory motion estimation. In case of the 1 min acquisition block at the beginning, the remaining time may be employed for clinical MR examinations. (b) MR self-gating is carried out assigning the PET/MR data to different respiratory motion phases. Respiratory patient motion is estimated either using a standard method based on 4D gated MR images (4D sMoCo PET) or employing the 4D joint MoCo-HDTV algorithm (4D jMoCo PET). Subsequently, different PET reconstructions are performed.

simulated and acquired MR data either using the proposed 4D joint MoCo-HDTV, which is described in section 3.1.2 (4D jMoCo PET) or employing the standard motion estimation method from section 3.2.3 (4D sMoCo PET). 3D motion average and 4D gated PET images were reconstructed as indicated in section 3.2.1. Furthermore, 4D sMoCo PET and 4D jMoCo PET reconstructions were performed employing the MoCo OSEM algorithm (section 3.2.2). For both MoCo PET methods, the corresponding respiratory MVFs derived from MR were applied.

Quantitative Evaluation of Image Reconstructions

To evaluate the different PET reconstruction methods for motion handling quantitatively, lung lesions revealing high tracer uptake were analyzed. For the simulated PET data, the regions of interest used for analysis were isolated from the ground truth. For the acquired patient data, lung lesions were selected in end-exhale. An automatic isocontour segmentation was employed for analyzing each selected volume of interest (VOI). Starting from the voxel with the highest activity value within the VOI, a region growing was carried out until no connected voxels with activity values larger than a specified threshold were found. Using values between 20 and 50% of the maximum, thresholds were adjusted for each lesion individually depending on its homogeneity and contrast to surrounding tissue. To measure background activity values, manually selected VOIs were used, which were identical for the different PET reconstruction methods. From the local activity concentration values $c_A(\boldsymbol{r})$ obtained from the reconstructed PET images, SUVs were calculated for the segmented voxels:

$$\mathrm{SUV}(\boldsymbol{r}) = \frac{c_A(\boldsymbol{r})}{A\,m}. \tag{3.31}$$

While A denotes the decay-corrected total injected activity, m represents the patient weight. For each lesion, the mean standardized uptake value ($\mathrm{SUV}_{\mathrm{mean}}$) and the maximum standardized uptake value ($\mathrm{SUV}_{\mathrm{max}}$) were determined. In addition, contrast and SNR were calculated, defined similarly to previous studies (Kinahan and Karp, 1994; Fürst et al., 2015):

$$\mathrm{contrast} = \frac{\bar{\mu}_{\mathrm{lesion}} - \bar{\mu}_{\mathrm{background}}}{\bar{\mu}_{\mathrm{background}}}, \tag{3.32}$$

$$\mathrm{SNR} = \frac{\bar{\mu}_{\mathrm{lesion}} - \bar{\mu}_{\mathrm{background}}}{\bar{\sigma}_{\mathrm{background}}}. \tag{3.33}$$

While $\bar{\mu}$ denotes the mean value of a VOI, $\bar{\sigma}$ represents its standard deviation. As a further parameter for evaluation, the FWHM of lesions was calculated for simulated data. For that purpose, a Gaussian fit along the head–feet direction was performed for each spherical lesion. For patient data, lesion volume was evaluated instead due to the inhomogeneity and non-spherical shape of several lesions. For statistical analysis, the paired Wilcoxon signed-rank test (Wilcoxon, 1945) was applied and P values smaller than 0.05 were considered to indicate a statistically significant difference.

3.5.3 5D Respiratory and Cardiac Motion-Compensated MRI

In the 5D MRI study, the extension of MoCo image reconstruction considering both the respiratory and the cardiac dimension was investigated. For this purpose, 5D reconstructions of contrast-enhanced MR data of eleven patients (p03 to p13 as listed in Table 3.2) were evaluated. For all subjects, highly undersampled data sets with an acquisition time of 1 min 55 s were created (section 3.4.2). In case of 5D reconstructions, these data revealed radial undersampling factors of 36. As illustrated in Fig. 3.14, the following images were reconstructed for all subjects: 3D motion average and 5D double-gated reconstructions, which represent standard methods (section 3.1.1), 4D respiratory MoCo, 5D respiratory MoCo and cardiac gated, and 5D respiratory and cardiac MoCo images as described in section 3.1.4.

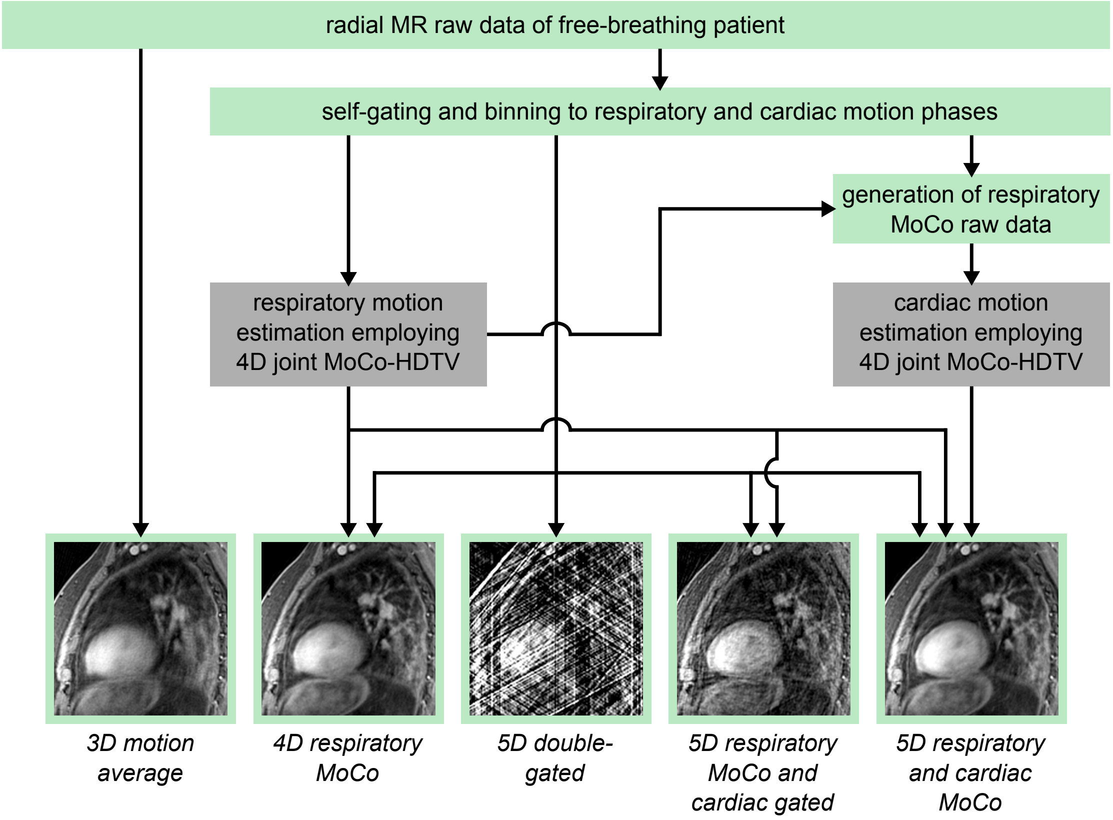

Figure 3.14: Overview of 5D MRI study: Radial MR data of free-breathing patients are acquired. After self-gating, MR data are binned to different combinations of respiratory and cardiac motion phases. Respiratory motion is estimated and respiratory MoCo raw data are generated. These raw data are used for estimation of cardiac motion. Using the respiratory and cardiac MVFs, several MR image reconstructions are performed.

Assessment of Image Sharpness

For quantitative assessment of potential improvements in image sharpness in MoCo reconstructions, reconstructed images of all patients were analyzed. For that purpose, the image gradient $\mathrm{TV}(\boldsymbol{f})$ was employed as a metric for image sharpness (McGee et al., 2000; Kingston et al., 2011):

$$\mathrm{TV}(\boldsymbol{f}) = \sum_i \sqrt{(\boldsymbol{\nabla}_x f_i)^2 + (\boldsymbol{\nabla}_y f_i)^2 + (\boldsymbol{\nabla}_z f_i)^2}. \tag{3.34}$$

The index i represents the voxel position and, instead of finite differences, the gradient operators $\boldsymbol{\nabla}_{xyz}$ correspond to 3D Sobel operators in the respective spatial direction. The comparison included 3D motion average, 4D respiratory MoCo, and 5D respiratory and cardiac MoCo reconstructions. These methods were chosen as they showed similar streak artifact and noise levels in contrast to the 5D respiratory and cardiac gated and 5D respiratory MoCo and cardiac gated images. The latter reconstructions were excluded due to their increased noise and artifact levels, which introduce artificial edges to the images and would bias the gradient calculation.

In addition, the three methods with similar streak artifact and noise levels selected above were evaluated independently by two board-certified radiologists. Both radiologists had at least five years of experience in reading thoracic MR images. The evaluation was blinded and the order of reconstruction methods was randomized for each patient so that the reconstruction method of each image was unknown to the readers. Criteria for the assessment were the following: sharpness of the edge of the diaphragm and of the lung parenchyma, sharpness of the borders and walls of the heart, and delineation and sharpness of the papillary muscles. Both radiologists defined a relative order of image sharpness for each patient assigning the values -1 (worst), 0, and $+1$ (best) to the reconstructed images. From the resulting values, mean and standard deviation were calculated for each reconstruction method. Applying the paired Wilcoxon signed-rank test (Wilcoxon, 1945), a statistically significant difference was assumed for P values smaller than 0.05. To determine the interrater agreement, Cohen's kappa coefficient (McHugh, 2012) was calculated with equal weights.

3.5.4 5D Respiratory and Cardiac Motion-Compensated PET

The 5D PET study was intended to assess potential improvements in image sharpness and quantification accuracy when applying respiratory and cardiac MVFs estimated from MR data to MoCo PET reconstruction of the heart. The evaluation comprised acquired simultaneous PET/MR data of four patients (s02 to s04 and s06 as listed in Table 3.2). As illustrated in Fig. 3.15, respiratory and cardiac MVFs were estimated on basis of

5 min MR acquisitions using the methods described in section 3.1.4. Besides the standard PET reconstruction methods 3D motion average and 5D double-gated (section 3.2.1), 5D respiratory and cardiac MoCo PET reconstructions employing respiratory and cardiac MVFs estimated from MR (section 3.2.2) were performed.

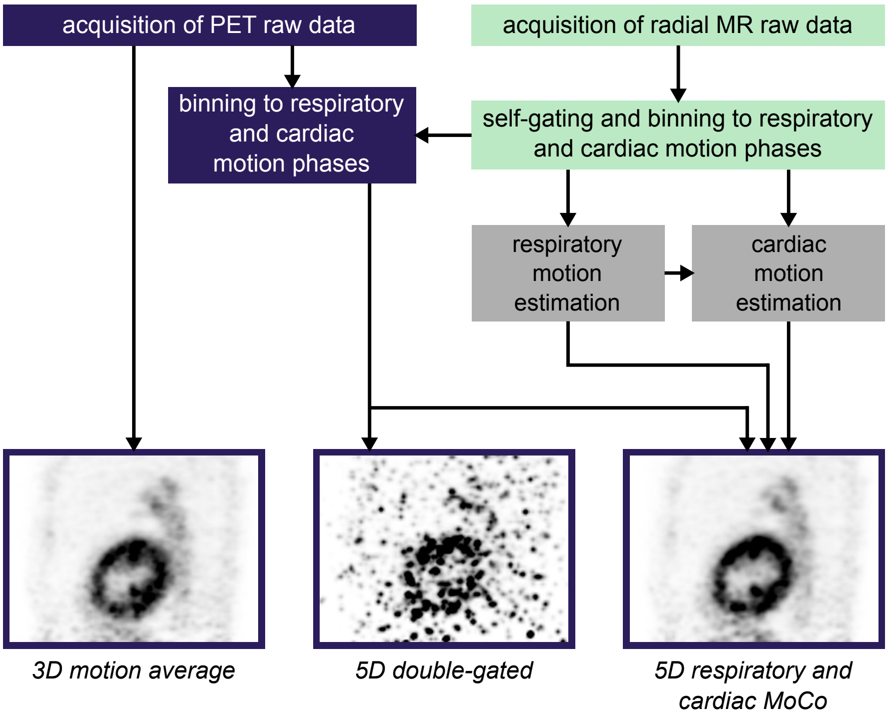

Figure 3.15: Overview of 5D PET study: Simultaneous PET/MR data of patients during free breathing are acquired. MR self-gating signals are derived and MR and PET data are sorted into different combinations of respiratory and cardiac motion phases. Respiratory and cardiac MVFs are estimated on basis of MR data and several PET image reconstructions are carried out.

Quantitative Evaluation of Image Reconstructions

For quantitative analysis of the reconstructed images of the four patients, the parameters SUV_{mean}, SUV_{max}, volume, contrast and SNR of the myocardium were determined in a diastolic and a systolic cardiac motion phase and compared to 3D motion average images. The quantitative parameters were calculated in a similar manner as defined in section 3.5.2. 5D double-gated images were excluded from evaluation as robust segmentation of the myocardium was not possible due to the very high noise level of the images.

4 | Results

In this chapter, results of the different studies conducted in this work are presented. In accordance to the description of these studies in section 3.5, the chapter is divided into four main parts: In section 4.1, results of the 4D respiratory time-resolved MRI study are shown. Section 4.2 illustrates outcomes of the 4D respiratory MoCo PET study. Results obtained in the 5D respiratory and cardiac MoCo MRI study can be found in section 4.3. An evaluation of 5D respiratory and cardiac MoCo PET is carried out in section 4.4. Parts of the results presented in this chapter have been published in Rank et al. (2016a), Rank et al. (2016b), Rank et al. (2016c) and Rank et al. (2016d).

4.1 4D Respiratory Time-Resolved MRI

4.1.1 Qualitative Comparison of Images

To assess image quality of thoracic and abdominal structures employing the MR reconstruction methods described in Fig. 3.12, several examples are depicted in the following: Figure 4.1 shows MR image reconstructions of the end-exhale motion phase of simulated data with acquisition times as short as 20 s and 40 s. Results of acquired data of the end-exhale motion phase and a mid-ventilation phase are given in Fig. 4.2 and Fig. 4.3, respectively. In Fig. 4.4, reconstructions of different respiratory motion phases are presented. For acquired data, the respiratory motion states of the reference and of the highly undersampled raw data were slightly different, which was caused by the nonuniform breathing patterns of volunteers and patients. While the references were created from full acquisitions, the highly undersampled reconstructions corresponded to the first 37 to 41 s of these measurements only.

For simulated and acquired data, 3D motion average reconstructions showed strong blurring of structures in the lungs, in the liver and in the diaphragm region, which was caused by respiratory motion. Due to the strong undersampling, 4D gated reconstructions revealed severe streak artifacts and increased noise levels. Analyzing 4D MASTeR and 4D HDTV reconstructions, streak artifacts were reduced considerably in comparison to the 4D gated

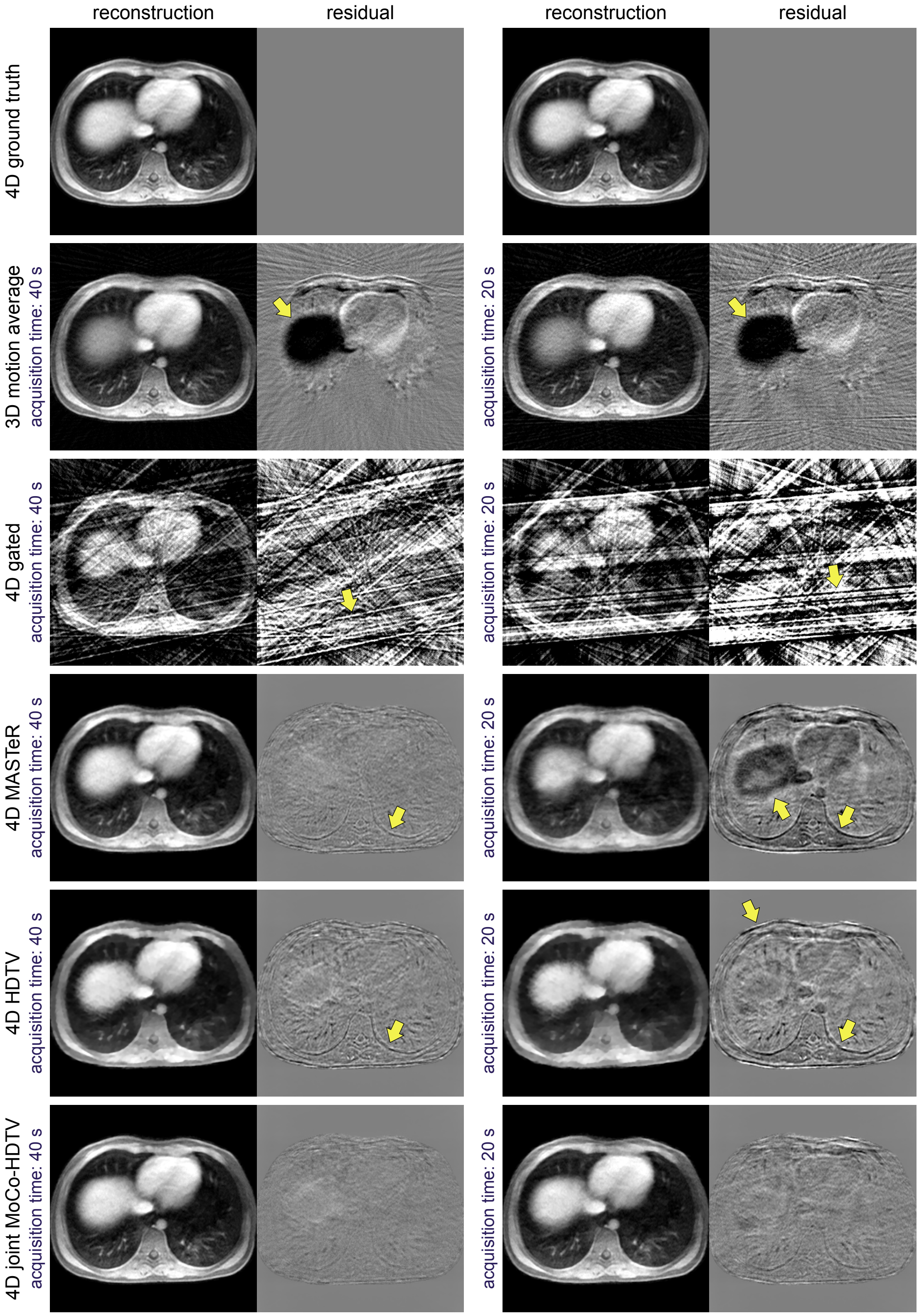

Figure 4.1: 4D MRI study: Ground truth and MR image reconstructions of highly undersampled raw data sets for simulated raw data in transversal slice orientation. Only the end-exhale motion phase is shown. The residuals represent difference images in comparison to the 4D ground truth amplified by a factor of two.

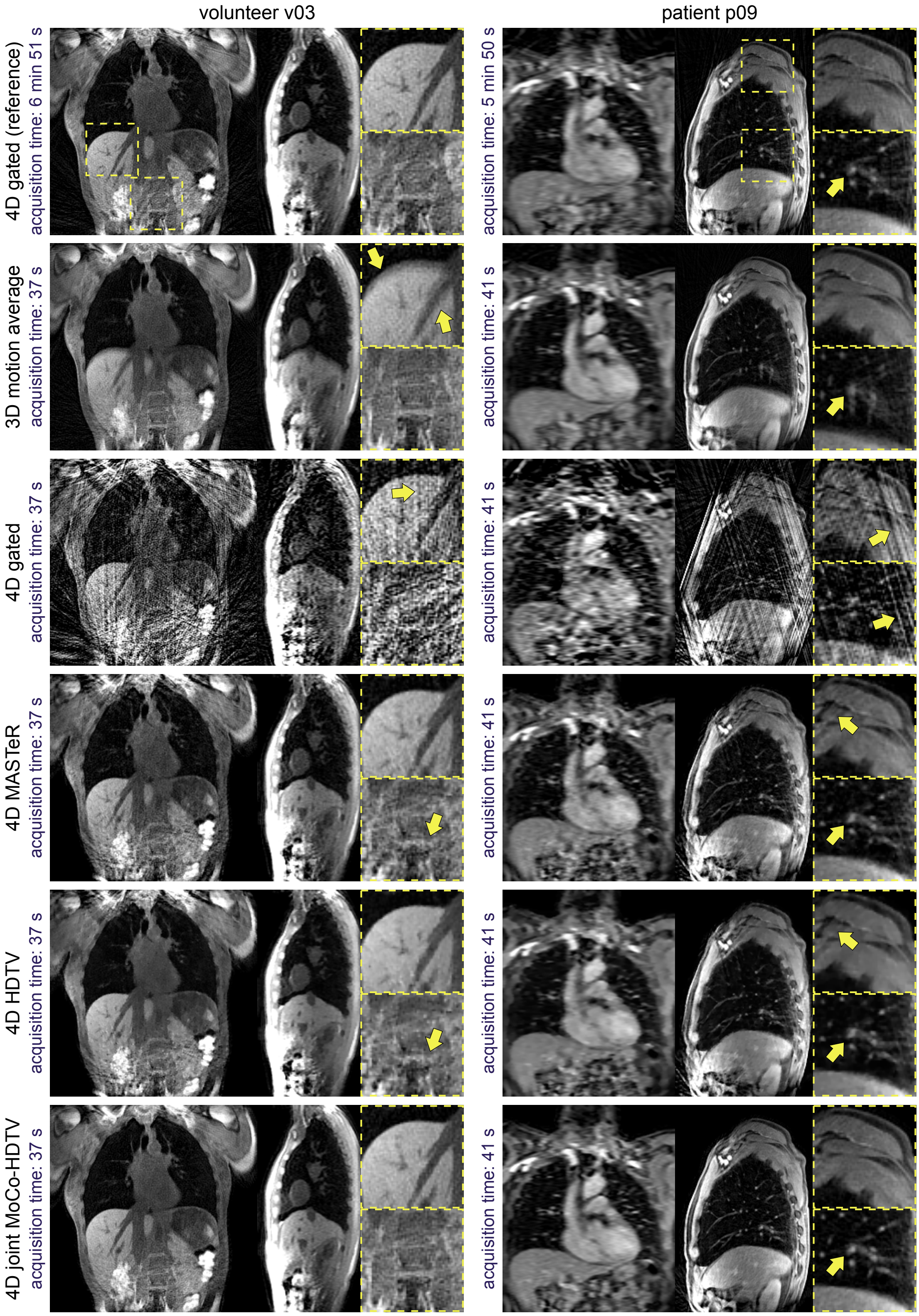

Figure 4.2: 4D MRI study: MR image reconstructions of reference and highly undersampled raw data sets from a 29-year-old female volunteer (v03, left) and from a 72-year-old male patient (p09, right) in end-exhale. Images were acquired in coronal and sagittal view, respectively, and upsampled to isotropic resolution for visualization. Adopted from Rank et al. (2016a).

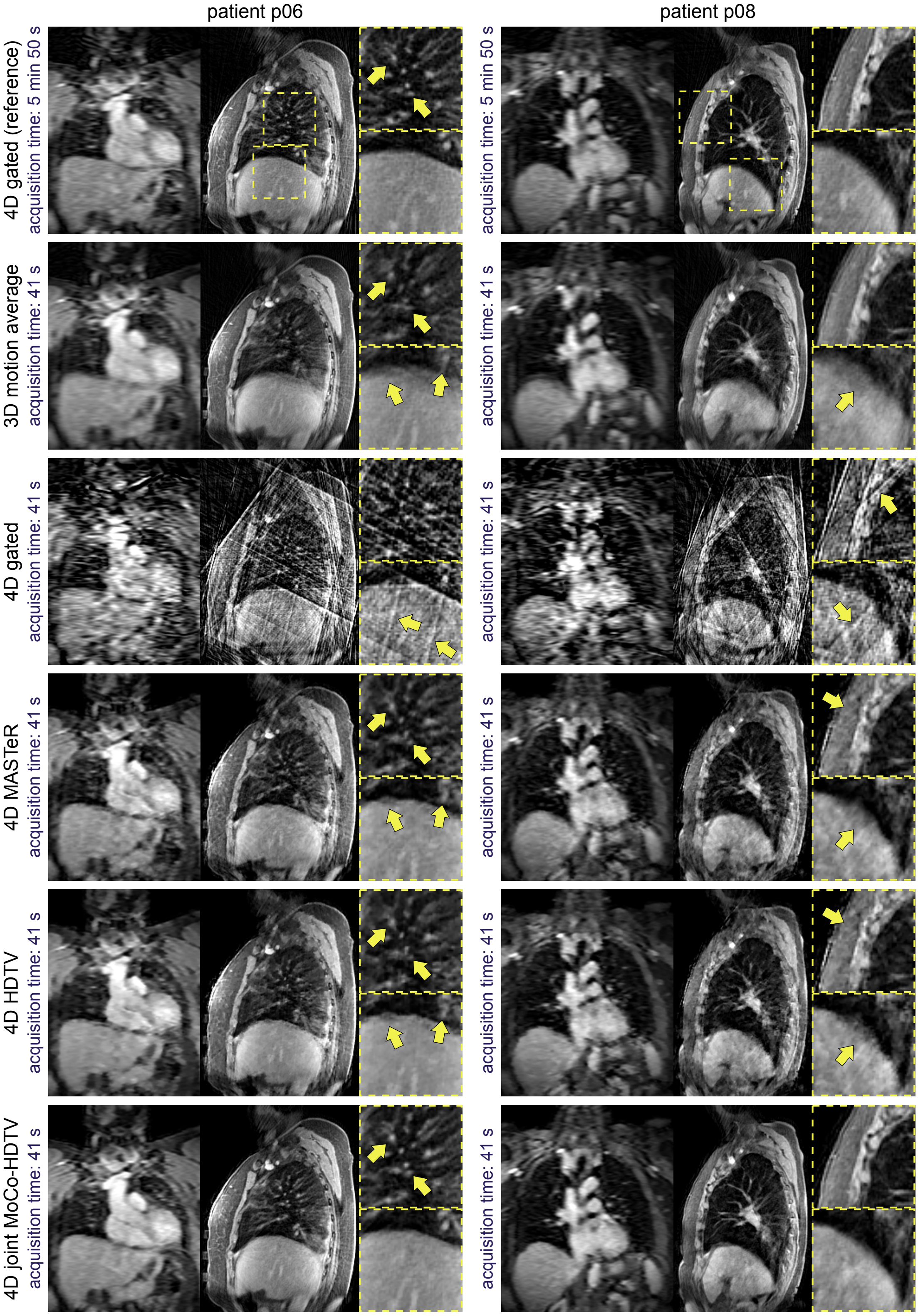

Figure 4.3: 4D MRI study: MR image reconstructions of reference and highly undersampled raw data sets from a 58-year-old female patient (p06, left) and from a 73-year-old female patient (p08, right) in a mid-ventilation motion phase. Images were acquired in sagittal view and upsampled to isotropic resolution for visualization. Adopted from Rank et al. (2016a).

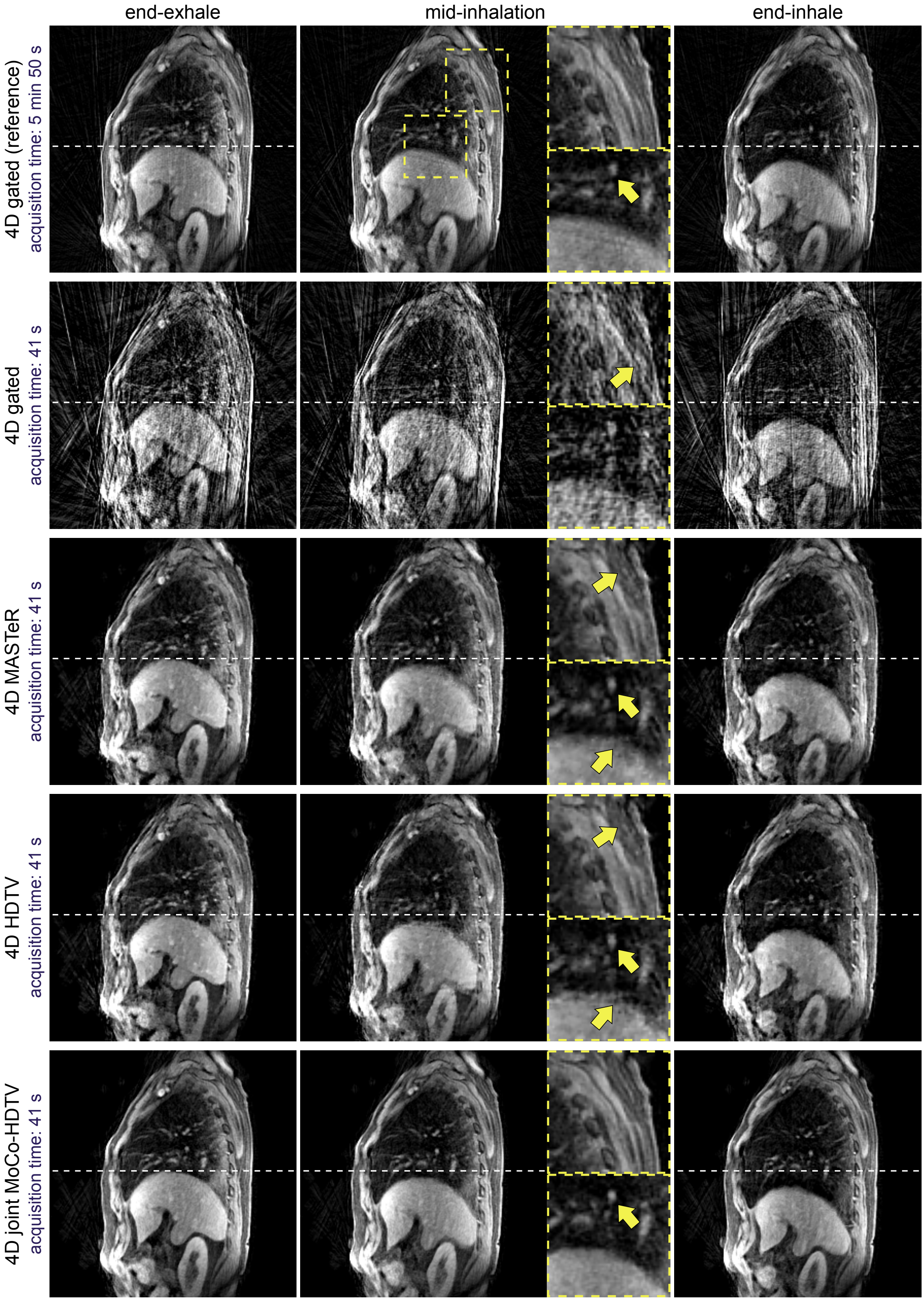

Figure 4.4: 4D MRI study: MR image reconstructions of different motion phases of reference and highly undersampled raw data sets from a 76-year-old male patient (p04) in sagittal view. Adopted from Rank et al. (2016a).

images. However, image sharpness was diminished in comparison to the ground truth and when compared to the reference reconstructions. Due to the strong regularization, patch-like and grainy textures were created in the images (Fig. 4.1 b, Fig. 4.3 and Fig. 4.4). 4D MASTeR yielded a slightly better image sharpness than 4D HDTV. Furthermore, grainy edges in motion phases with a high degree of motion were reduced as a result of the motion-adaptive regularization of MASTeR, which is illustrated for mid-inhalation phases in Fig 4.3 and Fig. 4.4. However, motion fidelity was reduced at very short acquisition times as can be seen in Fig. 4.1 b. The 4D joint MoCo-HDTV algorithm achieved lower streak artifact levels and higher image sharpness than 3D motion average, 4D gated, 4D HDTV and 4D MASTeR reconstructions of the highly undersampled data sets. For the simulated data, residual images showed the lowest differences to the ground truth when compared to the other techniques regardless of the acquisition time. For the acquired data, streak artifacts were less apparent for some subjects in 4D joint MoCo-HDTV reconstructions when compared to 4D gated images of the reference raw data sets, which were reconstructed from 6.6 to 11.1 times longer acquisition times (Fig. 4.2 a and Fig. 4.4). For the latter reconstruction technique, each motion phase was reconstructed from a different subset of spokes. As volunteers and patients exhibited nonideal breathing patterns, the angular spoke distributions of these subsets were not perfectly uniform in all cases. For some motion phases, this circumstance produced larger angular gaps between adjacent spokes and thus increased streak artifacts in the corresponding images. In contrast, 4D joint MoCo-HDTV reconstructions of the highly undersampled data sets were based on the same consecutively measured radial spokes for all motion phases resulting in nearly uniform angular spoke distributions. Furthermore, 4D joint MoCo-HDTV images revealed a slight decrease of motion fidelity when compared to the 4D ground truth or to the 4D reference gated images, especially when looking at structures at the interface of the lungs and the thorax. These regions exhibit abrupt changes in motion magnitude. This sliding lung motion was not modeled correctly by the image registration due to the fluid-like and diffusion-like regularization of MVFs. As a result, moving organs showed a slight underestimation of motion while some stationary structures were slightly affected by spurious motion.

4.1.2 Assessment of Image Quality

The evaluation of image similarity metrics for the different reconstruction algorithms is shown in Table 4.1 and in Fig. 4.5 for simulated and acquired data, respectively. For simulated data, 4D joint MoCo-HDTV outperformed 4D gated, 4D HDTV and 4D MASTeR reconstructions for all acquisition times yielding smaller MSEs and larger SSIM, NCC and NMI values when compared to the ground truth. In case of acquired data, the comparison to 4D reference gated reconstructions yielded the largest SSIM, NCC and NMI values for 4D joint MoCo-HDTV. These results demonstrate that the 4D joint MoCo-HDTV algorithm was able to restore a larger amount of image information from highly undersampled data than the other reconstruction techniques.

reconstruction algorithm	simulated acquisition time / s	MSE	SSIM	NCC	NMI
4D gated	60	1381	0.510	0.900	0.153
4D MASTeR	60	54	0.962	0.997	0.523
4D HDTV	60	83	0.931	0.993	0.465
4D joint MoCo-HDTV	60	30	0.978	0.998	0.583
4D gated	40	2552	0.391	0.834	0.107
4D MASTeR	40	81	0.941	0.995	0.470
4D HDTV	40	110	0.912	0.991	0.429
4D joint MoCo-HDTV	40	39	0.970	0.997	0.537
4D gated	20	6000	0.230	0.702	0.059
4D MASTeR	20	1104	0.722	0.985	0.225
4D HDTV	20	227	0.848	0.981	0.341
4D joint MoCo-HDTV	20	72	0.944	0.994	0.479

Table 4.1: 4D MRI study: Quantitative evaluation of simulated MR data: Image similarity metrics of the different reconstruction algorithms for several acquisition times when compared with 4D ground truth images. As described in section 3.5.1, the metrics mean squared error (MSE), structural similarity (SSIM), normalized cross-correlation (NCC) and normalized mutual information (NMI) were evaluated.

reconstruction algorithm	type of data set	score
4D gated	reference	3.29 ± 0.82
4D MASTeR	highly undersampled	2.63 ± 0.67
4D HDTV	highly undersampled	2.04 ± 0.74
4D joint MoCo-HDTV	highly undersampled	4.60 ± 0.49

Table 4.2: 4D MRI study: Qualitative assessment of image quality of acquired MR data: The values represent mean ± standard deviation of the scores given by two radiologists in a blinded study for a total number of twelve subjects (listed in Table 3.2). Adopted from Rank et al. (2016a).

Results of the qualitative assessment of image quality scores for acquired data by two radiologists are given in Table 4.2. 4D joint MoCo-HDTV images reconstructed from the highly undersampled raw data sets achieved significantly higher ($P < 0.05$) overall image quality scores when compared to 4D HDTV and 4D MASTeR reconstructions at the same undersampling factor and when compared to 4D gated reconstructions of the reference raw data sets. The lower scores of 4D reference gated images might be explained by residual streak artifacts being more apparent than for 4D joint MoCo-HDTV reconstructions as explained above. In the relative comparison of reconstruction algorithms, both radiologists agreed in 91.7% of cases (22 of 24 cases) and attributed the best image quality to 4D joint MoCo-HDTV.

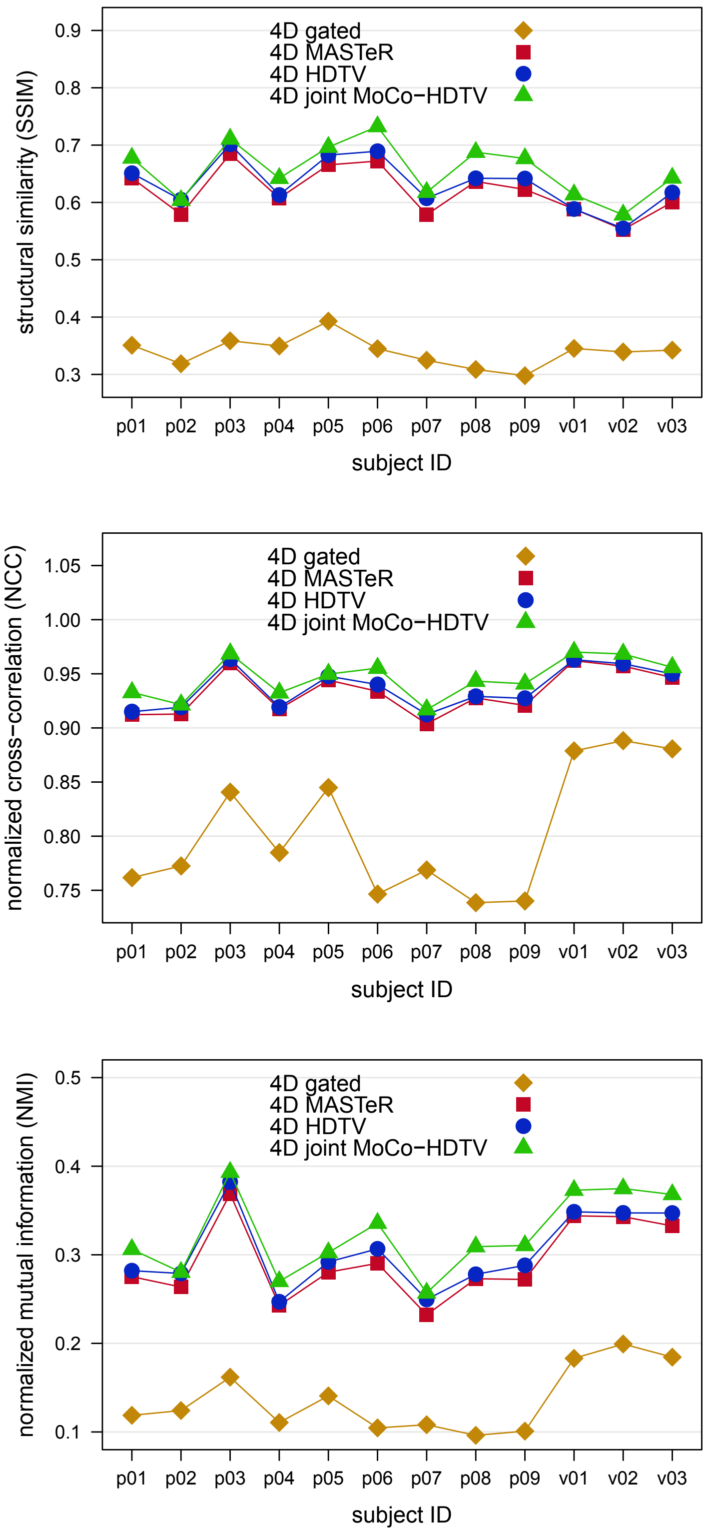

Figure 4.5: 4D MRI study: Quantitative evaluation of acquired MR data: Image similarity metrics of the different reconstruction algorithms when compared with reference 4D gated reconstructions. Adopted from Rank et al. (2016a).

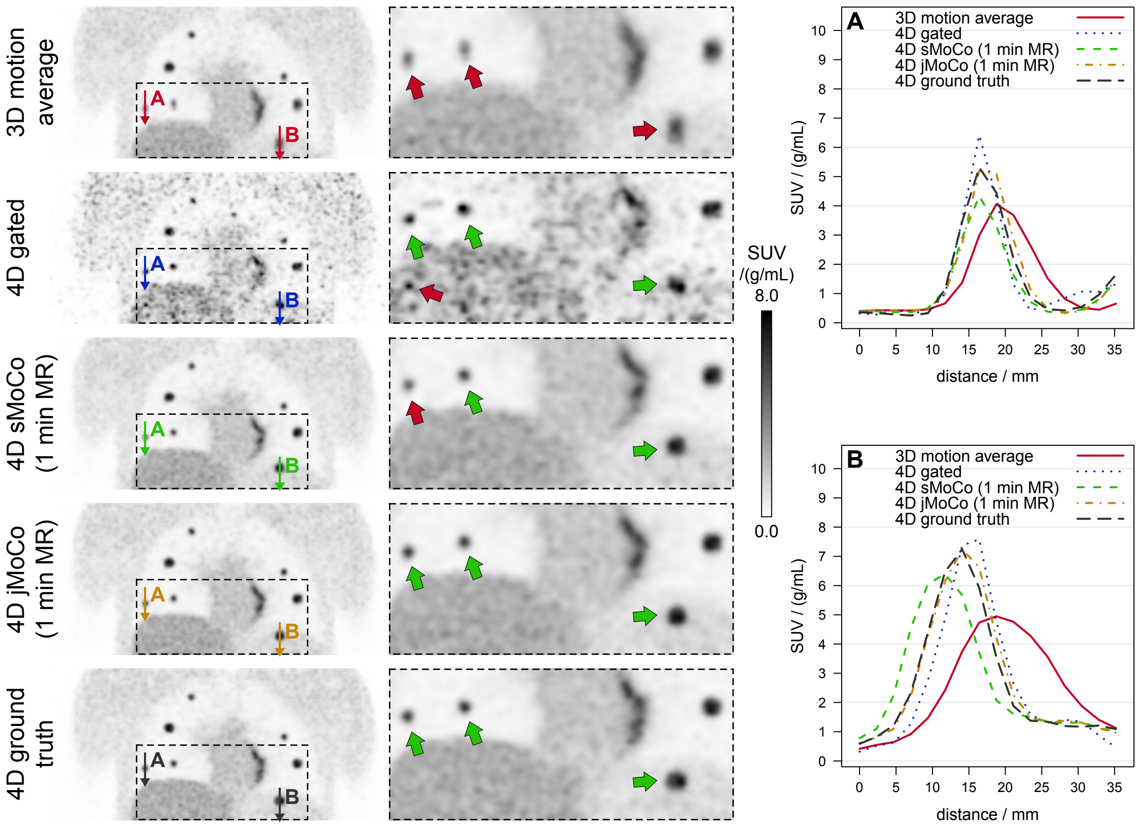

Figure 4.6: 4D PET study: PET reconstructions of an end-exhale motion phase of simulated data in coronal slice orientation. The positions of line profiles are indicated by arrows in the left column of the corresponding reconstructions. While green arrows in the central column imply visually appropriate quantification, red arrows demonstrate reduced accuracy of the latter. Adopted from Rank et al. (2016d).

4.2 4D Respiratory Motion-Compensated PET

4.2.1 Qualitative Comparison of Images

To evaluate the delineation of lung lesions using the PET reconstruction techniques depicted in Fig. 3.13, Fig. 4.6 shows reconstruction results of the PET/MR simulation while Fig. 4.7, Fig. 4.8 and Fig. 4.9 present PET images of three patients. 3D motion average images exhibited a blurring of structures affected by respiratory motion. 4D gated reconstructions showed increased noise levels due to the low statistics. All MoCo PET methods provided noise levels similar to the 3D motion average as 100% of the measured PET raw data were employed for reconstruction of each motion phase. 4D sMoCo PET images corresponding to the standard motion estimation technique yielded a decrease of motion blur for some lesions (Fig. 4.6 and Fig. 4.7) while blurring of other lesions was increased when using the 1 min MR acquisition for motion estimation (Fig. 4.8 and Fig. 4.9). In contrast, 4D jMoCo PET images employing the proposed 4D joint MoCo-HDTV algorithm were not

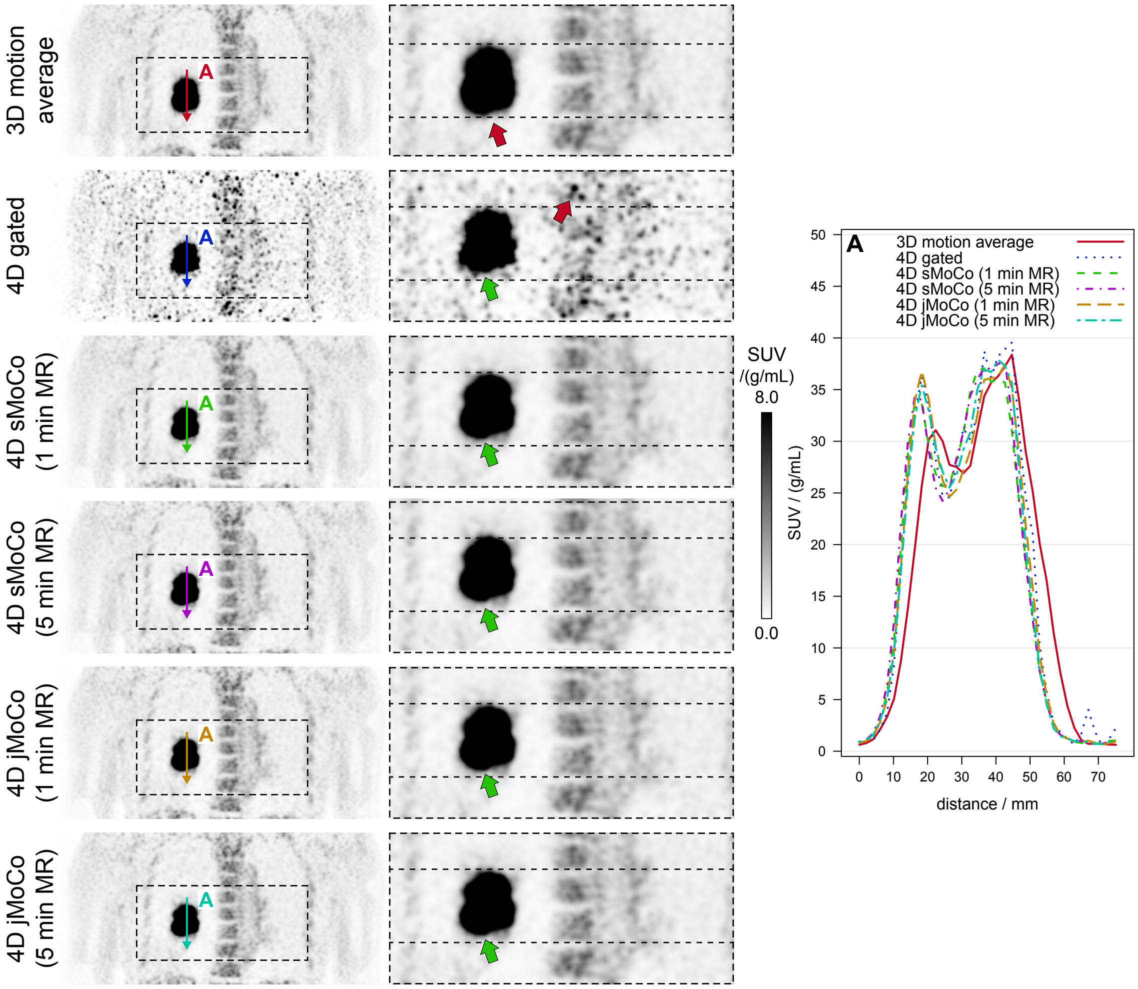

Figure 4.7: 4D PET study: PET reconstructions of an end-exhale motion phase of a 57-year-old male patient (s01) in coronal slice orientation. The positions of line profiles are indicated by arrows in the left column of the corresponding reconstructions. While green arrows in the central column imply visually appropriate quantification, red arrows demonstrate reduced accuracy of the latter. Adopted from Rank et al. (2016d).

affected by this degradation of image quality. Motion blurring of lesions was reduced regardless of the MR acquisition time used for motion estimation resulting in steeper line profiles with higher SUVs than 3D motion average images (Fig. 4.6, Fig. 4.8 and Fig. 4.9).

4.2.2 Quantitative Evaluation of Image Reconstructions

A graphical illustration of the parameters SUV_{mean}, SUV_{max}, FWHM/ lesion volume, contrast and SNR for simulated data and for acquired patient data is presented in Fig. 4.10 and Fig. 4.11, respectively. In general, 3D motion average images showed the lowest SUV_{mean}, SUV_{max} and contrast and the largest FWHM and lesion sizes. In contrast, 4D gated reconstructions exhibited the lowest SNR of all reconstruction methods. In case

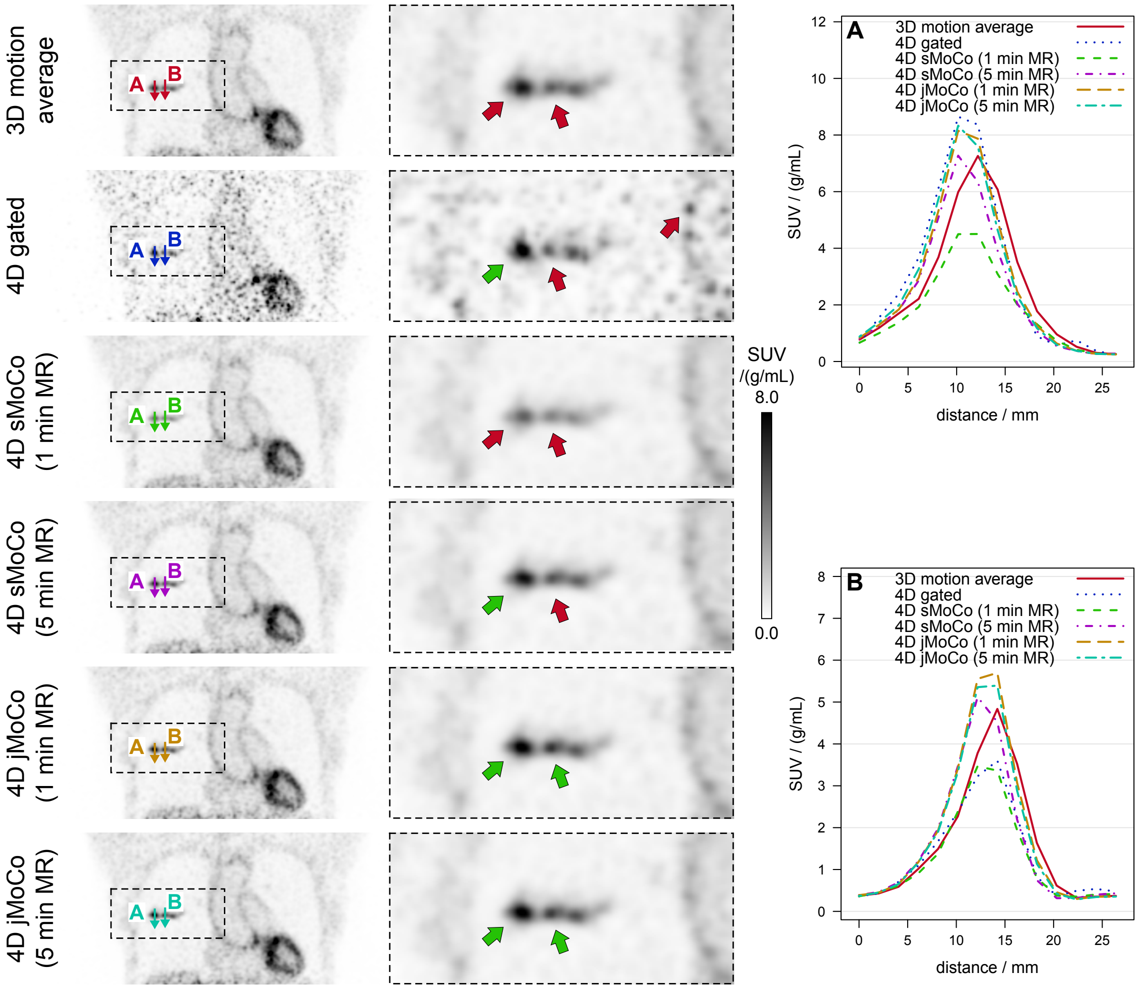

Figure 4.8: 4D PET study: PET reconstructions of an end-exhale motion phase of a 56-year-old female patient (s02) in coronal slice orientation. The positions of line profiles are indicated by arrows in the left column of the corresponding reconstructions. While green arrows in the central column imply visually appropriate quantification, red arrows demonstrate reduced accuracy of the latter.

of simulated data, 4D gated and 4D sMoCo PET images achieved increased $\mathrm{SUV}_{\mathrm{mean}}$, $\mathrm{SUV}_{\mathrm{max}}$ and contrast when compared to the 3D motion average. Being an improvement over motion average images, results did not fully match the values of 4D ground truth images. Considerable reduction of the FWHM of simulated lesions was found for all 4D PET reconstruction techniques. The proposed 4D jMoCo PET approach revealed the best agreement of quantitative parameters having a mean absolute deviation of 2.3% when compared to 4D ground truth images (Fig. 4.10). Relative to the 3D motion average, $\mathrm{SUV}_{\mathrm{mean}}$, $\mathrm{SUV}_{\mathrm{max}}$ and contrast were increased by 32.7% on average. For the acquired patient data, 4D gated images showed the highest values for $\mathrm{SUV}_{\mathrm{mean}}$, $\mathrm{SUV}_{\mathrm{max}}$ and contrast (Fig. 4.11). Owing to the increased image noise, $\mathrm{SUV}_{\mathrm{max}}$ was systematically overestimated resulting in an underestimation of lesion volume when employing the automatic isocontour

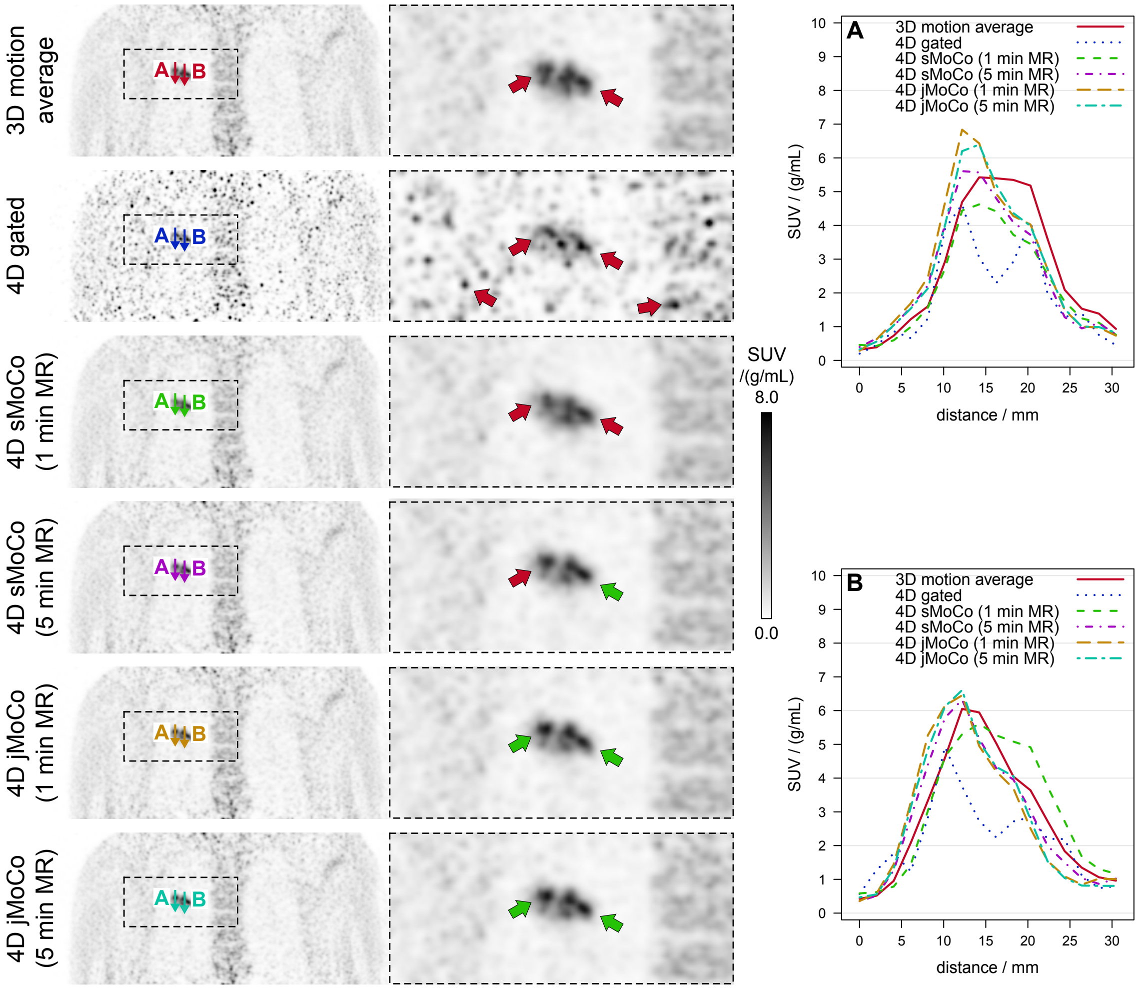

Figure 4.9: 4D PET study: PET reconstructions of an end-exhale motion phase of a 75-year-old male patient (s05) in coronal slice orientation. The positions of line profiles are indicated by arrows in the left column of the corresponding reconstructions. While green arrows in the central column imply visually appropriate quantification, red arrows demonstrate reduced accuracy of the latter. Adopted from Rank et al. (2016d).

segmentation described in section 3.5.2. This effect yielded an overestimation of $\mathrm{SUV}_{\mathrm{mean}}$ and contrast. In comparison to 3D motion average images, 4D sMoCo PET showed an average increase of the parameters $\mathrm{SUV}_{\mathrm{mean}}$, $\mathrm{SUV}_{\mathrm{max}}$ and contrast by 3.6% and 10.0% for the 1 min and 5 min MR acquisition time, respectively. This result demonstrates a reduced quantification accuracy for the short MR acquisition time. In contrast, the proposed 4D jMoCo PET yielded an average increase of $\mathrm{SUV}_{\mathrm{mean}}$, $\mathrm{SUV}_{\mathrm{max}}$ and contrast being similar for both acquisition times. This gain was 12.7% (1 min MR) and 13.2% (5 min MR) and thus larger than for the 4D sMoCo PET approach regardless of the acquisition time. In comparison to the 3D motion average and to 4D sMoCo PET (1 min MR), the increase was statistically significant ($P < 0.05$) for both the simulated data and the acquired patient data.

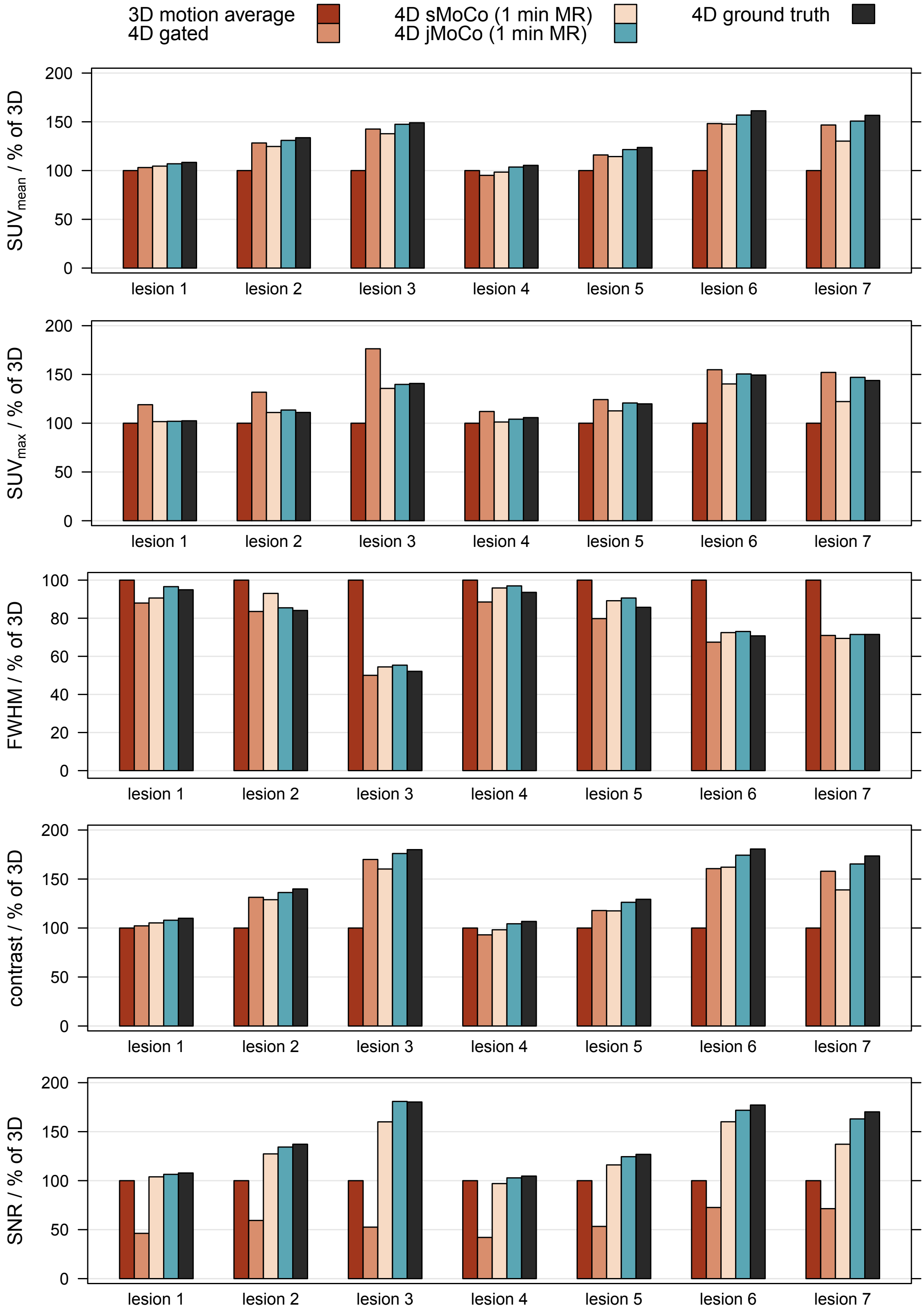

Figure 4.10: 4D PET study: Quantitative evaluation of seven lesions of the simulated PET data set. Adopted from Rank et al. (2016d).

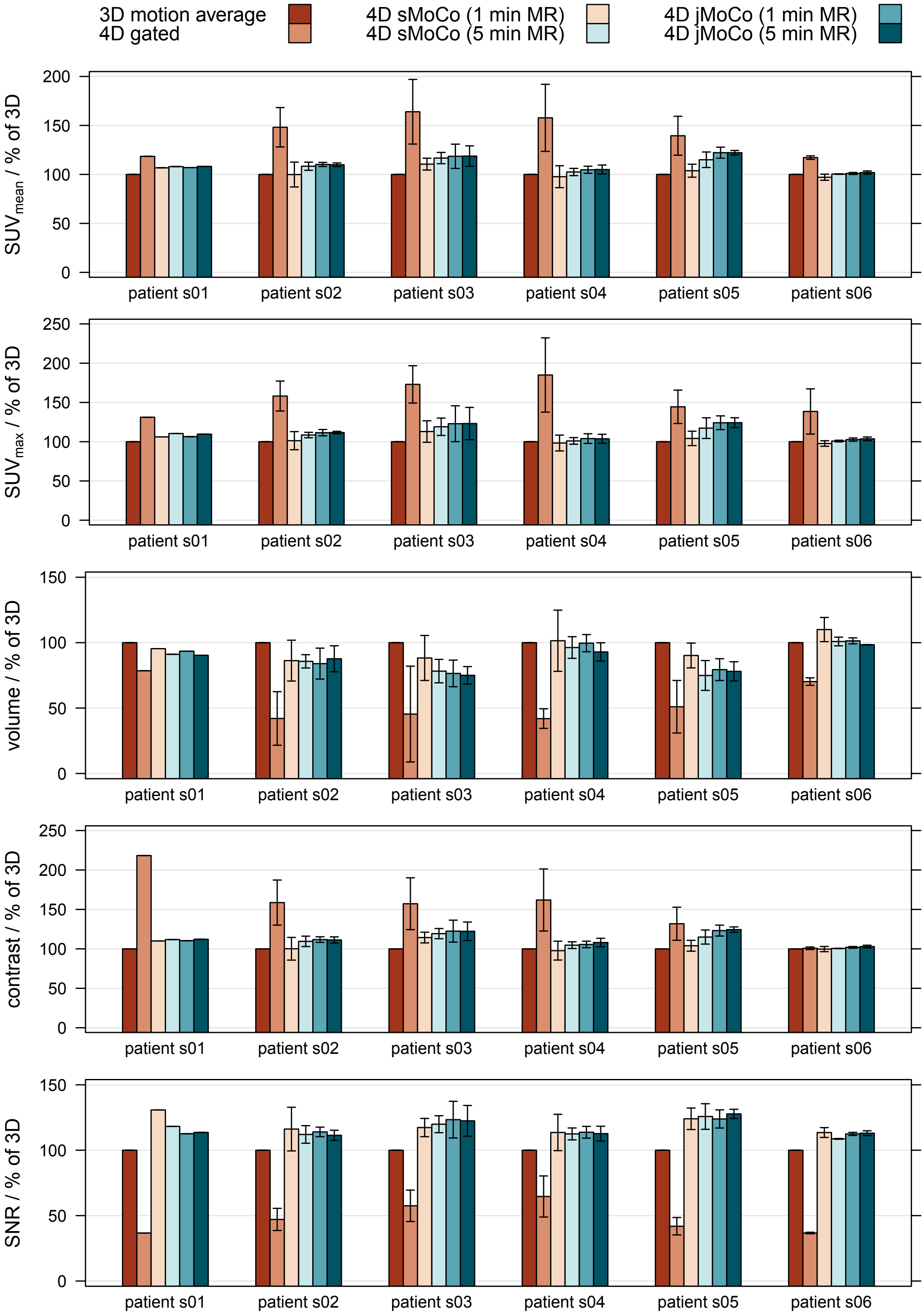

Figure 4.11: 4D PET study: Quantitative evaluation of PET data sets of six patients (listed in Table 3.2) with several lesions each. Mean and standard deviation of the lesions are drawn for each patient. Adopted from Rank et al. (2016d).

4.3 5D Respiratory and Cardiac Motion-Compensated MRI

4.3.1 Qualitative Comparison of Images

To compare image sharpness of cardiac structures applying the different MR reconstruction methods illustrated in Fig. 3.14, the following examples are given: Figures 4.12 and 4.13 present MR image reconstructions of the combination of an end-exhale respiratory phase and a diastolic cardiac phase in four patients. In addition, 5D respiratory and cardiac MoCo reconstructions of different combinations of respiratory and cardiac motion phases for two patients are shown in Fig. 4.15 and Fig. 4.14. In correspondence to the results in section 4.1, 3D motion average images exhibited blurring in regions, which are affected by respiratory and cardiac motion, e. g. at the lung parenchyma, at the edge of the diaphragm or at the borders and walls of the heart (Fig. 4.12 and Fig. 4.13). 4D respiratory MoCo reconstructions reduced respiratory blurring considerably when compared to the motion average. However, cardiac structures, e. g. the cardiac walls and the papillary muscles, were still affected by cardiac motion blur. While resolving both respiratory and cardiac motion, 5D double-gated images were distorted by very severe streak artifacts and noise due to the very high radial undersampling, such that the detection of cardiac structures was not possible. The artifact level was decreased in 5D respiratory MoCo and cardiac gated reconstructions and sharpness of cardiac structures was improved when compared to 4D respiratory MoCo images. Likewise, 5D respiratory and cardiac MoCo reconstructions yielded a similar improvement of sharpness of these structures as the images were fully compensated for organ motion (Fig. 4.12 and Fig. 4.13). Furthermore, this reconstruction technique resulted in noise and streak artifacts comparable to the motion average as 100% of the measured raw data were available for reconstruction of each motion phase. Analyzing the cardiac motion cycle at different respiratory phases (Fig. 4.15 and Fig. 4.14), the various cardiac phases were clearly resolved regardless of the respiratory motion state.

4.3.2 Assessment of Image Sharpness

Figure 4.16 shows image gradient values $\mathrm{TV}(\boldsymbol{f})$ as defined in Eq. (3.34) serving as quantitative metric for image sharpness for the different MR image reconstruction methods. For all eleven patients, 5D respiratory and cardiac MoCo images achieved the largest gradient values and thus the best image sharpness, followed by 4D respiratory MoCo and 3D motion average images.

Results of the relative assessment of image sharpness by two radiologists are shown in Table 4.3. On the relative scale, 5D respiratory and cardiac MoCo reconstructions revealed significantly higher scores for image sharpness than 3D motion average images and 4D respiratory MoCo images, i. e. P values were smaller than 0.05. 3D motion average images

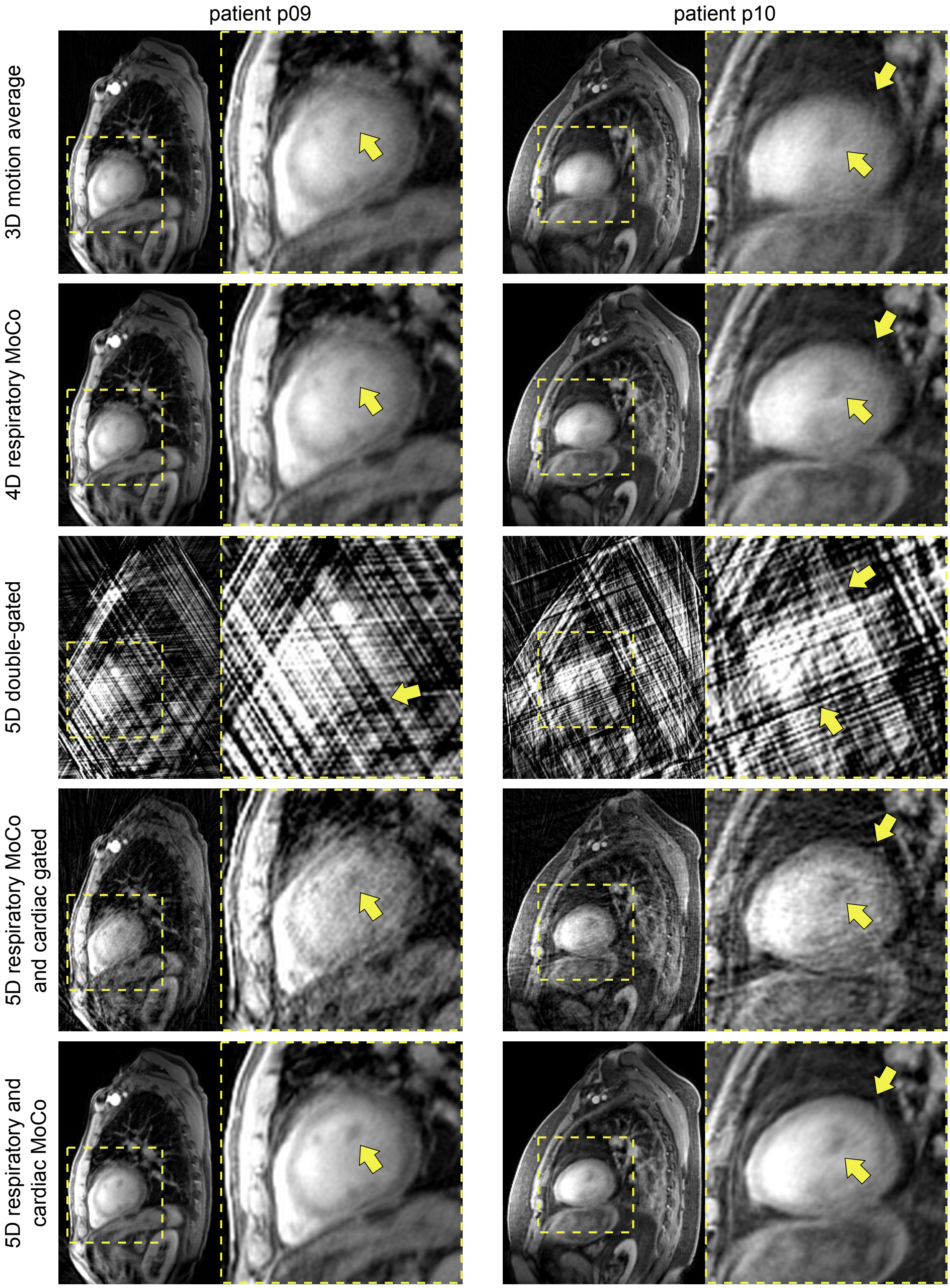

Figure 4.12: 5D MRI study: MR image reconstructions of a 72-year-old male patient (p09, left) and of a 73-year-old male patient (p10, right) in sagittal orientation. A combination of end-exhale respiratory phase and a diastolic cardiac phase is shown.

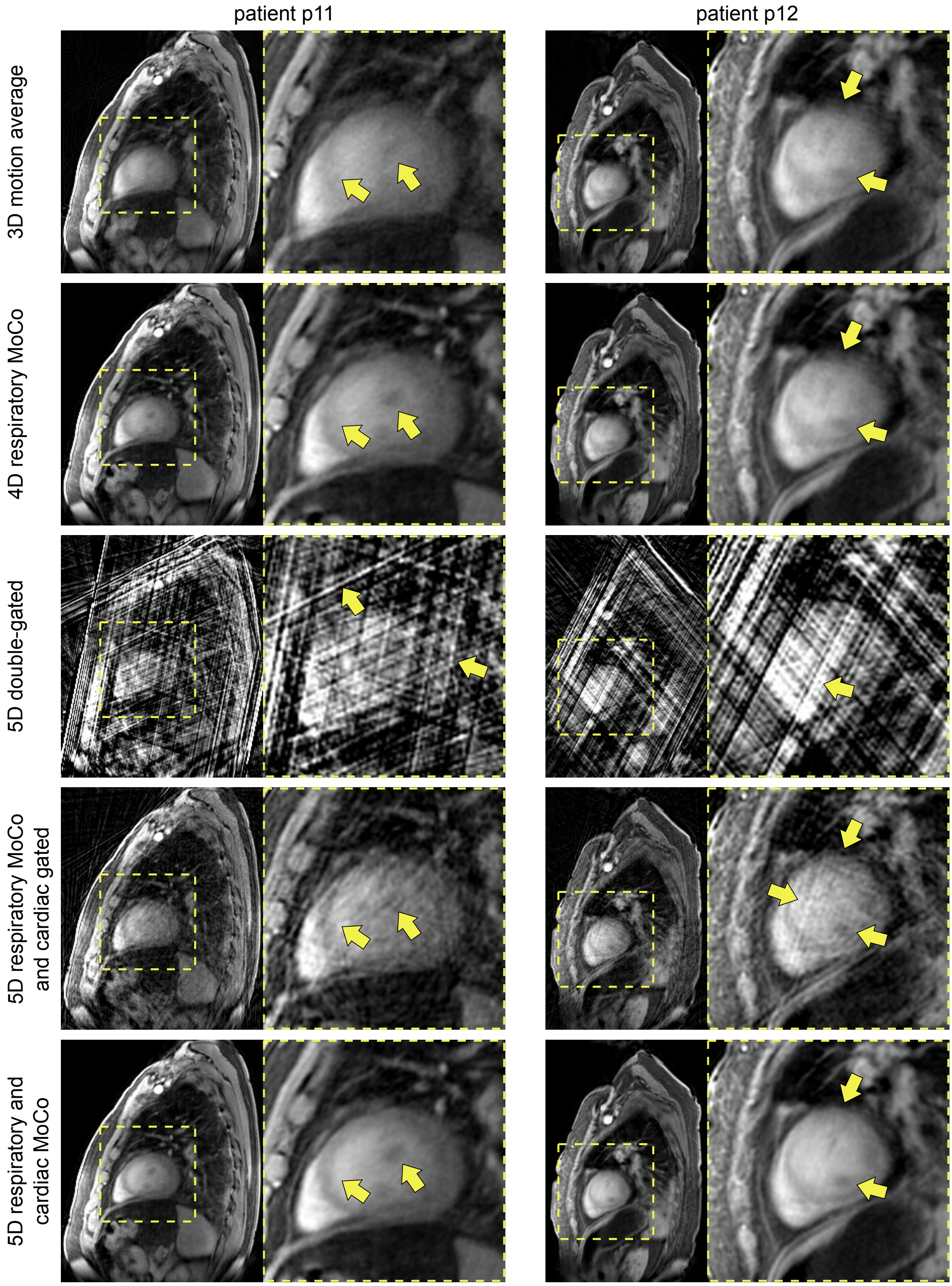

Figure 4.13: 5D MRI study: MR image reconstructions of a 64-year-old male patient (p11, left) and of a 79-year-old female patient (p12, right) in sagittal orientation. A combination of end-exhale respiratory phase and a diastolic cardiac phase is shown.

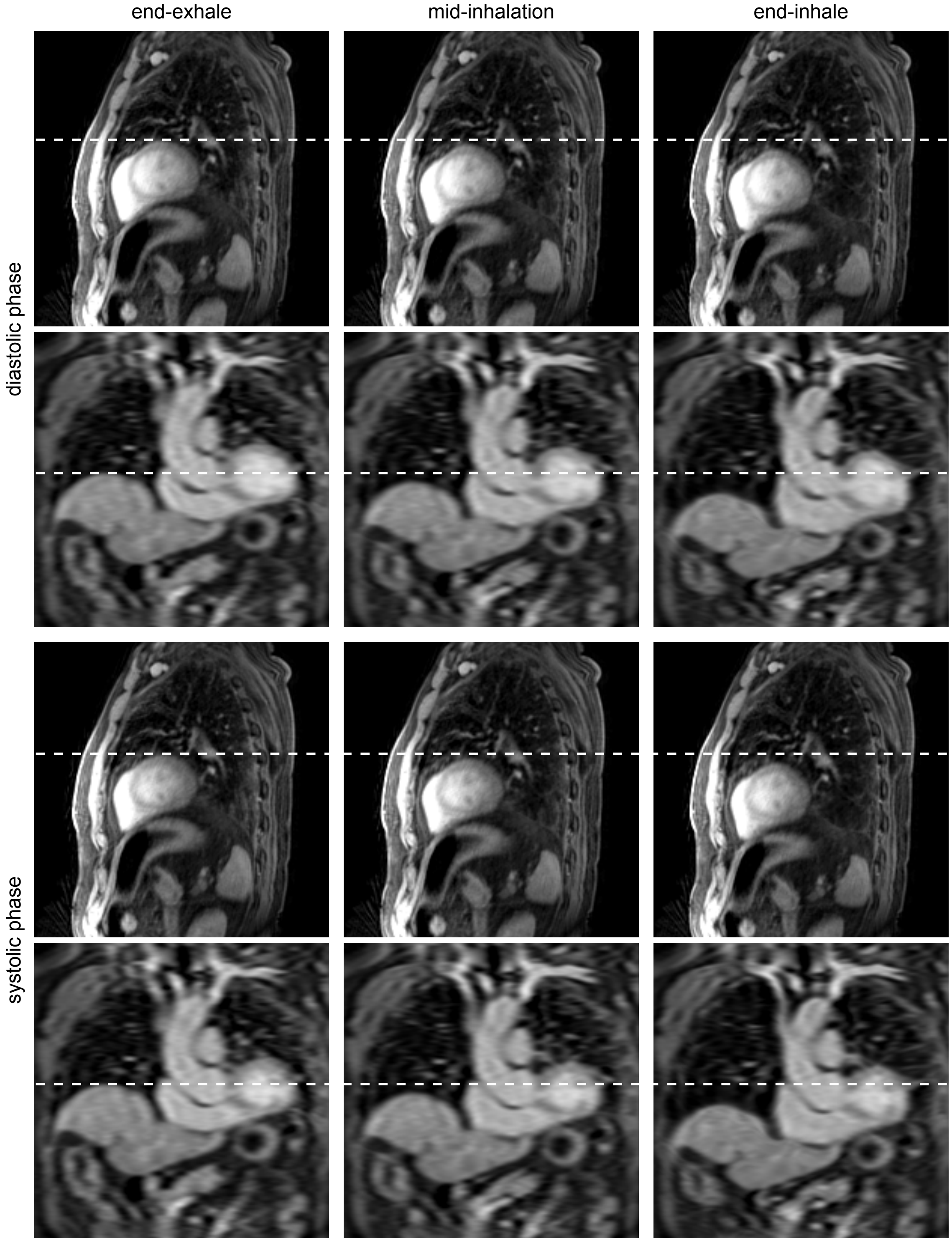

Figure 4.14: 5D MRI study: MR image reconstruction of different combinations of respiratory and cardiac motion phases from a 76-year-old male patient (p04). Images were acquired in sagittal orientation and the slice direction was upsampled to isotropic resolution for visualization.

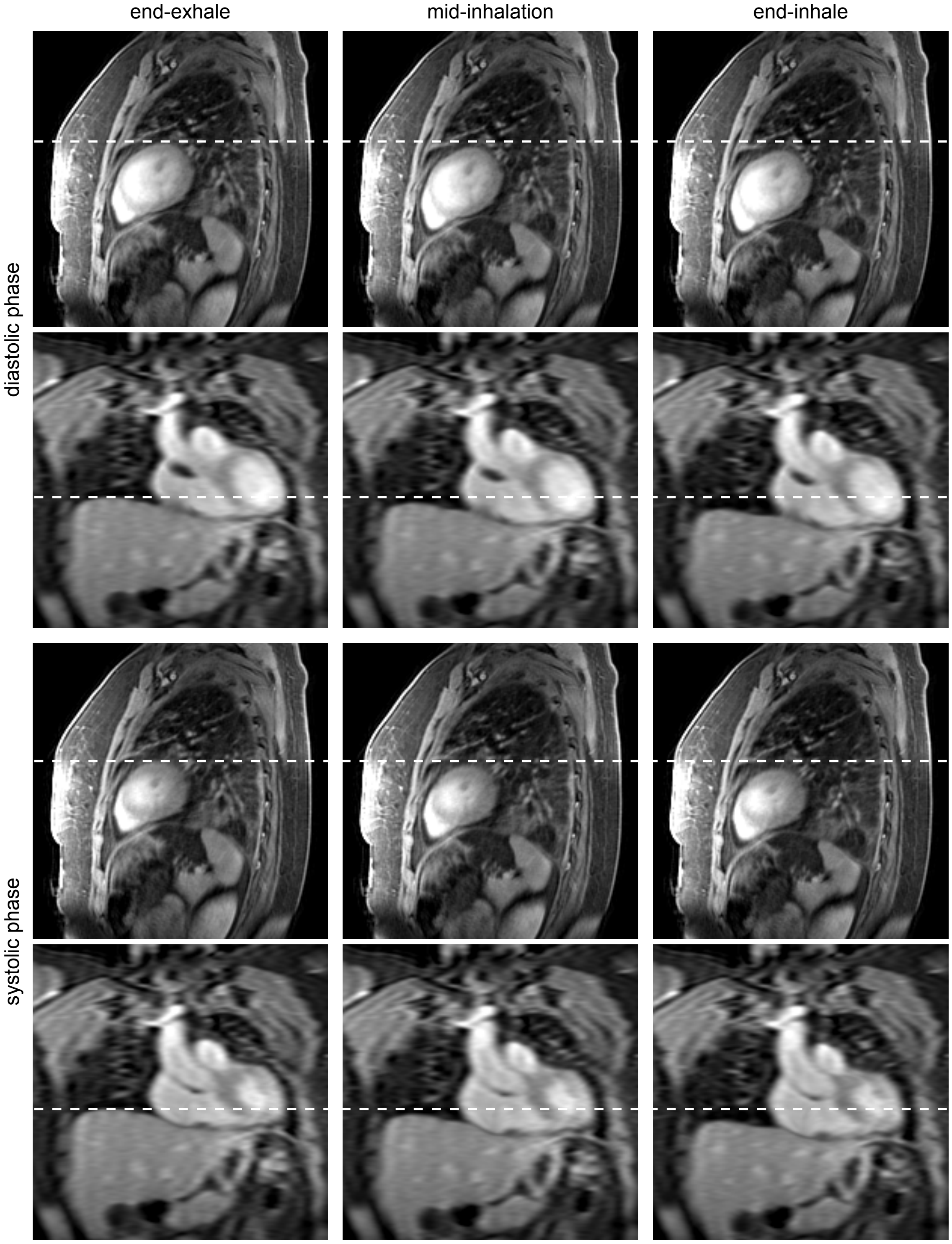

Figure 4.15: 5D MRI study: MR image reconstruction of different combinations of respiratory and cardiac motion phases from a 58-year-old female patient (p06). Images were acquired in sagittal orientation and the slice direction was upsampled to isotropic resolution for visualization.

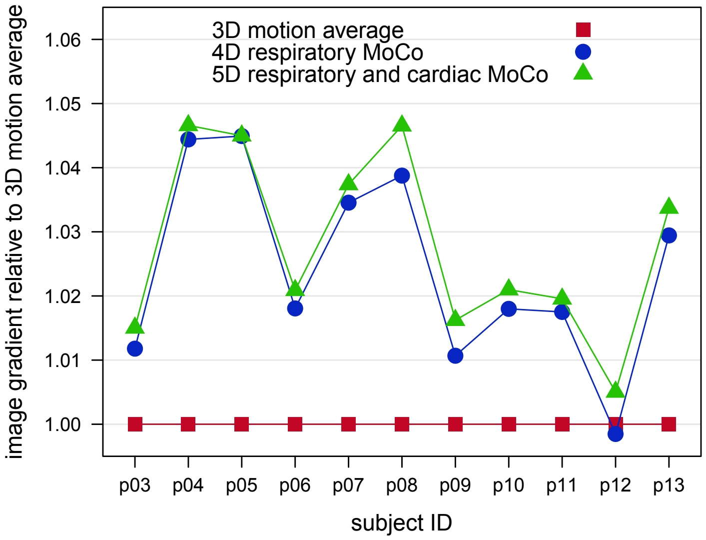

Figure 4.16: 5D MRI study: Quantitative evaluation of image sharpness metric for the different reconstruction methods relative to the 3D motion average.

reconstruction algorithm	score
3D motion average	-1.00 ± 0.00
4D respiratory MoCo	$+0.27 \pm 0.46$
5D respiratory and cardiac MoCo	$+0.73 \pm 0.46$

Table 4.3: 5D MRI study: Qualitative assessment of image sharpness: The values represent mean ± standard deviation of the relative scores given by two radiologists in a blinded study for a total number of eleven subjects (listed in Table 3.2).

were assigned with the lowest image sharpness scores for all subjects. The differences between 4D respiratory MoCo and 5D respiratory and cardiac MoCo were less apparent. The interrater agreement of the two radiologists, i. e. Cohen's kappa coefficient, was calculated as 0.73, which can be interpreted as a moderate agreement (McHugh, 2012).

4.4 5D Respiratory and Cardiac Motion-Compensated PET

4.4.1 Qualitative Comparison of Images

To investigate the feasibility of the methods developed in this work for cardiac PET imaging, Fig 4.17 and Fig. 4.18 present reconstructions of two patients comparing three different approaches. Similar to sections 4.2 and 4.3, 3D motion average images exhibited motion blurring resulting from respiratory and cardiac motion. As gating was performed in two temporal dimensions, 5D double-gated reconstructions showed very severe noise levels, e. g. impairing the delineation of the myocardium. While having noise levels comparable to the 3D motion average, 5D respiratory and cardiac MoCo reconstructions yielded reduced motion blurring revealing steeper line profiles through the myocardium than the former (Fig 4.17 and Fig. 4.18). This improvement of edge sharpness was demonstrated for diastolic and systolic motion phases.

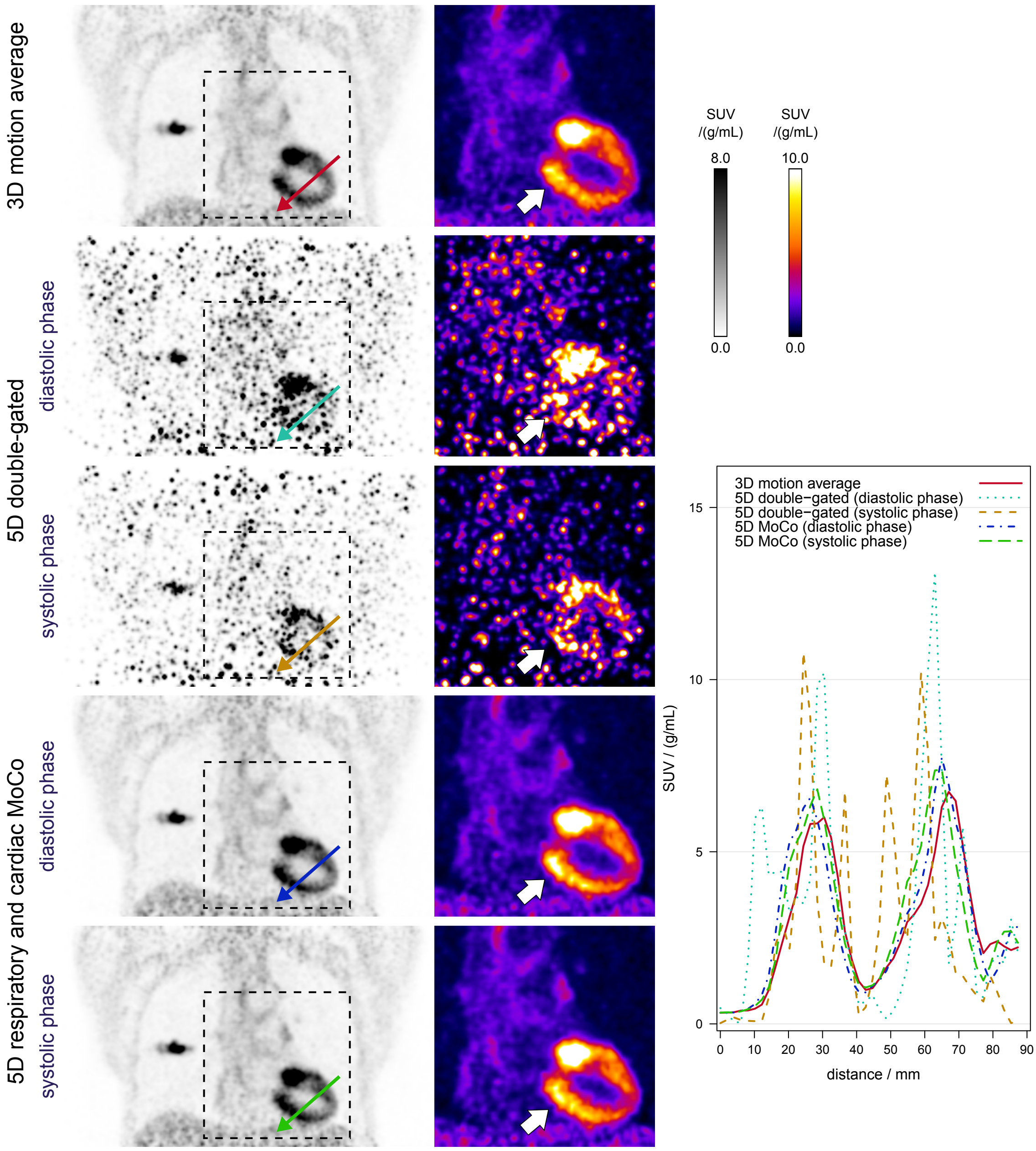

Figure 4.17: 5D PET study: PET reconstructions of different cardiac motion phases at end-exhale from data of a 56-year-old female patient (s02) in coronal orientation. The magnified views show the heart of the patient using a color scale to amplify differences between the images. The position of line profiles is indicated by arrows in the left column of the corresponding reconstructions. Adopted from Rank et al. (2016b).

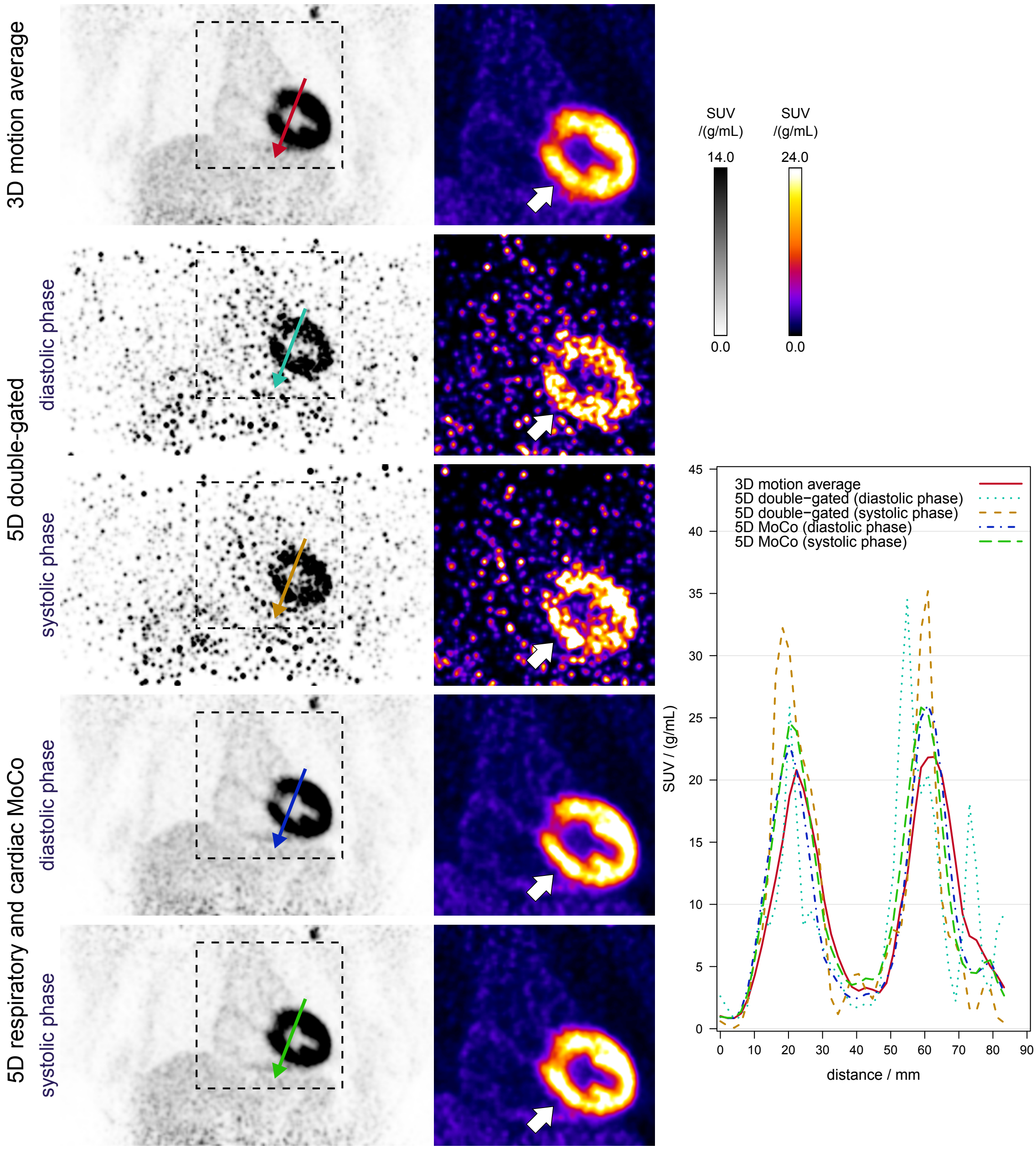

Figure 4.18: 5D PET study: PET reconstructions of different cardiac motion phases at end-exhale from data of a 48-year-old female patient (s04) in coronal orientation. The magnified views show the heart of the patient using a color scale to amplify differences between the images. The position of line profiles is indicated by arrows in the left column of the corresponding reconstructions. Adopted from Rank et al. (2016b).

4.4.2 Quantitative Evaluation of Image Reconstructions

The average variation of the parameters $\mathrm{SUV}_{\mathrm{mean}}$, $\mathrm{SUV}_{\mathrm{max}}$, volume, contrast and SNR for the myocardium of four patients is given in Table 4.4. Comparing 5D respiratory and cardiac MoCo images with the 3D motion average for the diastolic motion phase, all parameters were slightly increased. This result might indicate a slight improvement of quantification accuracy. As the left heart chamber is filled in the diastolic phase, an increased volume of the myocardium is expected. Likewise, the reduced volume of the systolic motion phase in 5D respiratory and cardiac MoCo images is in correspondence to expectations from cardiac physiology. While $\mathrm{SUV}_{\mathrm{mean}}$ and contrast yielded a slight increase for the systolic phase, $\mathrm{SUV}_{\mathrm{max}}$ and SNR were decreased. Standard deviations of systolic parameters were larger than the average variation of these parameters. As only four patients were evaluated, statistical significance of parameter variations was not proven by the data.

reconstruction algorithm	$\mathrm{SUV}_{\mathrm{mean}}$ / % of 3D	$\mathrm{SUV}_{\mathrm{max}}$ / % of 3D	volume / % of 3D	contrast / % of 3D	SNR / % of 3D
3D motion average	100.0	100.0	100.0	100.0	100.0
5D MoCo (diastolic phase)	102.8 ± 1.1	101.3 ± 3.3	105.0 ± 3.5	104.8 ± 2.0	102.7 ± 2.4
5D MoCo (systolic phase)	100.2 ± 3.7	97.1 ± 4.7	98.7 ± 5.3	101.2 ± 4.8	98.8 ± 5.1

Table 4.4: 5D PET study: Quantitative evaluation of PET images analyzing the myocardium. Mean and standard deviation describe the variation of parameters relative to the 3D motion average for a total number of four patients (listed in Table 3.2). The 5D MoCo algorithm corresponds to 5D respiratory and cardiac MoCo PET reconstructions.

5 | Discussion

In this chapter, sections 5.1 to 5.4 discuss findings of the four studies conducted in this work. This includes evaluation and comparison of results of the different methods for MR and PET image reconstruction developed in these studies. In addition, limitations and potential clinical applications of the algorithms are illustrated. An outlook providing ideas for improvement of MR and PET image reconstruction algorithms and data acquisition schemes is given in section 5.5.

5.1 4D Respiratory Time-Resolved MRI

MR imaging of the lung and upper abdomen is impaired by respiratory motion yielding motion blurring in case of 3D motion average reconstructions. As was shown in this study, performing respiratory time-resolved image reconstruction considerably reduces this blurring. However, standard motion handling strategies, e. g. breath-hold acquisition or gating, exhibit limitations in either temporal or spatial resolution, SNR, contrast and artifact level or demand inappropriately long acquisition times. For the highly undersampled data sets with undersampling factors of 16.8 evaluated in this study, 4D gated images revealed nondiagnostic image quality. To satisfy the Nyquist criterion for each respiratory phase, acquisition times of 10.2 to 11.5 min would have been required. As demonstrated for simulated and acquired MR data, the streak artifact and noise level of 4D images decreases considerably when using iterative image reconstruction methods. These methods seek to regularize the reconstructed images in such a way, that streak artifacts and noise are suppressed on the one hand while image sharpness and temporal fidelity are maintained on the other hand. To achieve an appropriate streak artifact level for the high undersampling factors employed in this study, the regularization of the 4D HDTV algorithm generated patch-like and grainy patterns in the images and decreased image sharpness. This behavior represents a trade-off for TV-based regularization (Block et al., 2007). While these effects were reduced in 4D MASTeR images (Asif et al., 2013), regularization of the image only in temporal dimension did not fully suppress streak artifacts in the images. The remaining streaks may generate spurious motion during the motion estimation step of the

MASTeR algorithm, which then decreases the accuracy of the motion-adaptive temporal regularization.

To address limitations of the other methods, the 4D joint MoCo-HDTV algorithm was proposed in this work. This algorithm combines advantages of motion compensation and iterative image reconstruction. Although it uses a similar regularization as 4D HDTV, the modified update equation described in Eq. (3.5) yields an improved sparsity of the image in the HDTV domain reducing the disadvantages of this type of regularization. As MVFs are estimated during the reconstruction process, the regularization within the final MoCo reconstruction can be disabled, which reveals an image perception similar to analytic gridding reconstructions.

To investigate the performance of the different reconstruction algorithms, the image similarity metrics MSE, SSIM, NCC and NMI were evaluated in comparison to the ground truth and in comparison to 4D gated reference reconstructions for simulated and acquired data, respectively. For all similarity metrics and subjects, 4D joint MoCo-HDTV outperformed 4D gated, 4D MASTeR (Asif et al., 2013) and 4D HDTV reconstructions. In addition, overall image quality in terms of image sharpness and artifact level was assessed by two radiologists for the acquired data in a blinded reading test. This assessment yielded significantly higher scores for 4D joint MoCo-HDTV than for 4D MASTeR and 4D HDTV reconstructions as well as higher scores than for 4D reference gated reconstructions with acquisition times being 6.6 to 11.1 times longer. The strong agreement of quantitative and qualitative assessment of reconstructed images provides confidence that the proposed 4D joint MoCo-HDTV algorithm achieved better image quality at high undersampling factors than the other approaches used for comparison. Furthermore, results demonstrate that 4D joint MoCo-HDTV enables reduction of acquisition times by about one order of magnitude when compared to standard 4D gated reconstructions. The algorithm showed a robust behavior for the thorax and upper abdomen region, for different subjects and image orientations, and for non-contrast-enhanced and contrast-enhanced acquisitions. Limitations of 4D joint MoCo-HDTV were found at describing sliding lung motion. This limitation affects only small regions at the interface of the lungs and the thorax. To improve results, either a segmentation of the lungs (Vandemeulebroucke et al., 2012) or a more sophisticated regularization of respiratory MVFs (Vishnevskiy et al., 2014) might be used.

Compared to the literature, 4D joint MoCo-HDTV shows similarities with previous work regarding the general approach of joint motion estimation and image reconstruction, in particular with the MASTeR (Asif et al., 2013) and deformation-corrected compressed sensing algorithm (Lingala et al., 2015). However, several major differences in initialization and regularization among these algorithms exist. Whereas the algorithms in Asif et al. (2013) and Lingala et al. (2015) required an initial guess for reconstruction, 4D joint MoCo-HDTV uses a multiresolution strategy with variable weighting of direct update and MoCo update in the update equation (Eq. (3.5)) instead to circumvent the problem that no MVFs are available at the initial reconstruction. In addition Asif et al. (2013) and Lingala et al. (2015) employed regularization in a deformation-compensated domain, while the proposed algorithm applies the HDTV regularization to the nondeformed image volume using a motion-adaptive weighting of temporal and spatial TV to reduce temporal blurring between adjacent motion phases with large differences in motion amplitude. Furthermore, this study demonstrates image reconstruction of 4D (3D + time) volumes located in the thorax and upper abdomen region. In contrast, Asif et al. (2013) and Lingala et al. (2015) did not consider out of plane motion and presented results of 2D + time reconstructions of cardiac MRI and myocardial perfusion MRI, respectively. With regard to data acquisition, the MASTeR algorithm (Asif et al., 2013) was applied to MR data acquired with a pseudo-random 2D Cartesian undersampling pattern while reconstruction of radial MR data was not presented in the original publication. This pseudo-random undersampling pattern might yield more incoherent undersampling artifacts, which might be better corrected for than streak artifacts arising from radial undersampling. For the implementation and radial undersampling factors used in this work, the MASTeR algorithm was found to be limited in suppressing streak artifacts while 4D joint MoCo-HDTV revealed better performance here.

As demonstrated in this study, the 4D joint MoCo-HDTV algorithm enables 4D respiratory time-resolved MRI with high undersampling factors and thus appropriately short acquisition times. Short acquisition times yield benefits, especially for pediatric examinations and for patients with discomfort in the scanner, and may reduce time and costs of MR examinations in general. Respiratory time-resolved 4D MRI with appropriate acquisition times might be of interest for a wide range of applications requiring dynamic information. Besides reducing motion blur in abdominal imaging, 4D MRI might be employed for the assessment of lung function in pulmonary imaging (von Siebenthal et al., 2007; Biederer et al., 2009, 2010). In the context of radiation oncology, potential applications are a patient-specific definition of safety margins or motion-adapted radiotherapy planning (Blackall et al., 2006; Dinkel et al., 2009; Hugo and Rosu, 2012; Sawant et al., 2014).

5.2 4D Respiratory Motion-Compensated PET

Similar to the 4D MRI study, respiratory motion represents a major challenge in PET image reconstruction of the thorax and abdomen. In PET, motion blurring yields an overestimation of lesion size or it leads to reduced SUVs, which may impede the detection of small lesions. 4D gated reconstructions as a standard motion handling strategy exhibit increased noise levels. The resulting local variations of SUVs might diminish the detectability of true lesions on the one hand while they might produce false positive findings on the other hand. In addition, the low number of counts in gated PET sinograms bias the reconstruction. In case of very low count numbers, the non-negativity constraint of the maximum likelihood expectation maximization PET reconstruction algorithm yields an overestimation of activity in regions with low uptake while regions with high uptake are underestimated (Walker et al., 2011; Van Slambrouck et al., 2014). MoCo PET reconstructions keep noise levels comparable to 3D motion average PET and are supposed to reduce motion blur in the images.

In this study, MR joint motion estimation and image reconstruction (4D jMoCo PET) using the 4D joint MoCo-HDTV algorithm was proposed for application to MoCo PET in simultaneous PET/MR imaging. Results were compared to a standard motion estimation method (4D sMoCo PET) employing 4D gated MR images for motion estimation. Comparing different MR acquisition times for motion estimation, the 4D sMoCo PET approach showed substantial degradation of quantification accuracy in case of MR acquisition times as low as 1 min and undersampling factors of 11.2. This degradation for short MR acquisition times can be explained by the strong undersampling producing severe streak artifacts in the MR images used for registration. As positions of radial streaks vary between motion phases, spurious motion is potentially introduced, which distorts the estimation of the actual respiratory patient motion. These findings are in correspondence to Grimm et al. (2015), who reported a decreased robustness of the standard motion estimation approach for undersampling factors of about 2.3 and larger. In contrast, the proposed 4D jMoCo PET approach was shown to be robust against strong radial undersampling of the MR acquisition. In a simulation study and *in vivo* for six patients, it showed significant improvements of PET image quality and quantification accuracy in terms of $\mathrm{SUV}_{\mathrm{mean}}$, $\mathrm{SUV}_{\mathrm{max}}$, FWHM/ lesion volume, contrast and SNR. The average increase of the parameters $\mathrm{SUV}_{\mathrm{mean}}$, $\mathrm{SUV}_{\mathrm{max}}$ and contrast was 32.7% and 12.7% compared to 3D motion average PET for simulated and patient data, respectively. These results are in accordance to Kinahan and Fletcher (2010), who reported an underestimation of SUV due to respiratory motion in the range of 25%.

Table 5.1 provides an overview of respiratory MoCo image reconstruction approaches for simultaneous PET/MR proposed in literature and applied to real patient data. Most of these approaches require several minutes of MR acquisition time per bed position for motion estimation. Moreover, they use a small number of motion phases, reduce spatial resolution or restrict the registration to only two dimensions, which improves robustness on the one hand, but might decrease accuracy of motion estimation on the other hand. The methods proposed in Würslin et al. (2013), Fayad et al. (2015b), Fürst et al. (2015) and Grimm et al. (2015) employ a standard motion estimation similar to the 4D sMoCo PET approach tested in this work. Compared to the methods from literature, the motion estimation method proposed in this study provides good temporal and spatial resolution (Table 5.1).

author	MR sequence	MR acquisition time / min	voxel size / mm^3	# of gates	motion estimation
Würslin et al. (2013)	2D multislice	3.0	$2.0 \times 2.0 \times 10.0$	4	3D
Petibon et al. (2014)	2D multislice	3.0	$2.0 \times 2.0 \times 8.0$	7	3D
Dutta et al. (2015)	2D radial	5.5 to 7.0	$2.0/2.3 \times 2.0/2.3 \times 5.0/8.0$	6	3D
Fayad et al. (2015a)	2D multislice	1.5	$2.0 \times 2.0 \times 10.0$	4	3D
Fayad et al. (2015b)	2D multislice	3.0	$2.0 \times 2.0 \times 10.0$	4	3D
Fürst et al. (2015)	radial stack-of-stars	10.0	$1.7 \times 1.7 \times 5.0$	5	3D
Grimm et al. (2015)	radial stack-of-stars	3.0 to 10.0	$1.7 \times 1.7 \times 5.0$	5	3D
Manber et al. (2015)	2D multislice	1.0 and 2.7	$1.8 \times 1.8 \times 10.0$[a]	10[b]	2D
proposed method	radial stack-of-stars	1.0	$1.6 \times 1.6 \times 4.5$	20[b,c]	3D

[a] 25 mm gap between slice centers
[b] Discrimination between inhalation and exhalation
[c] Motion phases have an overlap of 50%

Table 5.1: Overview of related work on respiratory MoCo image reconstruction for simultaneous PET/MR.

In this study, robust estimation of respiratory patient motion from highly undersampled MR data using acquisition times as short as 1 min per bed position was demonstrated. As typical PET acquisition times are in the range of 5 min per bed, this yields the opportunity to acquire a 1 min block of MR data for motion estimation at the beginning of the measurement and to spend the remaining 4 min of scan time for clinical MR examinations as shown in Fig. 3.13. This approach might have limitations when the breathing pattern and the maximum breathing amplitude of a patient vary considerably during the 5 min PET acquisition. For such cases, the 1 min MR acquisition for motion estimation might be subdivided into small data acquisition windows distributed uniformly over the full PET acquisition time. For slightly varying breathing amplitudes and periods as implemented in the simulation and for the six patients examined in this work, this problem did not occur.

To enable sorting of PET list-mode into gated sinograms, a motion surrogate signal has to be acquired for the full PET measurement. While the MR self-gating signal of the 5 min MR acquisition was used for gating in this work, an estimation of the motion surrogate signal from PET data would be required in practice (He et al., 2008; Büther et al., 2009; Schleyer et al., 2009; Fürst et al., 2015; Manber et al., 2015).

In the clinical environment, a reduction of motion blurring in PET images might increase the diagnostic value of simultaneous PET/MR when applied to regions affected by respiratory motion, such as the thorax and the abdomen. The resulting gain in contrast yields benefits for the detection of small tumor lesions or metastases. These small structures already exhibit reduced activity values as a result of the partial volume effect (Soret et al., 2007), which introduces image blurring due to the finite spatial resolution of the PET detector. Further reduction of activity caused by motion leads to additional bias in quantification accuracy and might prevent detection of the small structures. An improvement in quantification accuracy might advance PET-based staging of tumors (Wahl et al., 1994) and follow-up examinations to assess their response to therapy (Erdi et al., 2000).

5.3 5D Respiratory and Cardiac Motion-Compensated MRI

Besides the effect of respiratory motion, thoracic MR examinations are also affected by cardiac motion introducing blurring in the heart region. Accounting for two temporal dimensions and producing 5D double-gated reconstructions lead to further amplification of streak artifacts due to increased undersampling. For acquisition times as short as 2 min, image quality was nondiagnostic. For double-gated reconstructions satisfying the Nyquist sampling criterion for radial data, an acquisition time of about 69 min would have been required, which is not feasible in clinical routine. For MoCo image reconstruction, respiratory and cardiac motion estimation was performed sequentially due to the high undersampling of each combination of respiratory and cardiac motion phase. Respiratory MVFs were estimated in a similar fashion as for the 4D respiratory time-resolved studies. This allowed for 4D respiratory MoCo reconstruction, which already yielded a substantial improvement of image sharpness when compared to the motion average. This finding demonstrates that respiratory motion contributed most to motion blurring. While 5D respiratory MoCo and cardiac gated reconstructions additionally resolved different cardiac phases, images showed streak artifacts as only about 17% of the measured raw data were available for each cardiac phase. To enable robust estimation of cardiac MVFs from the highly undersampled MR data, the generation of respiratory MoCo MR raw data was required to have 100% of the measured information available for estimation of cardiac MVFs. To analyze the image sharpness of all methods that used 100% of the measured raw data for reconstruction, the image gradient was employed as image-based metric. In addition, images were assessed in a blinded reading test by two radiologists to simulate a clinically more relevant setting. Both evaluation methods were in strong agreement and demonstrated that 5D respiratory and cardiac MoCo images yielded increased image sharpness when compared with the motion average and when compared with MoCo reconstruction accounting for the respiratory dimension only. These results also show that the proposed method represents a robust and efficient method for estimation of respiratory and cardiac motion from strongly undersampled radial MR data. MR data can be acquired during free breathing without the need of any prospective control of image acquisition. In addition, respiratory and cardiac gating signals are derived intrinsically without the usage of navigators, ECG or external devices. Instead of estimating MVFs between all different motion phases, which would require $N_r \times N_c$ image registrations for reconstruction of a single combination of respiratory and cardiac phase (r, c), the proposed sequential motion estimation scheme needs only $N_r + N_c$ image registrations for reconstruction of any arbitrary combination. This circumstance results in a substantial reduction of computation times.

Considering clinical applications, results presented in this work certainly do not reveal the full potential of 5D MoCo reconstruction as MR data with parameters optimized for the clinical analysis of fibrosing lung disease were employed. As a 3D-encoded sequence was used, data of all partitions of a fixed spoke angle were correlated, which resulted in an effective temporal resolution of the data acquisition of about 170 ms. Especially for patients with increased heart rates, this temporal resolution might be insufficient leading to intraphase motion blurring. Moreover, spatial resolution of images was limited as the FOV was chosen to cover the complete thorax. In general, these settings do not satisfy the requirements of clinical applications in the field of cardiac MRI, which employ dedicated cardiac MR sequences and parameter settings. Thus instead of demonstrating cardiac-specific clinical applications, this work aimed at introducing a robust and efficient method for respiratory and cardiac motion estimation enabling time-resolved 5D MoCo image reconstruction from strongly undersampled MR data. To improve temporal resolution, state-of-the-art cardiac imaging methods either acquire a lower number of partitions or employ 3D radial sampling (Piccini et al., 2011; Feng et al., 2015; Monney et al., 2015; Piccini et al., 2016). The latter intrinsically provides isotropic spatial resolution. Furthermore, temporal resolution in the range of the repetition time can be achieved in theory as each acquired k-space line is independent.

Dynamic time-resolved MRI of the heart can provide valuable information for studying physiology (Francone et al., 2005; Muthurangu et al., 2008; Lurz et al., 2009; La Gerche et al., 2013). For such investigations, real-time cine MRI serves as clinical standard today. However, owing to the ultrafast data acquisition, only a single slice with reduced spatial resolution can be captured. In addition, images at different slice locations generally describe different motion cycles and a decoupled observation of respiratory and cardiac motion is not possible. Hence, 5D time-resolved MRI with appropriate acquisition times might overcome these limitations. If adapted to the cardiac-specific requirements, the proposed 5D MoCo reconstruction might develop high potential for clinical examinations. The intrinsic gating and acquisition during free breathing would simplify the clinical workflow and increase patient comfort. Furthermore, volumetric acquisition would require only a single measurement covering the complete heart region and allowing for reconstruction of any arbitrary combination of respiratory and cardiac motion phases.

5.4 5D Respiratory and Cardiac Motion-Compensated PET

In this study, the feasibility of 5D respiratory and cardiac MoCo PET image reconstruction was demonstrated. 5D double-gated PET images suffered from very high noise levels resulting in nondiagnostic image quality. In contrast, 5D MoCo PET images showed visual improvements with increased image sharpness and steeper line profiles when compared to 3D motion average PET reconstructions. The evaluation of quantitative parameters of the myocardium revealed smaller differences between MoCo images and the motion average than for lung lesions affected by respiratory motion. This can be explained by the smaller motion amplitude of the myocardium relative to its size when compared to lung lesions leading to less severe motion blurring. A further reason for the smaller differences is related to the cardiac MR self-gating. Unlike the data sets used in the 5D respiratory and cardiac MoCo MRI study, non-contrast-enhanced MR data were employed in this study. This circumstance reduced the accuracy of cardiac gating as image contrast within the heart was smaller than for contrast-enhanced data. As a result, measured MR and PET data were potentially assigned to wrong cardiac motion phases in some cases. This lead to a reduction of the cardiac motion amplitude and to an increase of intraphase motion blurring. The limited temporal resolution of the MR acquisition in the range of 160 ms might have further amplified these effects.

While visual improvements can be attributed to 5D MoCo PET images, the interpretation of quantitative parameters is more difficult for the myocardium. Any reconstruction-related changes of quantitative parameters interfere with physiologic changes of myocardial volume and tracer concentration when assessing different cardiac motion phases. Due to the technical limitations discussed previously, no distinct conclusions can be drawn. While the increase of the myocardial volume in the diastolic phase and the decrease in the systolic phase corresponds to the expectations from cardiac physiology, the small changes of the other parameters $\mathrm{SUV}_{\mathrm{mean}}$, $\mathrm{SUV}_{\mathrm{max}}$, contrast and SNR do not allow for proper interpretation of results, especially as no ground truth is available for comparison. For more accurate analysis, an improvement of cardiac MR gating for non-contrast-enhanced MR data and an adaptation of the MR data acquisition to cardiac-specific requirements are needed. Furthermore, preparation of patients with specific drug administration is required for cardiac examinations to increase the myocardial tracer uptake. To proceed beyond the stage of feasibility, further investigations on 5D respiratory and cardiac MoCo PET with a larger number of patients are necessary to demonstrate distinct improvements in quantification accuracy and clinical advantages of the proposed method.

5.5 Outlook

Future investigations should focus on improving the proposed methods on the one hand and on simplifying workflows regarding clinical applications on the other hand. In case of 4D respiratory time-resolved MRI, the potential of further reduction of acquisition times while keeping comparable image quality may be explored. For the implementation of 4D joint MoCo-HDTV used in this work, image noise and streak artifacts at borders of the FOV limited further reduction. Future studies on 4D respiratory MoCo PET may investigate the optimal number of respiratory motion phases for achieving the best quantification accuracy in MoCo PET reconstructions. For both 5D respiratory and cardiac MoCo studies, an adaptation to cardiac-specific requirements is desirable. This adaptation should include a careful choice of MR sequences as well as optimization of sequence parameters to improve MR image contrast of cardiac structures and to increase spatial and temporal resolution. In the following, a list of ideas is provided that might serve as a guidance to improve image quality and workflows of the different methods presented in this work.

Regularization of 4D joint MoCo-HDTV

To improve motion fidelity of image reconstructions for subjects with large motion amplitudes, regularization in a deformation-compensated domain may be investigated as proposed in Asif et al. (2013) and Lingala et al. (2015). In the current implementation of 4D joint MoCo-HDTV, the temporal TV applies temporal smoothing to the 4D image volume assuming small differences between adjacent motion phases. However, this assumption does not comply with patients having large motion amplitudes resulting in an underestimation of subject motion and in a blurring of structures strongly affected by motion. In addition, different spatial sparsity priors as an alternative to the spatial TV might be tested for regularization, for instance the wavelet transform. Instead of using a velocity map for controlling the regularization, cluster analysis may be applied to the MVFs to better distinguish between voxels affected by actual subject motion and voxels with spurious motion induced by streak artifacts. This knowledge might allow for region-dependent adaptation of the regularization improving the suppression of artifacts while preserving subject motion.

Motion Estimation of 4D joint MoCo-HDTV

To improve the accuracy of respiratory and cardiac motion estimation, additional knowledge may be incorporated into the registration process. In the current implementation, the binomial smoothing filter used for regularization of MVFs represents a trade-off between suppressing local errors caused by artifacts and inducing errors at regions with abrupt changes in motion amplitude, e. g. at the interface of the lungs and the thorax. To reduce errors caused by sliding lung motion, a segmentation of the thorax guiding an adaptive bilateral smoothing filter may be employed in case of respiratory motion. In addition, this segmentation might restrict the region of cardiac motion estimation. In the current implementation, registration between adjacent motion phases is performed independently and the cyclic regularization of MVFs is applied subsequently. Registration results might be improved by direct integration of the cyclic regularization into the registration process instead. Furthermore, knowledge about streak artifacts might be added to the image registration (Brehm et al., 2013; Rank et al., 2014) or a 3D–2D registration might be employed (Flach et al., 2014; Rank et al., 2015). For the latter, the image volume of the source motion phase would be deformed in such a way that it matches the measured raw data of the destination motion phase.

Upsampling of Motion Vector Fields

For a given number of motion phases, i. e. a fixed temporal resolution, reduction of MR acquisition time generally decreases robustness of MVF estimation. A lower number of motion bins, however, increases intraphase motion blurring. To circumvent this blurring, each motion phase may be subdivided into several subphases and intermediate MVFs may be calculated to deform these subphases. During MoCo image reconstruction, each subphase would then be deformed by an adapted MVF. In general, MVFs describe the deformation between the centers of source and destination motion phase. To adapt a MVF to a specific subphase, displacement might be scaled by considering mean motion amplitudes of subphases relative to the full-width motion phase used for motion estimation. This technique might allow for further reduction of acquisition time while preserving image sharpness and robustness of motion estimation. Instead, the hierarchical approach for image reconstruction may be extended to the temporal dimension. Starting at a low temporal resolution with a small number of motion phases, several reconstruction steps with an increasing number of motion bins may be performed.

k-Space Sampling

In this work, undersampling of the MR acquisition was only applied to the radial plane of the stack-of-stars sampling. To either increase spatial resolution of the reconstructed images or further reduce MR acquisition time, the Cartesian partition direction may be undersampled as well. Figure 5.1 shows the k-space coverage in partition direction of the current sampling method in comparison to a variable-density sampling as proposed by Feng et al. (2016b). Both sampling schemes use an equal number of data points and thus require the same acquisition time. However, employing variable-density sampling allows for sampling of higher frequencies in the partition direction and therefore increases spatial resolution of the reconstructed images. Instead, a comparable spatial resolution may be achieved requiring only half of the acquisition time. In addition, Cartesian undersampling would render radial streak artifacts in a less coherent fashion yielding benefits for iterative image reconstruction of sparse data. To further gain incoherence, spoke angles might be slightly disturbed for each partition. A disadvantage of additional undersampling in the partition direction is the increase of noise in the reconstructed images, which has to be balanced with the undersampling factor. Hence, SNR-efficient MR sequences, such as balanced steady-state free precession sequences might be used in the future (Oppelt et al., 1986). As these sequences are sensitive to rapidly changing eddy currents, the golden angle radial spacing might be replaced by a small surrogate (Wundrak et al., 2015). As an alternative to radial stack-of-stars sampling, 3D radial sampling may be considered as it provides isotropic spatial resolution and high temporal resolution (Piccini et al., 2011; Feng et al., 2015; Monney et al., 2015; Piccini et al., 2016).

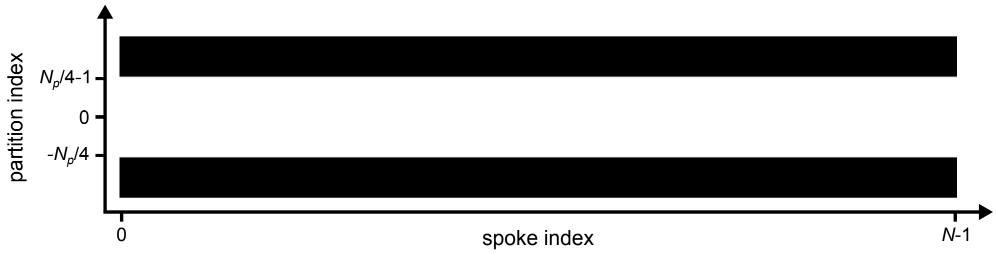

(a) standard k-space sampling

(b) variable density sampling

Figure 5.1: Comparison of standard k-space sampling in partition direction and variable density sampling (Feng et al., 2016b). White pixels indicate sampled k-space data while black areas are not measured.

Self-Gating

The derivation of cardiac self-gating signals may be improved as this procedure failed for some data sets, especially when non-contrast-enhanced MR data was employed. Investigations may focus on more optimal filters to increase robustness of the extraction of the cardiac motion signal from MR raw data. Instead, external ECG data might be acquired during the measurement. In case of simultaneous PET/MR acquisitions, intrinsic PET gating as described in He et al. (2008), Büther et al. (2009), Schleyer et al. (2009), Fürst et al. (2015) and Manber et al. (2015) may be developed rather than using MR data for gating. With regard to clinical application of PET/MR MoCo reconstruction, this development would be necessary if only a part of the MR acquisition time was used for motion estimation.

Incorporation of Contrast Dynamics into MR Reconstruction

Future developments may extend the existing MoCo MR reconstruction algorithms to a further temporal dimension describing contrast dynamics of abdominal or cardiac perfusion measurements. This would allow for reconstruction of 6D (3D + respiratory + cardiac + contrast dynamics) image volumes as proposed for micro-CT imaging of small animals (Sawall et al., 2012). To achieve appropriate acquisition times and reduce artifacts and noise in the images, additional regularization along the perfusion dimension, e. g. using TV or bilateral filtering, would be required.

PET Reconstruction

To increase image sharpness of PET images and thus improve detectability of small structures, the OSEM reconstruction algorithm may be extended to a maximum a posteriori formulation (Green, 1990; Qi et al., 1998; Dutta et al., 2015). Using this formulation, additional knowledge about the reconstructed PET volume can be incorporated into the cost function. For instance, the spatial smoothing operation can be included instead of applying a smoothing filter with a fixed strength at the end of each iteration. Besides, spatial TV regularization might be considered for PET reconstructions.

Practical Considerations

Although MR and PET/MR MoCo image reconstruction was tested with patient data in this work, several practical problems have to be solved with regard to clinical implementation of these methods. In this context, one important aspect is a considerable reduction of computation times for motion estimation and image reconstruction. Computational effort described in sections 3.1.5 and 3.2.4 was based on nonoptimized code and thus more efficient implementation of algorithms is required, e. g. employing graphics processing units for calculations. As the 4D joint MoCo-HDTV algorithm formed the basis of all studies conducted in this work, simplification of this algorithm and optimization of data processing may help to further reduce computation times. To increase the performance of forward and backward transforms during the iterative MR reconstruction process, a reduction of the number of coil channels is desired. Besides applying more advanced coil compression techniques as proposed in Zhang et al. (2013), the lower limit of compressed coil channels that still enables robust motion estimation may be investigated. Thus only a small number of channels may be employed for motion estimation while using a larger number of coils for the final image reconstruction. In addition, one repetition of each resolution level during 4D joint MoCo-HDTV reconstruction might be sufficient for robust motion estimation and image reconstruction.

A further step towards clinical application is a simplification of workflows. In this work, both MR and PET data were processed and reconstructed offline at workstations not directly connected to the scanners. Several manual steps for copying and processing data were necessary until images could be reconstructed. For clinical routine, fully automated workflows are desired, i. e. either a direct processing and reconstruction of data at the scanner console or at servers connected to the scanner would be required. For the latter, the Gadgetron framework providing features such as an extraction of MR raw data from the scanner, processing and image reconstruction, and injection of reconstructed images back to the scanner, might be suitable (Hansen and Sørensen, 2013). As offline MR image reconstruction was performed in this work, vendor-provided data correction methods were not available. Especially for applications in radiation oncology, a correction of geometric distortions of MR images caused by nonlinear gradient fields is important. Furthermore, an improved normalization of intensity inhomogeneities in MR images due to varying spatial sensitivities of coil channels is desirable.

While several practical issues remain, this work demonstrated that employing respiratory and cardiac MoCo MR and PET image reconstruction lead to considerable improvement of image quality when compared to standard methods used in clinical routine today. Furthermore, substantial reduction of MR acquisition times at comparable image quality was achieved, which can help to improve patient comfort in the scanner and to increase patient throughput in clinical practice.

6 | Conclusions

The aim of this work was to develop novel algorithms for time-resolved 4D (3D + respiratory) and 5D (3D + respiratory + cardiac) MoCo MR and PET image reconstruction with a focus on short MR acquisition times. Shortening MR acquisition times improves patient comfort in the scanner and increases patient throughput in clinical practice.

In the *4D respiratory time-resolved MRI* study, the 4D joint MoCo-HDTV algorithm was proposed, which alternates between MoCo MR image reconstruction and artifact-robust motion estimation at multiple resolution levels. It was shown that 4D joint MoCo-HDTV reveals 4D respiratory time-resolved MR images with low streak artifact levels and high image sharpness when using free-breathing radial MR data with acquisition times of 40 s and undersampling factors of 16.8. The achieved image quality was comparable to standard 4D gated reconstructions with acquisition times being about one order of magnitude longer. The novel method may be employed for a wide range of clinical applications, which require time-resolved 4D imaging acquired within appropriate acquisition times below 1 min.

In the *4D respiratory MoCo PET* study, a framework for simultaneous PET/MR image reconstruction was implemented incorporating motion information derived from MR into the MoCo PET reconstruction. It was demonstrated that employing artifact-robust motion estimation allows for MoCo PET reconstruction based on MR acquisition times as short as 1 min per bed position yielding results comparable to 5 min MR acquisitions. The remaining MR acquisition time can be used for clinical examinations. The proposed method may be integrated into clinical PET/MR improving PET image quality and quantification accuracy compared to 3D motion average PET and 4D gated PET and thus increasing the diagnostic value of simultaneous PET/MR.

For the *5D respiratory and cardiac MoCo MRI* study, a robust method for sequential estimation of respiratory and cardiac motion was developed. Using this method, time-resolved 5D MoCo image reconstruction of the complete thorax region from strongly undersampled MR data with undersampling factors of 36 and acquisition times below 2 min becomes possible. Any arbitrary combination of respiratory and cardiac motion phase can be reconstructed using 100% of the measured MR data. Reconstructed images revealed increased image sharpness in the heart region when compared to the motion average and to methods compensating for respiratory motion only. The proposed approach may be directly adapted to cardiac-specific applications, for which time-resolved 5D MR imaging offers new opportunities to study the interaction of respiration and cardiac motion.

In the *5D respiratory and cardiac MoCo PET* study, employing the respiratory and cardiac MVFs estimated from MR for 5D MoCo PET reconstruction demonstrated basic feasibility of the approach. While 5D MoCo PET images exhibited visual improvements compared to the motion average, no distinct conclusions on quantification accuracy could be drawn.

The methods developed in this work were adapted to cyclic motion in the thorax region, in particular to respiratory and cardiac motion. Other types of motion and body regions, e. g. irregular head motion, were not considered and would require different compensation methods. Results achieved for thoracic and abdominal imaging when using MoCo MR and PET image reconstruction represent distinct improvements of image quality in terms of image sharpness, artifact level and quantification accuracy when compared to standard methods used in clinical routine today. In comparison to these standard techniques, substantial reduction of MR acquisition times at comparable image quality can be realized improving patient comfort and increasing patient throughput in clinical practice. However, these opportunities go along with increased complexity of reconstruction methods demanding considerably longer computation times.

Besides improvements of motion estimation and image reconstruction, future work may focus on a reduction of required computation times and a simplification of workflows. These developments are inevitable for clinically feasible implementation of algorithms and they can only be achieved by close cooperation with the vendor. This would allow for broad application of MoCo image reconstruction in clinical routine and may help to improve the diagnostic value of thoracic and abdominal MR and simultaneous PET/MR examinations in the future.

Bibliography

Arnold, J. F. T., Mörchel, P., Glaser, E., Pracht, E. D., and Jakob, P. M. (2007). Lung MRI using an MR-compatible active breathing control (MR-ABC). *Magnetic Resonance in Medicine*, 58(6):1092–1098.

Asif, M. S., Hamilton, L., Brummer, M., and Romberg, J. (2013). Motion-adaptive spatio-temporal regularization for accelerated dynamic MRI. *Magnetic Resonance in Medicine*, 70(3):800–812.

Bailey, D. L., Antoch, G., Bartenstein, P., Barthel, H., Beer, A. J., Bisdas, S., Bluemke, D. A., Boellaard, R., Claussen, C. D., Franzius, C., Hacker, M., Hricak, H., la Fougère, C., Gückel, B., Nekolla, S. G., Pichler, B. J., Purz, S., Quick, H. H., Sabri, O., Sattler, B., Schäfer, J., Schmidt, H., van den Hoff, J., Voss, S., Weber, W., Wehrl, H. F., and Beyer, T. (2015a). Combined PET/MR: The real work has just started: Summary report of the "3rd International Workshop on PET/MR Imaging". *Molecular Imaging and Biology*, 17(3):297–312.

Bailey, D. L., Pichler, B. J., Gückel, B., Barthel, H., Beer, A. J., Bremerich, J., Czernin, J., Drzezga, A., Franzius, C., Goh, V., Hartenbach, M., Iida, H., Kjaer, A., la Fougère, C., Ladefoged, C. N., Law, I., Nikolaou, K., Quick, H. H., Sabri, O., Schäfer, J., Schäfers, M., Wehrl, H. F., and Beyer, T. (2015b). Combined PET/MRI: Multi-modality multi-parametric imaging is here: Summary report of the "4th International Workshop on PET/MR Imaging". *Molecular Imaging and Biology*, 17(5):595–608.

Bailey, D. L., Townsend, D. W., Valk, P. E., and Maisey, M. N. (2005). *Positron emission tomography: Basic sciences.* Springer.

Batchelor, P. G., Atkinson, D., Irarrazaval, P., Hill, D. L. G., Hajnal, J., and Larkman, D. (2005). Matrix description of general motion correction applied to multishot images. *Magnetic Resonance in Medicine*, 54(5):1273–1280.

Beatty, P. J., Nishimura, D. G., and Pauly, J. M. (2005). Rapid gridding reconstruction with a minimal oversampling ratio. *IEEE Transactions on Medical Imaging*, 24(6):799–808.

Bernstein, M. A., King, K. F., and Zhou, X. J. (2004). *Handbook of MRI pulse sequences.* Elsevier Academic Press.

Bezrukov, I., Mantlik, F., Schmidt, H., Schölkopf, B., and Pichler, B. J. (2013). MR-based PET attenuation correction for PET/MR imaging. *Seminars in Nuclear Medicine*, 43(1):45–59.

Biederer, J., Hintze, C., Fabel, M., and Dinkel, J. (2009). Investigation of respiratory-dependent movements of pulmonary space-occupying lesions with MRI. *Der Radiologe*, 49(8):705–711.

Biederer, J., Hintze, C., Fabel, M., and Dinkel, J. (2010). Magnetic resonance imaging and computed tomography of respiratory mechanics. *Journal of Magnetic Resonance Imaging*, 32(6):1388–1397.

Blackall, J. M., Ahmad, S., Miquel, M. E., McClelland, J. R., Landau, D. B., and Hawkes, D. J. (2006). MRI-based measurements of respiratory motion variability and assessment of imaging strategies for radiotherapy planning. *Physics in Medicine and Biology*, 51(17):4147–4169.

Bloch, F. (1946). Nuclear induction. *Physical Review*, 70(7-8):460–474.

Block, K. T. (2008). *Advanced methods for radial data sampling in magnetic resonance imaging*. PhD thesis, Georg-August-Universität Göttingen.

Block, K. T., Chandarana, H., Milla, S., Bruno, M., Mulholland, T., Fatterpekar, G., Hagiwara, M., Grimm, R., Geppert, C., Kiefer, B., and Sodickson, D. K. (2014). Towards routine clinical use of radial stack-of-stars 3D gradient-echo sequences for reducing motion sensitivity. *Journal of the Korean Society of Magnetic Resonance in Medicine*, 18(2):87–106.

Block, K. T., Uecker, M., and Frahm, J. (2007). Undersampled radial MRI with multiple coils. Iterative image reconstruction using a total variation constraint. *Magnetic Resonance in Medicine*, 57(6):1086–1098.

Boyd, S. and Vandenberghe, L. (2004). *Convex optimization*. Cambridge University Press.

Brasse, D., Kinahan, P. E., Lartizien, C., Comtat, C., Casey, M., and Michel, C. (2005). Correction methods for random coincidences in fully 3D whole-body PET: Impact on data and image quality. *Journal of Nuclear Medicine*, 46(5):859–867.

Brehm, M., Paysan, P., Oelhafen, M., and Kachelrieß, M. (2013). Artifact-resistant motion estimation with a patient-specific artifact model for motion-compensated cone-beam CT. *Medical Physics*, 40(10):101913–1–13.

Brehm, M., Paysan, P., Oelhafen, M., Kunz, P., and Kachelrieß, M. (2012). Self-adapting cyclic registration for motion-compensated cone-beam CT in image-guided radiation therapy. *Medical Physics*, 39(12):7603–7618.

Brehm, M., Sawall, S., Maier, J., Sauppe, S., and Kachelrieß, M. (2015). Cardiorespiratory motion-compensated micro-CT image reconstruction using an artifact model-based motion estimation. *Medical Physics*, 42(4):1948–1958.

Buerger, C. and Clough, R. E. (2012). Nonrigid motion modeling of the liver from 3-D undersampled self-gated golden-radial phase encoded MRI. *IEEE Transactions on Medical Imaging*, 31(3):805–815.

Burgos, N., Cardoso, M. J., Thielemans, K., Modat, M., Pedemonte, S., Dickson, J., Barnes, A., Ahmed, R., Mahoney, C. J., Schott, J. M., Duncan, J. S., Atkinson, D., Arridge, S. R., Hutton, B. F., and Ourselin, S. (2014). Attenuation correction synthesis for hybrid PET-MR scanners: Application to brain studies. *IEEE Transactions on Medical Imaging*, 33(12):2332–2341.

Büther, F., Dawood, M., Stegger, L., Wübbeling, F., Schäfers, M., Schober, O., and Schäfers, K. P. (2009). List mode-driven cardiac and respiratory gating in PET. *Journal of Nuclear Medicine*, 50(5):674–681.

Bydder, M., Larkman, D. J., and Hajnal, J. V. (2002). Combination of signals from array coils using image-based estimation of coil sensitivity profiles. *Magnetic Resonance in Medicine*, 47(3):539–548.

Candès, E. J., Romberg, J., and Tao, T. (2006). Robust uncertainty principles: Exact signal reconstruction from highly incomplete frequency information. *IEEE Transactions on Information Theory*, 52(2):489–509.

Catana, C. (2015). Motion correction options in PET/MRI. *Seminars in Nuclear Medicine*, 45(3):212–223.

Catana, C., Wu, Y., Judenhofer, M. S., Qi, J., Pichler, B. J., and Cherry, S. R. (2006). Simultaneous acquisition of multislice PET and MR images: Initial results with a MR-compatible PET scanner. *Journal of Nuclear Medicine*, 47(12):1968–1976.

Claessen, G., Claus, P., Delcroix, M., Bogaert, J., La Gerche, A., and Heidbuchel, H. (2014). Interaction between respiration and right versus left ventricular volumes at rest and during exercise: A real-time cardiac magnetic resonance study. *American Journal of Physiology. Heart and Circulatory Physiology*, 306(6):H816–H824.

Collignon, A., Maes, F., Delaere, D., Vandermeulen, D., Suetens, P., and Marchal, G. (1995). Automated multi-modality image registration based on information theory. *Information Processing in Medical Imaging*, 3(6):263–274.

Cruz, G., Atkinson, D., Buerger, C., Schaeffter, T., and Prieto, C. (2016). Accelerated motion corrected three-dimensional abdominal MRI using total variation regularized SENSE reconstruction. *Magnetic Resonance in Medicine*, 75(4):1484–1498.

de Bazelaire, C. M. J., Duhamel, G. D., Rofsky, N. M., and Alsop, D. C. (2004). MR imaging relaxation times of abdominal and pelvic tissues measured in vivo at 3.0 T: Preliminary results. *Radiology*, 230(3):652–659.

DeBenedetti, S., Cowan, C. E., Konneker, W. R., and Primakoff, H. (1950). On the angular distribution of two-photon annihilation radiation. *Physical Review*, 77(2):205–212.

Delso, G., Fürst, S., Jakoby, B., Ladebeck, R., Ganter, C., Nekolla, S. G., Schwaiger, M., and Ziegler, S. I. (2011). Performance measurements of the Siemens mMR integrated whole-body PET/MR scanner. *Journal of Nuclear Medicine*, 52(12):1914–1922.

Dempster, A. A., Laird, N. N., and Rubin, D. D. B. (1977). Maximum likelihood from incomplete data via the EM algorithm. *Journal of the Royal Statistical Society, Series B (Methodological)*, 39(1):1–38.

Deshmane, A., Gulani, V., Griswold, M. A., and Seiberlich, N. (2012). Parallel MR imaging. *Journal of Magnetic Resonance Imaging*, 36(1):55–72.

Dinkel, J., Hintze, C., Tetzlaff, R., Huber, P. E., Herfarth, K., Debus, J., Kauczor, H. U., and Thieke, C. (2009). 4D-MRI analysis of lung tumor motion in patients with hemidiaphragmatic paralysis. *Radiotherapy and Oncology*, 91(3):449–454.

Donoho, D. L. (2006). Compressed sensing. *IEEE Transactions on Information Theory*, 52(4):1289–1306.

Dutta, J., Huang, C., Li, Q., and El Fakhri, G. (2015). Pulmonary imaging using respiratory motion compensated simultaneous PET/MR. *Medical Physics*, 42(7):4227–4240.

Earls, J. P., Ho, V. B., Foo, T. K., Castillo, E., and Flamm, S. D. (2002). Cardiac MRI: Recent progress and continued challenges. *Journal of Magnetic Resonance Imaging*, 16(2):111–127.

Erdi, Y. E., Macapinlac, H., Rosenzweig, K. E., Humm, J. L., Larson, S. M., Erdi, A. K., and Yorke, E. D. (2000). Use of PET to monitor the response of lung cancer to radiation treatment. *European Journal of Nuclear Medicine and Molecular Imaging*, 27(7):861–866.

Fayad, H., Odille, F., Schmidt, H., Würslin, C., Küstner, T., Feblinger, J., and Visvikis, D. (2015a). The use of a generalized reconstruction by inversion of coupled systems (GRICS) approach for generic respiratory motion correction in PET/MR imaging. *Physics in Medicine and Biology*, 60(6):2529–2546.

Fayad, H., Schmidt, H., Würslin, C., and Visvikis, D. (2015b). Reconstruction incorporated respiratory motion correction in clinical simultaneous PET/MR imaging for oncology applications. *Journal of Nuclear Medicine*, 56(6):884–889.

Feng, L., Axel, L., Chandarana, H., Block, K. T., Sodickson, D. K., and Otazo, R. (2016a). XD-GRASP: Golden-angle radial MRI with reconstruction of extra motion-state dimensions using compressed sensing. *Magnetic Resonance in Medicine*, 75(2):775–788.

Feng, L., Coppo, S., Piccini, D., Lim, R. P., Stuber, M., Sodickson, D. K., and Otazo, R. (2015). Five-dimensional cardiac and respiratory motion-resolved whole-heart MRI. *Proceedings of the International Society for Magnetic Resonance Imaging*, 23:0027.

Feng, L., Grimm, R., Block, K. T., Chandarana, H., Kim, S., Xu, J., Axel, L., Sodickson, D. K., and Otazo, R. (2014). Golden-angle radial sparse parallel MRI: Combination of compressed sensing, parallel imaging, and golden-angle radial sampling for fast and flexible dynamic volumetric MRI. *Magnetic Resonance in Medicine*, 72(3):707–717.

Feng, L., Srichai, M. B., Lim, R. P., Harrison, A., King, W., Adluru, G., Dibella, E. V. R., Sodickson, D. K., Otazo, R., and Kim, D. (2013). Highly accelerated real-time cardiac cine MRI using k-t SPARSE-SENSE. *Magnetic Resonance in Medicine*, 70(1):64–74.

Feng, L., Zhao, T., Chandarana, H., Sodickson, D. K., and Otazo, R. (2016b). Motion-resolved golden-angle radial sparse MRI using variable-density stack-of-stars sampling. *Proceedings of the International Society for Magnetic Resonance Imaging*, 24:1091.

Fischer, S. E., Wickline, S. A., and Lorenz, C. H. (1999). Novel real-time R-wave detection algorithm based on the vectorcardiogram for accurate gated magnetic resonance acquisitions. *Magnetic Resonance in Medicine*, 42(2):361–370.

Flach, B., Brehm, M., Sawall, S., and Kachelrieß, M. (2014). Deformable 3D-2D registration for CT and its application to low dose tomographic fluoroscopy. *Physics in Medicine and Biology*, 59(24):7865–7887.

Francone, M., Dymarkowski, S., Kalantzi, M., and Bogaert, J. (2005). Real-time cine MRI of ventricular motion: A novel approach to assess ventricular coupling. *Journal of Magnetic Resonance Imaging*, 21(3):305–309.

Fürst, S., Grimm, R., Hong, I., Souvatzoglou, M., Casey, M. E., Schwaiger, M., Nekolla, S. G., and Ziegler, S. I. (2015). Motion correction strategies for integrated PET/MR. *Journal of Nuclear Medicine*, 56(2):261–269.

Glover, G. H. and Pauly, J. M. (1992). Projection reconstruction techniques for reduction of motion effects in MRI. *Magnetic Resonance in Medicine*, 28(2):275–289.

Gottesfeld Brown, L. (1992). A survey of image registration techniques. *ACM Computing Surveys*, 24(4):325–376.

Green, P. J. (1990). Bayesian reconstructions from emission tomography data using a modified EM algorithm. *IEEE Transactions on Medical Imaging*, 9(1):84–93.

Grimm, R., Block, K. T., Kiefer, B., and Hornegger, J. (2011). Bias correction for respiration detection in radial 3D gradient-echo imaging. *Proceedings of the International Society for Magnetic Resonance Imaging*, 19:2677.

Grimm, R., Forman, C., Hutter, J., Kiefer, B., Hornegger, J., and Block, K. T. (2013).

Fast automatic coil selection for radial stack-of-stars GRE imaging. *Proceedings of the International Society for Magnetic Resonance Imaging*, 21:3786.

Grimm, R., Fürst, S., Souvatzoglou, M., Forman, C., Hutter, J., Dregely, I., Ziegler, S. I., Kiefer, B., Hornegger, J., Block, K. T., and Nekolla, S. G. (2015). Self-gated MRI motion modeling for respiratory motion compensation in integrated PET/MRI. *Medical Image Analysis*, 19(1):110–120.

Haacke, E. M., Brown, R. W., Thompson, M. R., and Venkatesan, R. (1999). *Magnetic resonance imaging: Physical principles and sequence design.* John Wiley & Sons, Inc.

Hansen, M. S. and Sørensen, T. S. (2013). Gadgetron: An open source framework for medical image reconstruction. *Magnetic Resonance in Medicine*, 69(6):1768–1776.

He, J., O'Keefe, G. J., Gong, S. J., Jones, G., Saunder, T., Scott, A. M., and Geso, M. (2008). A novel method for respiratory motion gated with geometric sensitivity of the scanner in 3D PET. *IEEE Transactions on Nuclear Science*, 55(5):2557–2565.

Hestenes, M. R. and Stiefel, E. (1952). Method of conjugate gradients for solving linear systems. *Journal of Research of the National Bureau of Standards*, 49(6):409–436.

Heußer, T., Rank, C. M., Freitag, M. T., Dimitrakopoulou-Strauss, A., Schlemmer, H.-P., Beyer, T., and Kachelrieß, M. (2016). Simultaneous reconstruction of attenuation and activity for non-TOF PET/MR. *IEEE Transactions on Nuclear Science*, (early view online).

Hill, D. L., Batchelor, P. G., Holden, M., and Hawkes, D. J. (2001). Medical image registration. *Physics in Medicine and Biology*, 46(3):R1–R45.

Hollingsworth, K. G. (2015). Reducing acquisition time in clinical MRI by data undersampling and compressed sensing reconstruction. *Physics in Medicine and Biology*, 60(21):R297–R322.

Hudson, H. M. and Larkin, R. S. (1994). Accelerated image reconstruction using ordered subsets of projection data. *IEEE Transactions on Medical Imaging*, 13(4):601–609.

Hugo, G. D. and Rosu, M. (2012). Advances in 4D radiation therapy for managing respiration: Part I - 4D imaging. *Zeitschrift für Medizinische Physik*, 22(4):258–271.

Ionascu, D., Jiang, S. B., Nishioka, S., Shirato, H., and Berbeco, R. I. (2007). Internal-external correlation investigations of respiratory induced motion of lung tumors. *Medical Physics*, 34(10):3893–3903.

Jackson, J. I., Meyer, C. H., Nishimura, D. G., and Macovski, A. (1991). Selection of a convolution function for Fourier inversion using gridding. *IEEE Transactions on Medical Imaging*, 10(3):473–478.

Jadvar, H. and Colletti, P. M. (2014). Competitive advantage of PET/MRI. *European Journal of Radiology*, 83(1):84–94.

Kaiser, J. F. (1974). Nonrecursive digital filter design using the I0-SINH window function. *Proceedings of the IEEE International Symposium on Circuits and Systems*, pages 20–23.

Kak, A. C. and Slaney, M. (1988). *Principles of computerized tomographic imaging.* Society for Industrial and Applied Mathematics.

Keereman, V., Mollet, P., Berker, Y., Schulz, V., and Vandenberghe, S. (2013). Challenges and current methods for attenuation correction in PET/MR. *Magnetic Resonance Materials in Physics, Biology and Medicine*, 26(1):81–98.

Kim, E. E., Lee, M.-C., Inoue, T., and Wong, W.-H. (2013). *Clinical PET and PET/CT.* Springer.

Kinahan, P. E. and Fletcher, J. W. (2010). PET/CT standardized uptake values (SUVs) in clinical practice and assessing response to therapy. *Seminars in Ultrasound, CT and MRI*, 31(6):496–505.

Kinahan, P. E. and Karp, J. S. (1994). Figures of merit for comparing reconstruction algorithms with a volume-imaging PET scanner. *Physics in Medicine and Biology*, 39(3):631–642.

Kingston, A., Sakellariou, A., Varslot, T., Myers, G., and Sheppard, A. (2011). Reliable automatic alignment of tomographic projection data by passive auto-focus. *Medical Physics*, 38(9):4934–4945.

La Gerche, A., Claessen, G., Van De Bruaene, A., Pattyn, N., Van Cleemput, J., Gewillig, M., Bogaert, J., Dymarkowski, S., Claus, P., and Heidbuchel, H. (2013). Cardiac MRI: A new gold standard for ventricular volume quantification during high-intensity exercise. *Circulation: Cardiovascular Imaging*, 6(2):329–338.

Lange, K. and Carson, R. (1984). EM reconstruction algorithms for emission and transmission tomography. *Journal of Computer Assisted Tomography*, 8(2):306–316.

Larkman, D. J. and Nunes, R. G. (2007). Parallel magnetic resonance imaging. *Physics in Medicine and Biology*, 52(7):R15–R55.

Larson, A. C., Kellman, P., Arai, A., Hirsch, G. A., McVeigh, E., Li, D., and Simonetti, O. P. (2005). Preliminary investigation of respiratory self-gating for free-breathing segmented cine MRI. *Magnetic Resonance in Medicine*, 53(1):159–168.

Larson, A. C., Simonetti, O. P., and Li, D. (2002). Coronary MRA with 3D undersampled projection reconstruction trueFISP. *Magnetic Resonance in Medicine*, 48(4):594–601.

Larson, A. C., White, R. D., Laub, G., McVeigh, E. R., Li, D., and Simonetti, O. P. (2004). Self-gated cardiac cine MRI. *Magnetic Resonance in Medicine*, 51(1):93–102.

Li, T., Thorndyke, B., Schreibmann, E., Yang, Y., and Xing, L. (2006). Model-based image reconstruction for four-dimensional PET. *Medical Physics*, 33(5):1288–1298.

Liang, Z.-P. and Lauterbur, P. C. (1999). *Principles of magnetic resonance imaging: A signal processing perspective*. Wiley-IEEE Press Series in Biomedical Engineering, 1st edition.

Lin, W., Guo, J., Rosen, M. A., and Song, H. K. (2008). Respiratory motion-compensated radial dynamic contrast-enhanced (DCE)-MRI of chest and abdominal lesions. *Magnetic Resonance in Medicine*, 60(5):1135–1146.

Lingala, S. G., DiBella, E., and Jacob, M. (2015). Deformation corrected compressed sensing (DC-CS): A novel framework for accelerated dynamic MRI. *IEEE Transactions on Medical Imaging*, 34(1):72–85.

Lurz, P., Muthurangu, V., Schievano, S., Nordmeyer, J., Bonhoeffer, P., Taylor, A. M., and Hansen, M. S. (2009). Feasibility and reproducibility of biventricular volumetric assessment of cardiac function during exercise using real-time radial k-t SENSE magnetic resonance imaging. *Journal of Magnetic Resonance Imaging*, 29(5):1062–1070.

Lustig, M., Donoho, D., and Pauly, J. M. (2007). Sparse MRI: The application of compressed sensing for rapid MR imaging. *Magnetic Resonance in Medicine*, 58(6):1182–1195.

Lustig, M., Donoho, D. L., Santos, J. M., and Pauly, J. M. (2008). Compressed sensing MRI. *IEEE Signal Processing Magazine*, 25(2):72–82.

Manber, R., Thielemans, K., Hutton, B., Barnes, A., Ourselin, S., Arridge, S., O'Meara, C., Wan, S., and Atkinson, D. (2015). Practical PET respiratory motion correction in clinical PET/MR. *Journal of Nuclear Medicine*, 56(6):890–897.

Martinez-Möller, A., Souvatzoglou, M., Delso, G., Bundschuh, R. A., Chefd'hotel, C., Ziegler, S. I., Navab, N., Schwaiger, M., and Nekolla, S. G. (2009). Tissue classification as a potential approach for attenuation correction in whole-body PET/MRI: Evaluation with PET/CT data. *Journal of Nuclear Medicine*, 50(4):520–526.

McClelland, J. R., Hawkes, D. J., Schaeffter, T., and King, A. P. (2013). Respiratory motion models: A review. *Medical Image Analysis*, 17(1):19–42.

McGee, K. P., Manduca, A., Felmlee, J. P., Riederer, S. J., and Ehman, R. L. (2000). Image metric-based correction (autocorrection) of motion effects: Analysis of image metrics. *Journal of Magnetic Resonance Imaging*, 11(2):174–181.

McGibney, G., Smith, M. R., Nichols, S. T., and Crawley, A. (1993). Quantitative evaluation of several partial Fourier reconstruction algorithms used in MRI. *Magnetic Resonance in Medicine*, 30(1):51–59.

McHugh, M. L. (2012). Interrater reliability: The kappa statistic. *Biochemia Medica*, 22(3):276–282.

Mehranian, A., Arabi, H., and Zaidi, H. (2016). Vision 20/20: Magnetic resonance imaging-guided attenuation correction in PET/MRI: Challenges, solutions, and opportunities. *Medical Physics*, 43(3):1130–1155.

Monney, P., Piccini, D., Rutz, T., Vincenti, G., Coppo, S., Koestner, S. C., Sekarski, N., Di Bernardo, S., Bouchardy, J., Stuber, M., and Schwitter, J. (2015). Single centre experience of the application of self navigated 3D whole heart cardiovascular magnetic resonance for the assessment of cardiac anatomy in congenital heart disease. *Journal of Cardiovascular Magnetic Resonance*, 17(55):1–12.

Montesinos, P., Abascal, J. F. P. J., Cussó, L., Vaquero, J. J., and Desco, M. (2014). Application of the compressed sensing technique to self-gated cardiac cine sequences in small animals. *Magnetic Resonance in Medicine*, 72(2):369–380.

Munoz, C., Kolbitsch, C., Reader, A. J., Marsden, P., Schaeffter, T., and Prieto, C. (2016). MR-based cardiac and respiratory motion-compensation techniques for PET-MR imaging. *PET Clinics*, 11(2):179–191.

Muthurangu, V., Lurz, P., Critchely, J. D., Deanfield, J. E., Taylor, A. M., and Hansen, M. S. (2008). Real-time assessment of right and left ventricular volumes and function in patients with congenital heart disease by using high spatiotemporal resolution radial k-t SENSE. *Radiology*, 248(3):782–791.

Nensa, F., Beiderwellen, K., Heusch, P., and Wetter, A. (2014). Clinical applications of PET/MRI: Current status and future perspectives. *Diagnostic and Interventional Radiology*, 20(5):438–447.

Nyquist, H. (1928). Thermal agitation of electric charge in conductors. *Physical Review*, 32(1):110–113.

Odille, F., Vuissoz, P. A., Marie, P. Y., and Felblinger, J. (2008). Generalized reconstruction by inversion of coupled systems (GRICS) applied to parallel MRI. *Magnetic Resonance in Medicine*, 60(1):146–157.

Oliveira, F. P. M. and Tavares, J. M. R. S. (2014). Medical image registration: A review. *Computer Methods in Biomechanics and Biomedical Engineering*, 17(2):73–93.

Oppelt, A., Graumann, R., Barfuss, H., Fischer, H., Hartl, W., and Schajor, W. (1986). FISP - a new fast MRI sequence. *Electromedica*, 54(1):15–18.

O'Sullivan, J. D. (1985). A fast sinc function gridding algorithm for Fourier inversion in computer tomography. *IEEE Transactions on Medical Imaging*, 4(4):200–207.

Paling, M. R. and Brookeman, J. R. (1986). Respiration artifacts in MR imaging: Reduction by breath holding. *Journal of Computer Assisted Tomography*, 10(6):1080–1082.

Paulus, D. H., Quick, H. H., Geppert, C., Fenchel, M., Zhan, Y., Hermosillo, G., Faul, D., Boada, F., Friedman, K. P., and Koesters, T. (2015). Whole-body PET/MR imaging: Quantitative evaluation of a novel model-based MR attenuation correction method including bone. *Journal of Nuclear Medicine*, 56(7):1061–1066.

Petibon, Y., Huang, C., Ouyang, J., Reese, T. G., Li, Q., Syrkina, A., Fakhri, G. E., and Chen, Y.-l. (2014). Relative role of motion and PSF compensation in whole-body oncologic PET-MR imaging. *Medical Physics*, 41(4):042503–1–12.

Piccini, D., Feng, L., Bonanno, G., Coppo, S., Yerly, J., Lim, R. P., Schwitter, J., Sodickson, D. K., Otazo, R., and Stuber, M. (2016). Four-dimensional respiratory motion-resolved whole heart coronary MR angiography. *Magnetic Resonance in Medicine*, (early view online).

Piccini, D., Littmann, A., Nielles-Vallespin, S., and Zenge, M. O. (2011). Spiral phyllotaxis: The natural way to construct a 3D radial trajectory in MRI. *Magnetic Resonance in Medicine*, 66(4):1049–1056.

Pichler, B. J., Judenhofer, M. S., Catana, C., Walton, J. H., Kneilling, M., Nutt, R. E., Siegel, S. B., Claussen, C. D., and Cherry, S. R. (2006). Performance test of an LSO-APD detector in a 7-T MRI scanner for simultaneous PET/MRI. *Journal of Nuclear Medicine*, 47(4):639–647.

Purcell, E. M., Torrey, H. C., and Pound, R. V. (1946). Resonance absorption by nuclear magnetic moments in a solid. *Physical Review*, 69(1-2):37–38.

Qi, J., Leahy, R. M., Hsu, C., Farquhar, T. H., and Cherry, S. R. (1998). Fully 3D Bayesian image reconstruction for the ECAT EXACT HR+. *IEEE Transactions on Nuclear Science*, 45(3):1096–1103.

Qiao, F., Pan, T., Clark, J. W., and Mawlawi, O. R. (2006). A motion-incorporated reconstruction method for gated PET studies. *Physics in Medicine and Biology*, 51(15):3769–3783.

Quick, H. H. (2014). Integrated PET/MR. *Journal of Magnetic Resonance Imaging*, 39(2):243–258.

Quirk, S., Becker, N., and Smith, W. L. (2013). External respiratory motion analysis and statistics for patients and volunteers. *Journal of Applied Clinical Medical Physics*, 14(2):90–101.

Ramachandran, G. N. and Lakshminarayanan, A. V. (1971). Three-dimensional reconstruction from radiographs and electron micrographs: Application of convolutions instead of Fourier transforms. *Proceedings of the National Academy of Sciences of the United States of America*, 68(9):2236–2240.

Rank, C. M., Heußer, T., Brehm, M., and Kachelrieß, M. (2014). Artifact model-based respiratory motion compensation (MoCo) for simultaneous PET/MR based on strongly undersampled radial MR data. *Proceedings of the IEEE Nuclear Science Symposium and Medical Imaging Conference*, 978(1):3–6.

Rank, C. M., Heußer, T., Buzan, M. T. A., Wetscherek, A., Freitag, M. T., Dinkel, J., and Kachelrieß, M. (2016a). 4D respiratory motion-compensated image reconstruction of free-breathing radial MR data with very high undersampling. *Magnetic Resonance in Medicine*, (early view online).

Rank, C. M., Heußer, T., Flach, B., Brehm, M., and Kachelrieß, M. (2015). Respiratory motion compensation for simultaneous PET/MR based on a 3D-2D registration of strongly undersampled radial MR data: A simulation study. *Proceedings of SPIE, Medical Imaging: Physics of Medical Imaging*, 9412:941218–1–8.

Rank, C. M., Heußer, T., Wetscherek, A., Freitag, M. T., Schlemmer, H.-P., and Kachelrieß, M. (2016b). Five-dimensional respiratory and cardiac motion compensation for simultaneous PET/MR. *Proceedings of the IEEE Nuclear Science Symposium and Medical Imaging Conference*, (accepted, in press).

Rank, C. M., Heußer, T., Wetscherek, A., Freitag, M. T., Schlemmer, H.-P., and Kachelrieß, M. (2016c). Respiratory motion compensation for simultaneous PET/MR using strongly undersampled MR data. *Proceedings of the International Society for Magnetic Resonance Imaging*, 24:4249.

Rank, C. M., Heußer, T., Wetscherek, A., Freitag, M. T., Sedlaczek, O., Schlemmer, H.-P., and Kachelrieß, M. (2016d). Respiratory motion compensation for simultaneous PET/MR based on highly undersampled MR data. *Medical Physics*, (accepted, in press).

Rasche, V., De Boer, R. W., Holz, D., and Proksa, R. (1995). Continuous radial data acquisition for dynamic MRI. *Magnetic Resonance in Medicine*, 34(5):754–761.

Reiser, M. F., Semmler, W., and Hricak, H. (2008). *Magnetic resonance tomography*. Springer, 1st edition.

Ritschl, L., Bergner, F., Fleischmann, C., and Kachelrieß, M. (2011). Improved total variation-based CT image reconstruction applied to clinical data. *Physics in Medicine and Biology*, 56(6):1545–1561.

Ritschl, L., Sawall, S., Knaup, M., Hess, A., and Kachelrieß, M. (2012). Iterative 4D cardiac micro-CT image reconstruction using an adaptive spatio-temporal sparsity prior. *Physics in Medicine and Biology*, 57(6):1517–1525.

Rockmore, A. J. and Macovski, A. (1976). A maximum likelihood approach to emission image reconstruction from projections. *IEEE Transactions in Nuclear Science*, 23(4):1428–1432.

Rokey, R., Wendt, R. E., and Johnston, D. L. (1988). Monitoring of acutely ill patients during nuclear magnetic resonance imaging: Use of a time-varying filter electrocardiographic gating device to reduce gradient artifacts. *Magnetic Resonance in Medicine*, 6(2):240–245.

Roncali, E. and Cherry, S. R. (2011). Application of silicon photomultipliers to positron emission tomography. *Annals of Biomedical Engineering*, 39(4):1358–1377.

Rudin, L. I., Osher, S., and Fatemi, E. (1992). Nonlinear total variation based noise removal algorithms. *Physica D: Nonlinear Phenomena*, 60(1-4):259–268.

Saha, G. B. (2010). *Basics of PET imaging: Physics, chemistry, and regulations.* Springer.

Sauppe, S. J., Hahn, A., Brehm, M., Paysan, P., Seghers, D., and Kachelrieß, M. (2016). Five-dimensional motion compensation for respiratory and cardiac motion with cone-beam CT of the thorax region. *Proceedings of SPIE, Medical Imaging: Physics of Medical Imaging*, 9783:97830H–1–9.

Sawall, S., Kuntz, J., Socher, M., Knaup, M., Hess, A., Bartling, S., and Kachelrieß, M. (2012). Imaging of cardiac perfusion of free-breathing small animals using dynamic phase-correlated micro-CT. *Medical Physics*, 39(12):7499–7506.

Sawant, A., Keall, P., Pauly, K. B., Alley, M., Vasanawala, S., Loo, B. W., Hinkle, J., and Joshi, S. (2014). Investigating the feasibility of rapid MRI for image-guided motion management in lung cancer radiotherapy. *BioMed Research International*, 485067:1–7.

Schleyer, P. J., O'Doherty, M. J., Barrington, S. F., and Marsden, P. K. (2009). Retrospective data-driven respiratory gating for PET/CT. *Physics in Medicine and Biology*, 54(7):1935–1950.

Schultz, C. L., Alfidi, R. J., Nelson, A. D., Kopiwoda, S. Y., and Clampitt, M. E. (1984). The effect of motion on two-dimensional Fourier transformation magnetic resonance images. *Radiology*, 152(1):117–121.

Shannon, C. E. (1948). A mathematical theory of communication. *The Bell System Technical Journal*, 27:379–423/623–656.

Shepp, L. A. and Vardi, Y. (1982). Maximum likelihood reconstruction for emission tomography. *IEEE Transactions on Medical Imaging*, 1(2):113–122.

Song, J., Liu, Q. H., Johnson, G. A., and Badea, C. T. (2007). Sparseness prior based iterative image reconstruction for retrospectively gated cardiac micro-CT. *Medical Physics*, 34(11):4476–4483.

Soret, M., Bacharach, S. L., and Buvat, I. (2007). Partial-volume effect in PET tumor imaging. *Journal of Nuclear Medicine*, 48(6):932–945.

Stanisz, G. J., Odrobina, E. E., Pun, J., Escaravage, M., Graham, S. J., Bronskill, M. J., and Henkelman, R. M. (2005). T1, T2 relaxation and magnetization transfer in tissue at 3T. *Magnetic Resonance in Medicine*, 54(3):507–512.

Tan, W., Xu, L., Wang, X., Qiu, D., Han, G., and Hu, D. (2013). Estimation of the displacement of cardiac substructures and the motion of the coronary arteries using electrocardiographic gating. *OncoTargets and Therapy*, 2013(6):1325–1332.

Thirion, J. P. (1998). Image matching as a diffusion process: An analogy with Maxwell's demons. *Medical Image Analysis*, 2(3):243–260.

Tsoumpas, C., Buerger, C., King, A. P., Mollet, P., Keereman, V., Vandenberghe, S., Schulz, V., Schleyer, P., Schaeffter, T., and Marsden, P. K. (2011). Fast generation of 4D PET-MR data from real dynamic MR acquisitions. *Physics in Medicine and Biology*, 56(20):6597–6613.

Uecker, M., Zhang, S., Voit, D., Karaus, A., Merboldt, K.-D., and Frahm, J. (2010). Real-time MRI at a resolution of 20 ms. *NMR in Biomedicine*, 23(8):986–994.

Uecker, M., Zhang, S., Voit, D., Merboldt, K.-D., and Frahm, J. (2012). Real-time MRI: Recent advances using radial FLASH. *Imaging in Medicine*, 4(4):461–476.

Van Slambrouck, K., Stute, S., Comtat, C., Sibomana, M., van Velden, F., Boellaard, R., and Nuyts, J. (2014). Bias reduction for low-statistics PET: Maximum likelihood reconstruction with a modified Poisson distribution. *IEEE Transactions on Medical Imaging*, 34(1):1–11.

Vandemeulebroucke, J., Bernard, O., Rit, S., Kybic, J., Clarysse, P., and Sarrut, D. (2012). Automated segmentation of a motion mask to preserve sliding motion in deformable registration of thoracic CT. *Medical Physics*, 39(2):1006–1015.

Vercauteren, T., Pennec, X., Perchant, A., and Ayache, N. (2009). Diffeomorphic demons: Efficient non-parametric image registration. *NeuroImage*, 45(1):S61–S72.

Vigen, K. K., Peters, D. C., Grist, T. M., Block, W. F., and Mistretta, C. A. (2000). Undersampled projection-reconstruction imaging for time-resolved contrast-enhanced imaging. *Magnetic Resonance in Medicine*, 43(2):170–176.

Viola, P. and Wells, W. M., I. (1995). Alignment by maximization of mutual information. *Proceedings of the IEEE International Conference on Computer Vision*, 24(2):16–23.

Vishnevskiy, V., Gass, T., Székely, G., and Gokse, O. (2014). Total variation regularization of displacements in parametric image registration. In *Abdominal Imaging. Computational and Clinical Applications*, volume 8676, pages 211–220. Springer.

Visvikis, D., Lamare, F., Bruyant, P., Boussion, N., and Cheze Le Rest, C. (2006). Respiratory motion in positron emission tomography for oncology applications: Problems and solutions. *Proceedings of the 3rd International Conference on Imaging Technologies in Biomedical Sciences*, 569(2):453–357.

von Siebenthal, M., Székely, G., Gamper, U., Boesiger, P., Lomax, A., and Cattin, P. (2007). 4D MR imaging of respiratory organ motion and its variability. *Physics in Medicine and Biology*, 52(6):1547–1564.

Wahl, R. L., Quint, L. E., Greenough, R. L., Meyer, C. R., White, R. I., and Orringer, M. B. (1994). Staging of mediastinal non-small cell lung cancer with FDG PET, CT, and fusion images: Preliminary prospective evaluation. *Radiology*, 191(2):371–377.

Walker, M. D., Asselin, M.-C., Julyan, P. J., Feldmann, M., Talbot, P. S., Jones, T., and Matthews, J. C. (2011). Bias in iterative reconstruction of low-statistics PET data: Benefits of a resolution model. *Physics in Medicine and Biology*, 56(4):931–949.

Wang, H. and Amini, A. A. (2012). Cardiac motion and deformation recovery from MRI: A review. *IEEE Transactions on Medical Imaging*, 31(2):487–503.

Wang, Z., Bovik, A. C., Sheikh, H. R., and Simoncelli, E. P. (2004). Image quality assessment: From error visibility to structural similarity. *IEEE Transactions on Image Processing*, 13(4):600–612.

Watson, C. C. (2000). New, faster, image-based scatter correction for 3D PET. *IEEE Transactions on Nuclear Science*, 47(4):1587–1594.

Wells, W. M., Viola, P., Atsumi, H., Nakajima, S., and Kikinis, R. (1996). Multi-modal volume registration by maximization of mutual information. *Medical Image Analysis*, 1(1):35–51.

Wilcoxon, F. (1945). Individual comparisons by ranking methods. *Biometrics Bulletin*, 1(6):80–83.

Winkelmann, S., Schaeffter, T., Koehler, T., Eggers, H., and Doessel, O. (2007). An optimal radial profile order based on the golden ratio for time-resolved MRI. *IEEE Transactions on Medical Imaging*, 26(1):68–76.

World Medical Association (2013). World Medical Association Declaration of Helsinki: Ethical principles for medical research involving human subjects. *JAMA*, 310(20):2191–2194.

Wundrak, S., Paul, J., Ulrici, J., Hell, E., and Rasche, V. (2015). A small surrogate for the golden angle in time-resolved radial MRI based on generalized fibonacci sequences. *IEEE Transactions on Medical Imaging*, 34(6):1262–1269.

Würslin, C., Schmidt, H., Martirosian, P., Brendle, C., Boss, A., Schwenzer, N. F., and

Stegger, L. (2013). Respiratory motion correction in oncologic PET using T1-weighted MR imaging on a simultaneous whole-body PET/MR system. *Journal of Nuclear Medicine*, 54(3):464–471.

Wyawahare, M. V., Patil, P. M., and Abhyankar, H. K. (2009). Image registration techniques: An overview. *International Journal of Signal Processing, Image Processing and Pattern Recognition*, 2(3):11–28.

Zhang, S., Block, K. T., and Frahm, J. (2010a). Magnetic resonance imaging in real time: Advances using radial FLASH. *Journal of Magnetic Resonance Imaging*, 31(1):101–109.

Zhang, S., Joseph, A. a., Voit, D., Schaetz, S., Merboldt, K.-D., Unterberg-Buchwald, C., Hennemuth, A., Lotz, J., and Frahm, J. (2014). Real-time magnetic resonance imaging of cardiac function and flow - recent progress. *Quantitative Imaging in Medicine and Surgery*, 4(5):313–329.

Zhang, S., Uecker, M., Voit, D., Merboldt, K.-D., and Frahm, J. (2010b). Real-time cardiovascular magnetic resonance at high temporal resolution: Radial FLASH with nonlinear inverse reconstruction. *Journal of Cardiovascular Magnetic Resonance*, 12(39):1–7.

Zhang, T., Pauly, J. M., Vasanawala, S. S., and Lustig, M. (2013). Coil compression for accelerated imaging with Cartesian sampling. *Magnetic Resonance in Medicine*, 69(2):571–582.

Zitová, B. and Flusser, J. (2003). Image registration methods: A survey. *Image and Vision Computing*, 21(11):977–1000.

List of Figures

List of Tables

Publications

Parts of this thesis have been published in the following journal articles and conference contributions:

Journal Articles (Peer-Reviewed)

Rank, C. M., Heußer, T., Wetscherek, A., Freitag, M. T., Sedlaczek, O., Schlemmer, H.-P., and Kachelrieß, M. (2016). Respiratory motion compensation for simultaneous PET/MR based on highly undersampled MR data. *Medical Physics*, (accepted, in press).

Rank, C. M., Heußer, T., Buzan, M. T. A., Wetscherek, A., Freitag, M. T., Dinkel, J., and Kachelrieß, M. (2016). 4D respiratory motion-compensated image reconstruction of free-breathing radial MR data with very high undersampling. *Magnetic Resonance in Medicine*, (early view online).

Heußer, T., Rank, C. M., Freitag, M. T., Dimitrakopoulou-Strauss, A., Schlemmer, H.-P., Beyer, T., and Kachelrieß, M. (2016). MR-consistent simultaneous reconstruction of attenuation and activity for non-TOF PET/MR. *IEEE Transactions on Nuclear Science*, (early view online).

Kolb, C., Wetscherek, A., Buzan, M. T., Werner, R., Rank, C. M., Kachelrieß, M., Kreuter, M., Dinkel, J., Heußel, C. P., and Maier-Hein, K. (2016). Regional lung ventilation analysis using temporally resolved MRI. *Journal of Computer Assisted Tomography*, (early view online).

Conference Proceedings

Rank, C. M., Heußer, T., Wetscherek, A., Freitag, M. T., Schlemmer, H.-P., and Kachelrieß, M. (2016). Five-dimensional respiratory and cardiac motion compensation for simultaneous PET/MR. *Proceedings of the IEEE Nuclear Science Symposium and Medical Imaging Conference*, (accepted, in press).

Heußer, T., Rank, C. M., Freitag, M. T., and Kachelrieß, M. (2016). MLAA-based headphone attenuation estimation in hybrid PET/MR imaging. *Proceedings of the IEEE Nuclear Science Symposium and Medical Imaging Conference*, (accepted, in press).

Rank, C. M., Sauppe, S., Heußer, T., Wetscherek, A., and Kachelrieß, M. (2016). Five-dimensional respiratory and cardiac motion compensation based on strongly undersampled MR data. *Proceedings of the International Society for Magnetic Resonance in Medicine*, 24:0786.

Rank, C. M., Heußer, T., Wetscherek, A., Freitag, M. T., Schlemmer, H.-P., and Kachelrieß, M. (2016). Respiratory motion compensation for simultaneous PET/MR using strongly undersampled MR data. *Proceedings of the International Society for Magnetic Resonance in Medicine*, 24:4249.

Heußer, T., Rank, C. M., Freitag, M. T., Schlemmer, H.-P., Dimitrakopoulou-Strauss, A., Beyer, T., and Kachelrieß, M. (2016). Joint estimation of attenuation and activity distributions for clinical non-TOF FDG head patient PET/MR data employing MR prior information. *Proceedings of the International Society for Magnetic Resonance in Medicine*, 24:1775.

Rank, C. M., Heußer, T., Wetscherek, A., Pfaffenberger, A., and Kachelrieß, M. (2016). Respiratory time-resolved 4D MR imaging for RT applications with acquisition times below one minute. *Radiotherapy & Oncology*, 119(S1):S33.

Sauppe, S., Rank, C. M., Hahn, A., Brehm, M., Paysan, P., Seghers, D., and Kachelrieß, M. (2016). Cardio-respiratory motion compensation for 5D thoracic CBCT in IGRT. *Radiotherapy & Oncology*, 119(S1):S452–S453.

Rank, C. M., Heußer, T., Brehm, M., and Kachelrieß, M. (2015). Motion compensation (MoCo) for simultaneous PET/MR based on strongly undersampled radial MR data – A simulation study. *Proceedings of the International Society for Magnetic Resonance in Medicine*, 23:2579.

Heußer, T., Rank, C. M., Beyer, T., and Kachelrieß, M. (2015). MR-consistent simultaneous reconstruction of attenuation and activity for non-TOF PET/MR: A simulation study. *Proceedings of the Fully Three-Dimensional Image Reconstruction in Radiology and Nuclear Medicine.*

Rank, C. M., Heußer, T., Wetscherek, A., and Kachelrieß, M. (2015). Respiratory motion compensation for simultaneous PET/MR based on strongly undersampled radial MR data. *Proceedings of the 4th Conference on PET/MR and SPECT/MR, EJNMMI Physics*, 2(Suppl 1):A24.

Heußer, T., Rank, C. M., Beyer, T., and Kachelrieß, M. (2015). Simultaneous reconstruction of attenuation and activity for non-TOF PET/MR using MR prior information. *Proceedings of the 4th Conference on PET/MR and SPECT/MR, EJNMMI Physics*, 2(Suppl 1):A30.

Rank, C. M., Heußer, T., Flach, B., Brehm, M., and Kachelrieß, M. (2015). Respiratory motion compensation for simultaneous PET/MR based on a 3D–2D registration of strongly undersampled radial MR data: A simulation study. *Proceedings of SPIE, Medical Imaging: Physics of Medical Imaging*, 9412:941218–1–8.

Rank, C. M., Heußer, T., Brehm, M., and Kachelrieß, M. (2014). Artifact model–based respiratory motion compensation (MoCo) for simultaneous PET/MR based on strongly undersampled radial MR data. *Proceedings of the IEEE Nuclear Science Symposium and Medical Imaging Conference*, 978(1):3–6.

Scientific Awards

Runner-up Oral Presentation, *5th Conference on PET/MR and SPECT/MR* 2016, May 13–25, 2016 – Cologne, Germany.

3rd Place for Best Electronic Poster Presentation (within Detection & Correction of Motion in MRI & MRS Study Group), *ISMRM 24th Annual Meeting and Exhibition* 2016, May 7–13, 2016 – Singapore.

ECR 2016 – Best Scientific Paper Presentation (within the topic Physics in Radiology), *European Congress of Radiology* 2016, March 2–6, 2016 – Vienna, Austria.

Acknowledgments

An dieser Stelle möchte ich mich bei allen, die zum Gelingen meiner Doktorarbeit beigetragen haben, ganz herzlich bedanken, insbesondere bei:

Prof. Dr. Peter Bachert für die Übernahme des Erstgutachtens.

Prof. Dr. Marc Kachelrieß für die Übernahme des Zweitgutachtens, die freundliche Aufnahme in seine Arbeitsgruppe und die Möglichkeit, dieses interessante Thema bearbeiten zu dürfen. Herzlichen Dank für die umfassende Betreuung meiner Arbeit, die großartige Förderung sowie die stets freundliche und überaus kompetente Hilfe bei allen auftretenden Fragen und Problemen.

Allen Mitarbeitern der Arbeitsgruppe „Röntgenbildgebung und Computertomographie" für die kollegiale Hilfsbereitschaft und stets angenehme und freundschaftliche Arbeitsatmosphäre. Insbesondere vielen Dank an das „MoCo"-Büro mit Juliane, Thorsten, Sebastian und Sergej für die großartige Zusammenarbeit sowie den guten Kaffee und die unterhaltsamen und lustigen Gespräche zwischendurch.

Dr. Andreas Wetscherek für die tolle Zusammenarbeit bei der Entwicklung der MR-Rekonstruktion und die vielen hilfreichen Diskussionen.

Dr. Martin Freitag für die große fachliche Unterstützung bei medizinischen Fragestellungen aller Art.

Prof. Dr. Julien Dinkel, Dr. Teo Buzan und Dr. Oliver Sedlaczek für die großzügige Bereitstellung von Patientendaten sowie Regula Gnirs für die Unterstützung bei PET/MR-Messungen.

Prof. Dr. Thomas Beyer, Dr. Thomas Koesters und Dr. Matthias Fenchel für ihre Hilfe bei der Entwicklung der Rekonstruktion von PET-Daten.

Allen Korrekturlesern für ihre Hilfe und mühevolle Arbeit.

Ein ganz besonderer Dank gilt meinen Eltern für die Ermöglichung meines Physikstudiums und die herzliche Unterstützung in jeglicher Hinsicht.